

ABSTRACT

VO, ALLISON MARIE. Multi-Proxy Approach to Reconstructing a Paleoseismic Record of Cascadia Subduction Zone Earthquakes in Late Holocene Sediments of Lake Crescent, WA. (Under the direction of Dr. Elana L. Leithold).

This study investigates the late Holocene sediment record of Lake Crescent, WA to provide a template for interpreting the origin of the event deposits formed earlier in its history. Lake Crescent is a deep, oligotrophic, glacially-carved lake located between the Strait of Juan de Fuca and the northern margin of the Olympic Mountains. Lake Crescent's proximity to the Cascadia subduction zone, steep subaqueous slopes, and steady sediment accumulation rate render it a prime setting to preserve earthquake-induced event deposits in its sediment archive. Previous research on the Lake Crescent sediment record has identified numerous seismically-triggered mass wasting deposits, but the origins of some event layers remain uncertain.

Three types of event layers have been identified in sediments deposited during the past ca. 500 years, all of which are interpreted as turbidites. The most prominent turbidite was observed across the lake's southern basin, where it ranges from 2 to 15 cm in thickness. Strong evidence suggests that this deposit formed during the 1700 A.D. Cascadia subduction earthquake, when multiple subaqueous slopes failed around the lake basin. By comparison, ten turbidites of similar thickness that were previously identified in sediments that accumulated over the last ~3100 years are also interpreted as the products of strong shaking during earthquakes. The spatial extent of several thin turbidites deposited since 1700 AD is greater than would be expected from fluvial inputs, suggesting they formed during less-intense earthquake-induced shaking that triggered smaller, localized slope failures. The timing of accumulation of these layers is

consistent with historical earthquakes that occurred on Vancouver Island, Canada, and near Olympia and Entiat, Washington.

© Copyright 2019 by Allison Vo

All Rights Reserved

Multi-Proxy Approach to Reconstructing a Paleoseismic Record of Cascadia Subduction
Zone Earthquakes in Late Holocene Sediments of Lake Crescent, WA.

by
Allison Marie Vo

A thesis submitted to the Graduate Faculty of
North Carolina State University
in partial fulfillment of the
requirements for the degree of
Master of Science

Marine, Earth & Atmospheric Sciences

Raleigh, North Carolina
2019

APPROVED BY:

Dr. Elana L. Leithold
Committee Chair

Dr. Karl W. Wegmann

Dr. Ethan Hyland

DEDICATION

To my parents for their constant love and never-ending support of my dreams and ambitions, no matter how short-lived or left-field they may seem. To my best friend, for being the most supportive live-in therapist and chef; this experience wouldn't have been the same without you. To my grandma for inspiring my love of the outdoors and instilling a strong curiosity in me. To all the friends, family, professors, and mentors who encouraged me to and helped me find my way. Also to Beenie, the soil-eating, rock hound every geologist needs.

BIOGRAPHY

I come from a military family but I have always called North Carolina home. I became interested in the sciences early on and found myself at the North Carolina School of Science and Mathematics. I escaped to the beach for a few years while attending Florida Atlantic University, where I discovered my love for field geology and environmental conservation. After spending some time traveling, I came back home to pursue my Master's degree at North Carolina State University.

ACKNOWLEDGMENTS

I would like to thank my advisor, Dr. Lonnie Leithold for her incredible patience and constant support throughout this process; I would not have made it through with my sanity intact without her help. I would also like to thank Dr. Karl Wegmann and Dr. Ethan Hyland for always making the time to work through problems and help me produce my best work. I am grateful to have such a supportive and knowledgeable committee guiding me through this process. I would also like to express my gratitude for the team at LacCore, especially Kristina Brady, and Trever Contreras from the Washington Department of Natural Resources. Without their help, this project would not have been possible. Finally, I would like to thank Benjamin F. Lewis, the man who invented the crab pot puller, without which I would not have been able to collect my gravity cores.

TABLE OF CONTENTS

LIST OF TABLES	vii
LIST OF FIGURES.....	viii
1. Introduction	1
1.1. Lake Setting.....	2
1.2. Tectonic and Geologic Setting.....	3
1.3. Historical Earthquakes.....	8
2. Methodology	11
2.1. Sediment Core Collection	11
2.2. Sediment Core Processing	12
2.3. Radiocarbon Sample Preparation.....	13
2.4. Particle Size.....	14
2.5. Diatom Analysis	15
2.6. Loss on Ignition	16
2.7. X-ray Fluorescence Core Scanning.....	17
2.8. Sand Petrology	17
2.9. Statistical approach to Classify Event Layers	18
3. Results	18
3.1. Identification of Event Layers.....	18
3.2. Description of Event Layer 1.....	25
3.2.1. Particle Size	27
3.2.2. Diatom Analysis	30
3.2.3. Sand Petrology	32
3.2.4. XRF Analysis	33
3.2.5. Loss on Ignition	38
3.3. Age-Depth Model.....	39
4. Discussion and Interpretation.....	41
4.1. Interpretation of EL1 and EL2.....	41
4.2. Interpretation of EL3-A	44
4.2.1. Age of Event Layers	48
4.3. Interpretation of Turbidites in SHAKE15.....	49

5. Conclusions	54
5.1. Summary	54
References	55
Appendices	63
Appendix A. Gravity Coring Sites	63
Appendix B. Sand Petrology Point Counts	64
Appendix C. Diatom Counts	65
Appendix D. Loss on Ignition	68
Appendix E. EL3-A Thickness	69
Appendix F. XRF Analysis in EL3-A for 8A-1G and 9A-1G	70
Appendix G. Geophysical profiles alongside core images	72
Appendix H. Identification of event layers in cores from the northern basin.	76
Appendix I. Core image and event layer classification of core 13A-1G	77
Appendix J. Thickness of event layers correlated across multiple gravity cores in the southern basin.	78
Appendix K. Particle size results.....	79
Appendix L. Table of Event Layers.....	82

LIST OF TABLES

Table 1.1	Summary of significant earthquakes.....	10
Table 2.1	Summary of correlated event layers in the southern basin	20
Table 3.1	Summary of radiocarbon dating of materials	38
Table 4.1	Event free length and percentage of core that is composed of event layers determined for each gravity core.	39
Table 5.1	Summary of EL3-A deposits identified in core 6A-1K	53

LIST OF FIGURES

Figure 1.1. Lake Crescent location with respect to Cascadia subduction margin	6
Figure 2.1. Geologic map of Lake Crescent.....	8
Figure 3.1. Historical Earthquakes to Impact Lake Crescent	9
Figure 4.1. Gravity coring sites in Lake Crescent	12
Figure 5.1. Comparison of magnetic susceptibility and particle size	15
Figure 6.1. Profiles of color parameters a^* , b^* , and L for core 6A-1G.....	21
Figure 7.1. Correlation of event layers in cores along north-south transect.....	22
Figure 8.1. Geophysical data for EL2 deposits in core 13A-1G	23
Figure 9.1. Correlation of event layers along the west- east transect	24
Figure 10.1. Profiles of magnetic susceptibility, L^* , a^* , and b^* in EL3-A.....	25
Figure 11.1. Comparison of median, mean, standard deviation, and D90 particle size.....	26
Figure 12.1. Particle size distribution in EL3-A.....	27
Figure 13.1. D90 particle size in EL3-A along west-east transect	28
Figure 14.1. D90 particle size in EL3-A along north-south transect	28
Figure 15.1. P: B in cores along west-east transect	29
Figure 16.1. P: B in EL3-A.....	30
Figure 17.1. Comparison of volcanic-lithic and sedimentary-lithic content at base of EL3-A along west-east transect	31
Figure 18.1. Comparison of volcanic-lithic and sedimentary-lithic content at base of EL3-A along north-south transect.....	31
Figure 19.1. Geochemical ratios in 7A-1G	33
Figure 20.1. Loading plots for PCA run	35
Figure 21.1 <i>PCA(c)</i> model scores.	36

Figure 22.1. Percent loss on ignition from samples in EL3-A along the north-south transect.	37
Figure 23.1. Correlation of EL3-A in cores along west-east transect	38
Figure 24.1. Event Free Age Depth Model in 10A-1G	40
Figure 25.1. Modelled Intensity compared to Event Layer Thickness	43
Figure 26.1. Discharge data from Elwha River Stream Gauge.....	44
Figure 27.1. EL3-A in core 7A-1G alongside data.....	48
Figure 28.1. Visual comparison of EL3-A deposits identified in SHAKE2018 and SHAKE2015 cores.....	51

1. INTRODUCTION

Natural hazard assessment and prediction is heavily dependent on the ability to examine and interpret past records of natural disturbances. Earthquakes can be particularly devastating, often resulting in a sequence of hazards. Ground shaking, landslides, and surface ruptures often spur secondary effects such as tsunamis, seiche events, flooding, liquefaction, or fires (Keefer, 2002; Daniell et al., 2017). Accurately predicting the recurrence of earthquakes from geologic records is paramount to preparing for such an event.

Along the coast of the Pacific Northwest of the United States, geologic evidence of coastal marsh subsidence, tsunami deposits, and deep sea turbidites indicate that there have been numerous Holocene great earthquakes ($M_w > 8.5$) along the Cascadia subduction zone, with a recurrence interval of approximately 500 years (Nelson et al., 2006; Goldfinger et al., 2013; Atwater et al., 2014). The absence of a great earthquake in the past 300 years suggests that the probability of a large earthquake in the next decades is significant (Nelson et al., 2006; Goldfinger et al., 2013; Atwater et al., 2014). Additionally, shallow crustal fault ruptures and deep intraslab earthquakes in the region can have significant impacts on landscapes and infrastructure. Understanding the paleoseismic record of the region is a necessary step to adequately predict and prepare for seismic hazards that may occur in the future.

Turbidites, sedimentary deposits formed by the mobilization of sediments perched on subaqueous slopes via turbidity currents, have been used in paleoseismological investigations conducted in both deep marine and lacustrine environments (Atwater, 1995; Nelson et al., 2000; Goldfinger et al., 2003, 2007, 2012; Karlin et al., 2004; Moernaut, 2010, among others). Studies have shown that turbidite deposits in lakes around the world can be linked to earthquakes, including in central Chile (Moernaut et al., 2014; Van Daele et al., 2015), Switzerland (Hilbe et al., 2014), and western Washington (Karlin & Abella, 2004; Leithold et al., 2019). Examining turbidite frequencies provides constraints on earthquake recurrence intervals that may exceed the limits of instrumental records.

Lake Crescent, located on the Olympic Peninsula in western Washington, offers a unique opportunity to study the paleoseismic history of Cascadia subduction

earthquakes and other seismic events that have impacted the area. The deep, oligotrophic lake is surrounded by steep slopes and is situated such as to record not only ruptures of the Cascadia subduction margin, but also both deep intraslab and shallow crustal earthquakes. Previous studies of Lake Crescent recovered up to 8,500 years of sediment in a suite of nine piston cores containing four distinct types of event layers (Pollen, 2016; Leithold et al, 2019). Most notably, four megaturbidites of up to 2 m thickness were sampled and are each characterized by a sandy base, thick homogenous or graded silt, and thin clay cap, commonly overlying pebbly debris flow deposits. These megaturbidites were interpreted to record the effects of rockslides into the lake triggered by ruptures of the underlying Lake Creek-Boundary Creek fault system. There are also eleven decimeter-scale, silty, normally graded, stacked turbidites, inferred to result from multiple near simultaneous slope failures triggered by earthquake shaking (Pollen, 2016; Leithold et al., 2019). The sources of these earthquakes are uncertain, however. A comparison of event layers that can be tied to historical events may serve as a frame of reference for interpreting event layers found deeper in the middle-late Holocene stratigraphic record. This study aims to examine the past 500 years of sediment accumulation in Lake Crescent to provide a template for interpreting the origin of event deposits formed earlier in its history.

1.1. Lake Setting

Lake Crescent is a deep (190 m maximum) lake located between the Strait of Juan de Fuca and the northern margin of the Olympic Mountains. The lake lies within the boundaries of Olympic National Park and has been protected by the National Park Service since 1939. Renowned for its clarity, Lake Crescent sits at an elevation of about 176 m and has a surface 20.8 km². Approximately 50% of the lake is deeper than 95 m (Moran et al., 2013). Lake Crescent is separated into two major basins. The larger elongated southern basin, which stretches east-west for 4.2 km, narrows near Barnes Creek delta and turns north, opening into the smaller northern basin. Approximately 50% of the subaqueous valley walls surrounding the southern basin exceed 30° inclination. U.S. Highway 101 borders the southern shores of the lake, while the remaining shoreline is occupied by approximately 100 residences in addition to 3

recreational facilities and a National Park campground (Rector and Hallock, 1991). Most of the watershed remains undeveloped. Seasons are mild in the area, lacking extremes in precipitation or temperatures, however precipitation is variable across the watershed. The average precipitation is 336-483 mm per year (Moran et al., 2013).

The watershed surrounding Lake Crescent is approximately 11,000 ha and Lake Crescent comprises about one-fifth of the area. Lake Crescent is fed by 32 tributaries and there is a single outflow, however only 5-6 of the tributary streams are substantial perennial contributors. Barnes Creek is the largest of all the tributaries with a mean discharge of 1.75 m³/s (Moran et al., 2013). Based on radiocarbon geochronology (Moran et al., 2013), the sediment accumulation rate in the southern basin is between 0.84 and 0.93 mm/year while sediment accumulates in the northern basin at about 0.60 mm/year. More recently, Pollen (2016) estimated a sediment accumulation of 0.84 (0.77-0.94) mm/yr using radiocarbon dates from core 6A-1K, located in the middle of the southern basin, consistent with the Moran et al. (2013) sediment accumulation rates.

1.2. Tectonic and Geologic Setting

Lake Crescent is situated above the Cascadia subduction zone, which extends 1,000 km from Vancouver Island to northern California, and within its forearc high, (Fig. 1). The lake lies approximately 200 km east of the Cascadia trench where the Juan de Fuca plate subducts obliquely (45° NE) beneath the North American plate at a rate of ca. 40 mm/yr (Wells et al., 1998, DeMets and Dixon, 1999). Studies have shown that the Cascadia forearc is broken into a series of rigid blocks that rotate in a clockwise direction in response to Pacific-North American shear and extension of the Basin and Range Province (McCaffrey et al, 2007). GPS measurements indicate that relative motions of the Oregon, Western Washington, and Vancouver Island crustal blocks cause permanent north-south oriented shortening in the Puget Sound region at a rate of 4.4 ± 0.3 mm/yr (McCaffrey et al, 2007). This deformation is partially accommodated by shallow crustal fault systems, including the Lake Creek-Boundary Creek Fault zone that runs beneath Lake Crescent (Nelson et al., 2017).

Lake Crescent is one of two large lakes in Olympic National Park. It was once joined with Lake Sutherland to form a larger body of water that drained to the east via

Indian Creek and into the Elwha River. Several massive landslides resulted in the dissection of the ancestral Lake Crescent into the two modern lakes between 4000 and 5000 years ago (Tabor, 1975; Pringle et al., 2010; Joyner, 2016). The rockslide blocked the ancestral drainage, resulting in an increase in water surface elevation (Pringle et al., 2010). Lake Crescent spilled over into a new outlet, now known as the Lyre River, which flows from the northwest corner of the lake north into the Strait of Juan de Fuca.

Great megathrust earthquakes ($M \geq 9$) are a distinct concern for the region. However, there is a lack of written records in western Washington prior to European settlement ca.1774, thus there is a lack of historical documentation of any subduction earthquakes occurring in the region. Geologic evidence of coastal subsidence, turbidites from offshore marine sediment cores, and tsunami deposits in buried tidal marshes indicate the Cascadia subduction zone has generated numerous earthquakes in the last 10,000 years (Goldfinger et al, 2012; Atwater and Hemphill-Haley, 1997; Atwater, 1987). Atwater (1987) first discovered evidence of great earthquakes in tidal mud flats. At least six buried vegetated lowlands were recovered in sediments that have accumulated over the past 3500 years; at least three were overlain by sheets of sand. This was one of the first records that suggested great earthquakes from the Cascadia subduction zone generated tsunamis that were accompanied by up to 2 m of coastal subsidence (Atwater, 1987). The timing of the most recent of these events was later verified using written records of tsunami in Japan that provide a documentation of secondary effects of the event (Satake et al., 1996). Written records from Japan depict large tsunami that occurred on January 27 and 28, 1700, indicating that a Cascadia source event would have occurred about 9 pm local time on January 26, 1700 (Atwater et al., 2005). Dendrochronological studies of forests along the coast of the Pacific Northwest also present evidence consistent with the timing of a 1700 A.D. Cascadia earthquake (Jacoby et al. 1997). Indigenous peoples of the Pacific Northwest share oral traditions that recount experiences of catastrophic events such as tsunamis, earthquakes, and large floods (McMillan et al., 2002). In addition, archeological evidence has been presented that indicates the abandonment of villages along the coast in southern Washington and Oregon (Hutchinson and McMillan, 1997; Hutchinson et al., 2019). In recent decades, a breadth of geological evidence has

emerged that verifies the timing and effects of the 1700 Cascadia earthquake (Goldfinger et al., 2012; Atwater et al. 1995; Jacoby et al. 1997, among others). While the Cascadia subduction zone has been studied since the 1980s, much of the geological evidence used to reconstruct the paleoseismic history of the region comes from southwestern Washington and points further south in Oregon and northern California, and the terrestrial record remains relatively short. Some hypothesize that northern Cascadia ruptures only when the entire margin ruptures, while others conclude that northern Cascadia may sometimes rupture independently of the entire margin and may not always produce great earthquakes (Goldfinger et al., 2016, Hutchinson and Clague, 2017). Thus, there is a need to build upon the regional paleoseismic archive using sediment records that serve to test these alternative hypotheses.

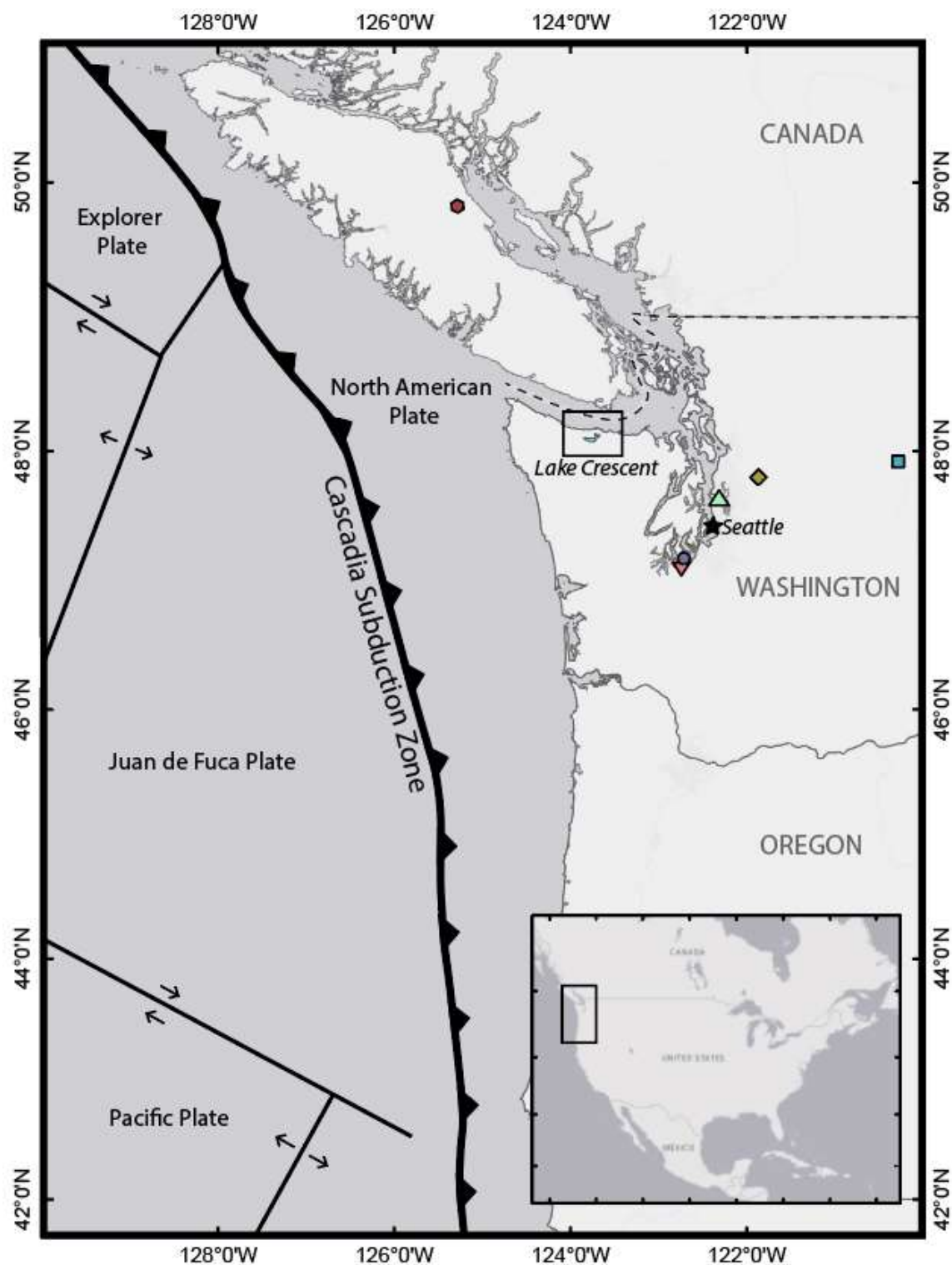


Figure 1. Location of Lake Crescent with respect to the Cascadia subduction zone. Locations of relevant historical earthquakes are indicated by colored markers. Red hexagon- 1946 Vancouver Island (M 7-7.5), Blue square- 1972 Entiat (M 6.5-7), Gold diamond- 1996 Duvall (M 5.3), Green triangle- 1949 Olympia (M 6.7), Purple circle- 2001 Nisqually (M 6.8), Pink inverted triangle- 1965 Tacoma (M 6.8).

The complex geology of the Olympic Peninsula reflects deformation in the Cascadia forearc. The dominant geologic formation is an Eocene basalt, known as the Crescent Formation. Lake Crescent is bordered by the Crescent Formation on the northern and eastern slopes of the southern basin (Fig. 2). The Crescent Formation appears on the Olympic Peninsula in a horseshoe-like shape that is open to the west. The Crescent Formation is composed of lower to middle Eocene volcanic rocks, primarily submarine basalt flows and breccia flows. Filled lava tubes, pillow basalts, and altered palagonite are also common within this unit. Closer to Lake Crescent, interbedded basaltic tuff, siltstone, chert, red argillite, volcanoclastic conglomerate and limestone are present. Marine pillow basalts are found towards the bottom but grade into flow dominated, columnar jointed rocks near the top (Schasse, 2003).

The geologic units adjacent to the southern margin wall of the southern basin consist of Tertiary marine sedimentary rocks, known as the Blue Mountain unit (Tabor and Cady, 1978). The Blue Mountain unit consists of gray to black lithic sandstone, siltstone, and pebble or granule conglomerates (Schasse, 2003). In addition, there are a few areas along the shore where Quaternary mass wasting deposits are present. These deposits consist of Holocene and Pleistocene clays, silts, sands, and gravel talus slopes. Typical of landslide deposits, those along the margin of Lake Crescent are unstratified, broken and poorly-sorted and often contain large boulders or blocks of the adjacent bedrock (Schasse, 2003). Lake Crescent is underlain by three faults, trending east-west and dipping to the north. The Lake-Creek Boundary-Creek Fault and Sadie Creek splay run beneath the northern basin, while the Barnes Creek Fault runs through the southern basin (Tabor and Cady, 1978; Schasse, 2003).

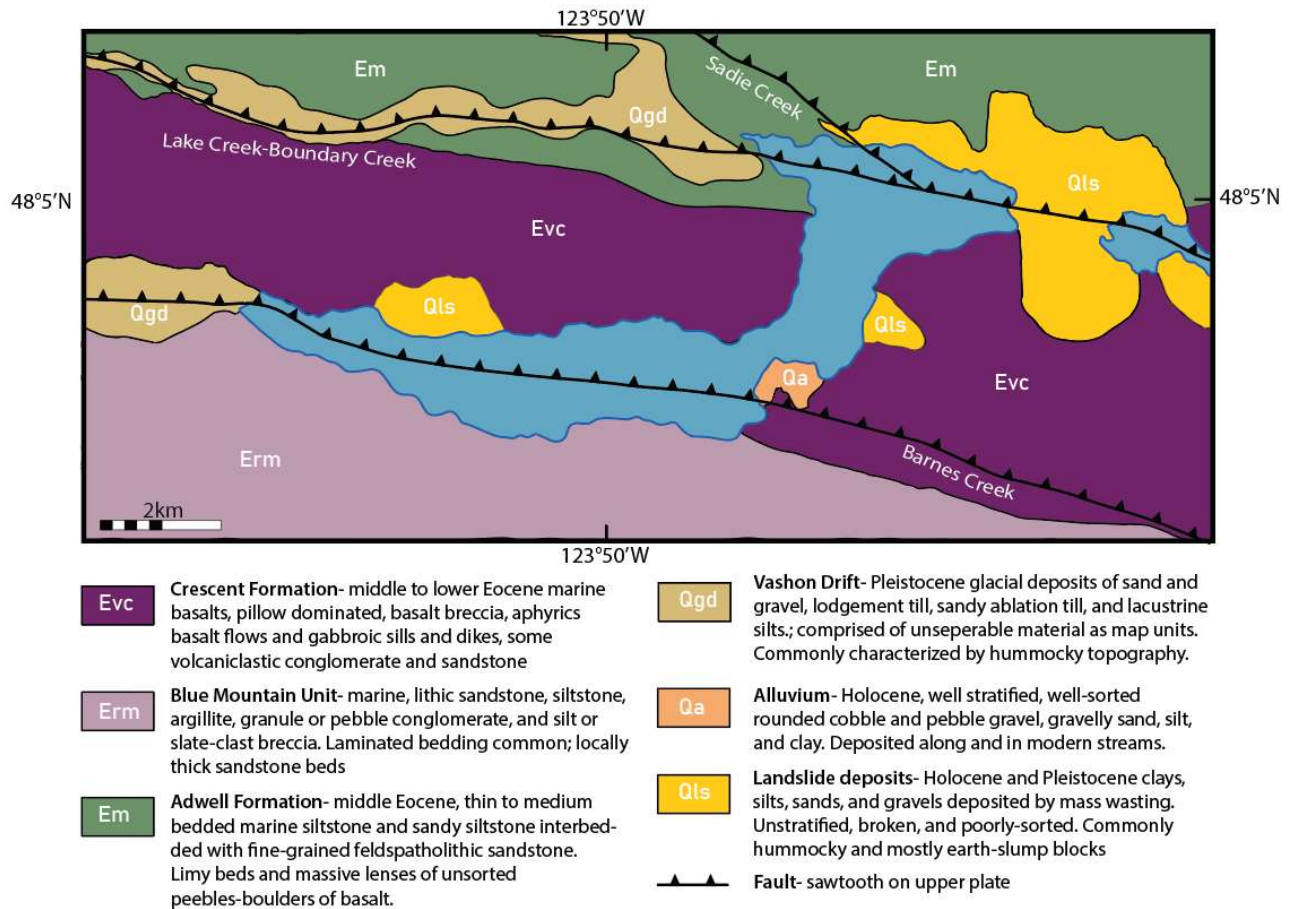


Figure 2. Simplified map of geologic units surrounding Lake Crescent, adapted from Schasse (2003). To the east of Lake Crescent is the once-attached Lake Sutherland.

1.3. Historical Earthquakes

This study attempts to identify event layers or turbidites in the uppermost sediments in Lake Crescent that may be the products of historically documented earthquakes. In order for turbidite-based paleoseismology to work, each earthquake leaving a deposit in the sedimentary record must generate enough energy to trigger turbidity currents (Sumner et al., 2014). Thus, attention is given to historical earthquakes that are known to have generated high magnitudes in the region. A review of earthquakes that occurred in the last century and exceed M5 offers a list of potential events that may be preserved in the sedimentary record of Lake Crescent (Fig. 3).

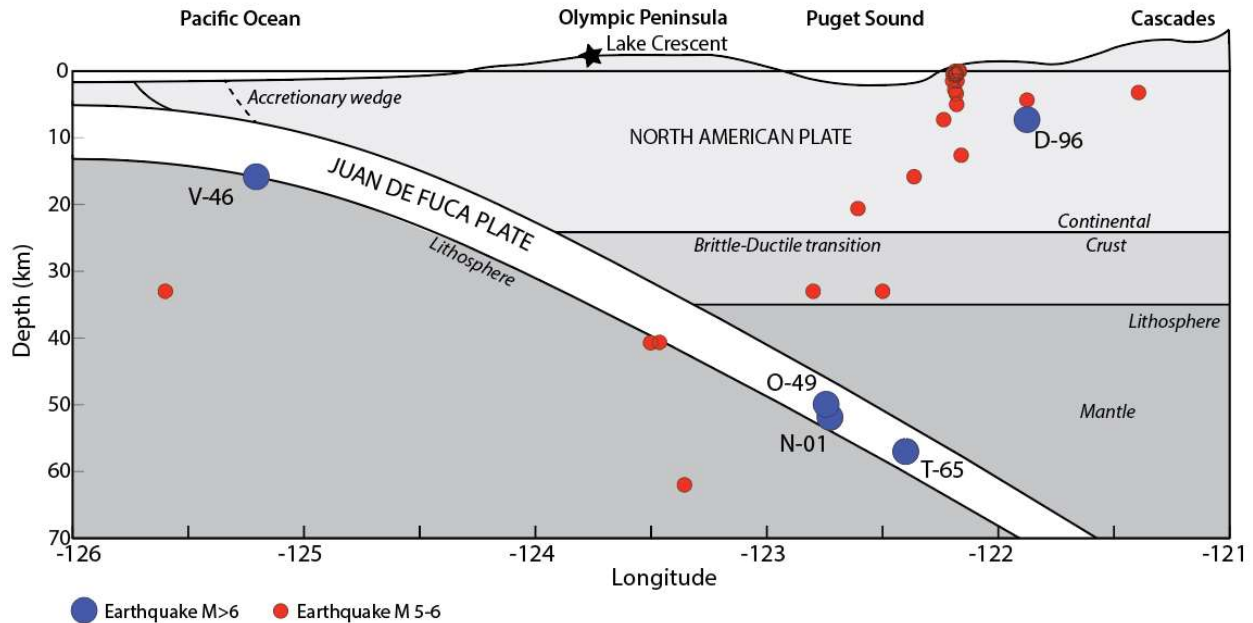


Figure 3. Generalized cross section of Cascadia subduction margin at 48.50' N. Depths of earthquakes ($M > 5$) that occurred between 45°N and 55°N, between 1898 and 2012 are indicated by circle markers (ANSS). The star marker indicates location of Lake Crescent. The approximate depths of the Vancouver Island (V-46), Olympia (O-49), Tacoma (T-65), Duvall (D-96), and Nisqually (N-01) are shown by the blue markers. Note the V-46 is a crustal earthquake that occurred north of 48.50' N, thus when transposed appears in the subducting plate.

Most recently, the Nisqually earthquake (M_w 6.8) occurred on February 28, 2001 between Tacoma and Olympia, WA and was felt across western Washington. This deep intraslab earthquake caused liquefaction and triggered several landslides, resulting in approximately 400 injuries and costing an estimated \$2-4 billion in damages (Highland, 2001). The Seattle-Tacoma (Puget Sound) earthquake was a deep intraslab earthquake that occurred on April 29, 1965 just south of Seattle. With a M_w 6.5-6.7, the event was felt from Oregon to British Columbia and Montana. Intense shaking caused the collapse of numerous buildings on Seattle's Harbor Island, slumping, and at least 7 deaths, causing over \$12.5 million (ca. \$100 million in 2018) in damages (Washington Military Dept., 2015). Prior to the Tacoma earthquake was the 1949 Olympia earthquake (M_w 6.8-7.0), which occurred about 8 miles northeast of Olympia along the southern edge of the Puget Sound. A USGS report noted that most buildings in Olympia were damaged from liquefaction and severe ground shaking, killing 8 people, injuring many, and costing an estimated \$25 million (ca. \$265 million in 2018) in damages (Washington

Military Dept., 2015). The Duvall earthquake (M_w 5.3) occurred May 2, 1996 near Duvall, WA. The Duvall event was reportedly felt by many residents from Olympia to southern British Columbia and resulted in some building damage. More than 45 aftershocks of ($M \geq 2$) and 6 events ($M \geq 3$) occurred within the first 3 days (PNSN, 2019). On June 23, 1946, the Vancouver Island earthquake (M_w 7.3) struck on the Forbidden Plateau in central Vancouver and was felt across the region, including in Portland, Oregon and Prince Rupert, British Columbia. Communities west of Campbell River sustained major damage, knocking over 75% of the chimneys in the closest towns and a few in Victoria (PNSN, 2019). The earliest of the earthquakes occurred near Columbia River town of Entiat east of the Cascade Crest in the year 1872 and was felt over 390,000 mi^2 . The shallow Entiat or Washington State earthquake (estimated M_w 6.5-7.5) caused landslides, toppled trees, and created a fissure south of Seattle (Bakun et al., 2002).

Table 1. Summary of significant historical earthquakes with high magnitudes and within proximity to Lake Crescent.

Name	Date	Location	Distance to Lake Crescent (km)	Magnitude	Mercalli Intensity	Depth (km)
Entiat	December 14, 1872	47° 54' 0" N, 120° 18' 0" W	263	6.5-7	IX	NA
Vancouver Island	June 23, 1946	49° 37' 12" N, 125° 15' 36" W	204	7-7.5	VI-VII	~15
Olympia	April 13, 1949	47° 0' 0" N, 122° 31' 48" W	153	6.7	VII	50
Seattle-Tacoma	April 29, 1965	47° 0' 0" N, 122° 31' 48" W	153	6.7	VIII	59
Nisqually	February 28, 2001	47° 11' 24" N, 122° 39' 36" W	130	6.8	VIII	57
Duvall	May 2, 1996	47.76 N, 121.85 W	150	5.3	VII	~7

2. METHODS

2.1 Sediment Core Collection

A suite of thirteen gravity cores was collected from Lake Crescent in May of 2018 with the assistance of the Washington State Department of Natural Resources (DNR). Coring sites were selected based on locations of previously collected piston cores. Four cores were collected from the northern lake basin and nine were collected from the southern basin, ranging from 0.6-0.8 m in length. Cores were collected along north-south and west-east transects in the southern basin (Fig.4). The gravity corer consisted of a weighted metal head (5.4 kilograms) to which one meter of polycarbonate tubing with an inner diameter of 70 mm was attached. The device was lowered on a rope to the lakebed from a small boat that was maneuvered to maintain position and compensate for drift during deployment and recovery. Once the device was retrieved, the tube was capped by hand at the base before breaching the water surface. The top of the core was capped once the device was detached on board the boat. In a few cases, the tubes penetrated into the lakebed beyond the top of the core tubes, and sediment overflowed as the coring device was removed from the tubing. As a result, those cores did not preserve the sediment-water interface. At a few coring locations in the lake, where water depth was nearing 190 m and the rope reached its maximum length, the corer was unable to collect a full tube of sediment. Zorbitrol, sodium polyacrylate absorbent powder, was used to fill the remaining space in the tubes when necessary to preserve the sediment-water interface during transport. Core tubes were cut above the sediments in some cases in preparation for shipping to the National Lacustrine Core Facility (LacCore) in Minneapolis, Minnesota.

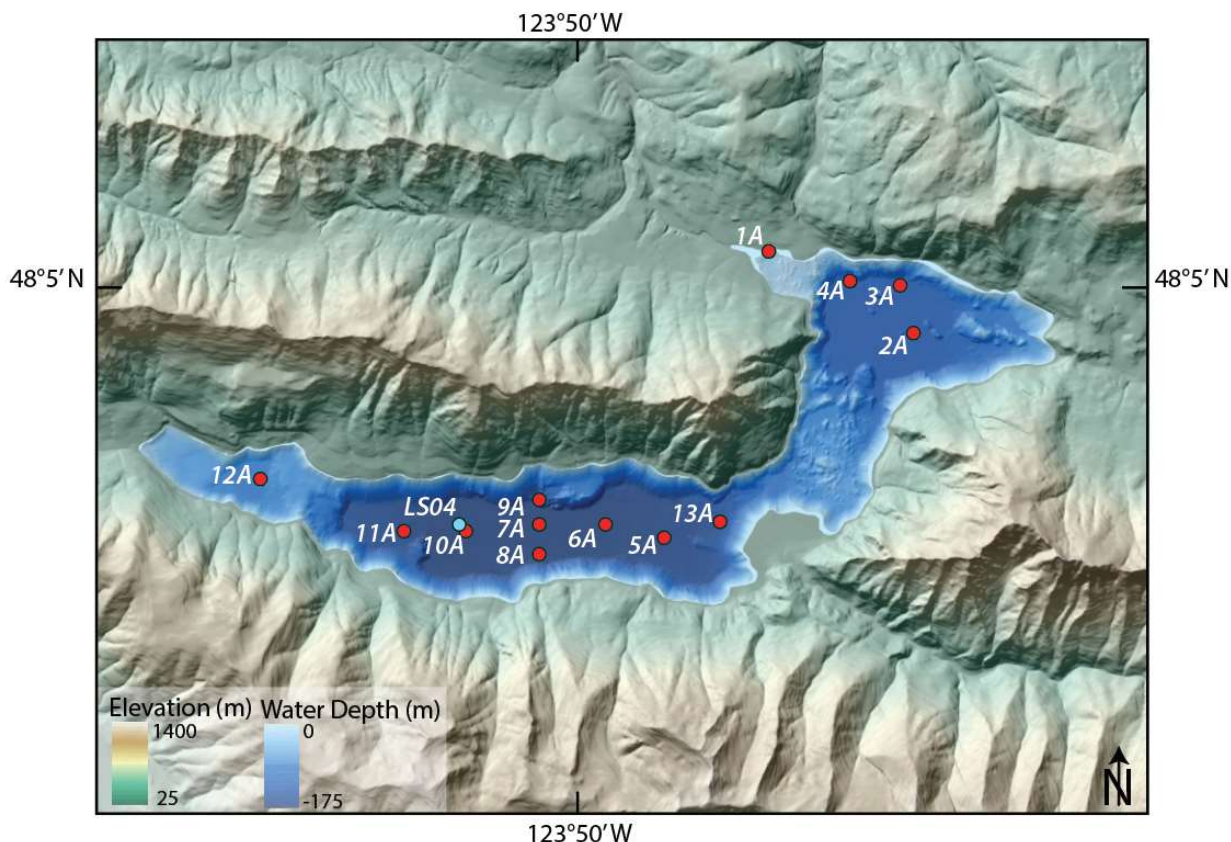


Figure 4. Map of sites where gravity cores were collected in May 2018. Red circles indicate coring sites. The LS04 coring site from the Moran et al. (2013) study is indicated by the blue circle.

2.2 Sediment Core Processing

Cores were scanned using the Geotek multi-sensor core logger (MSCL) upon arrival at the LacCore (National Lacustrine Coring) facility in Minneapolis, Minnesota. The multi-sensor core logger measured sediment density, acoustic wave velocity, electrical resistivity, and loop-sensor magnetic susceptibility at a 1 cm resolution. Cores were then split into working and archive halves using two medical cast saws. Utility box cutters were used to remove polycarbonate shredding from cores. Both halves were placed on a Schnurrenberger-Hillesheim device (Wagner modification), where two guillotines were wedged between the halves while the utility knife was used to cut the endcaps. The guillotine panels were used to remove excess sediment from each half. Using a rounded glass slide, the surface of the working and archive halves were smoothed until each half was level. The working half of each core was photographed using Geotek Geoscan-III, a digital line scanner, at 10 pixels/mm or ~300dpi. The

archived halves were scanned using the Geotek MSCL-XYZ core scanner for high-resolution point-sensor magnetic susceptibility and color spectra. Color parameters are useful to characterize the color of sediments quantitatively. L^* is used to quantify lightness or luminescence (Debret et al., 2006). The reflectance values for a^* is an indicator of red/green variation, where an increase in a^* indicates redness. The values for b^* reflect blue/yellow variation (Debret et al., 2006). Corelyzer software was used to display core images at 508 dpi while examining cores during the sampling process. The working half of each core was sampled for radiocarbon dating (^{14}C). The cores were also sampled for particle size and compositional analyses at 10-15 cm intervals. Event layers observed were sampled at 1 cm intervals. The upper 15 cm of cores 10A-1G, 7A-1G, and 4A-1G was collected from both halves at 1 cm increments for ^{210}Pb dating. Subsamples were frozen and shipped to the sedimentology lab at North Carolina State University.

2.3 Radiocarbon Sample Preparation

Eight organic matter samples were thawed for one hour prior to the start of sample preparation. Samples collected from above, below, and within a turbidite identified in cores 7A-1G and 10A-1G were selected for standard acid-base-acid pretreatment following the protocol of Olsson, 1986. Samples were rinsed in a fine mesh, stainless steel sieve with deionized, carbon-free water. The sieve was rinsed with methanol, acetone, methanol, and deionized water again between samples. A warm bath was maintained at $\sim 65\text{-}70^\circ\text{C}$ on a hot plate. Samples were each transferred to a 50 mL glass beaker, covered with foil, and submerged in 1 N hydrochloric acid, then placed in the bath for 30 minutes. After 30 minutes, a separate, clean syringe assigned to each beaker was used to remove the hydrochloric acid. Sodium hydroxide (1 N) was then added to each beaker so that the sample was submerged and the beaker was then placed in the warm bath for an hour. Every hour the NaOH was removed with the assigned syringe and replaced with new NaOH until the liquid in the beaker appeared clear. This was repeated 6-29 times depending on the amount of sample and sample type. Once the liquid was clear, NaOH was removed and replaced with enough HCl to submerge the sample for 30 minutes. The sample was then rinsed using deionized water. Every 5 minutes the water was replaced and the pH was checked using paper

strips until the solution was neutral. This was done up to 17 times for some samples. All liquid was finally removed and the sample was dried on the hotplate. The dried samples were then packaged in small glass vials that had previously been combusted at 500°C and were sent to the National Ocean Sciences Accelerator Mass Spectrometer facility (NOSAMS) at Woods Hole Institute of Oceanography for radiocarbon analysis. The radiocarbon dates received from NOSAMS were calibrated using the Calib ^{14}C Calibration Program 7.10 and the IntCal13 curve (Reimer et al., 2013). Sediment accumulation rates determined using ^{14}C data from Lake Crescent published by Moran et al. (2012) were also used in constraining the ages of event layers observed in the cores. The sediment accumulation rates were determined using ^{14}C from a box core (LS04) that was recovered by Moran et al. (2012) very close to the recovery site of core 10A-1G in this study (Fig. 4).

2.4 Particle Size

Particle size analysis was performed on subsamples of sediment, using a Beckman Coulter LS 13-320 laser diffraction particle size analyzer. Sediment samples were thawed for one hour prior to analyses. Approximately 50 mg of sample was added to a 50 mL glass beaker with ~30 mL of deionized water and small magnetic stir bar. The beaker was placed on a magnetic stir plate for 1-2 minutes. Using a disposable plastic pipette, small volumes of sample were introduced to the analyzer until the Polarizing Intensity Differential Scattering (PIDS) obscuration reached 40%. The analyzer measured the particle size distribution from 0.04-2000 micrometers; thus, any coarser particles were not accounted for. Magnetic susceptibility was used as a proxy for grain size and guided the selection of samples for particle size analysis throughout the cores at a 1 cm resolution (Booth et al., 2005; Fig. 5).

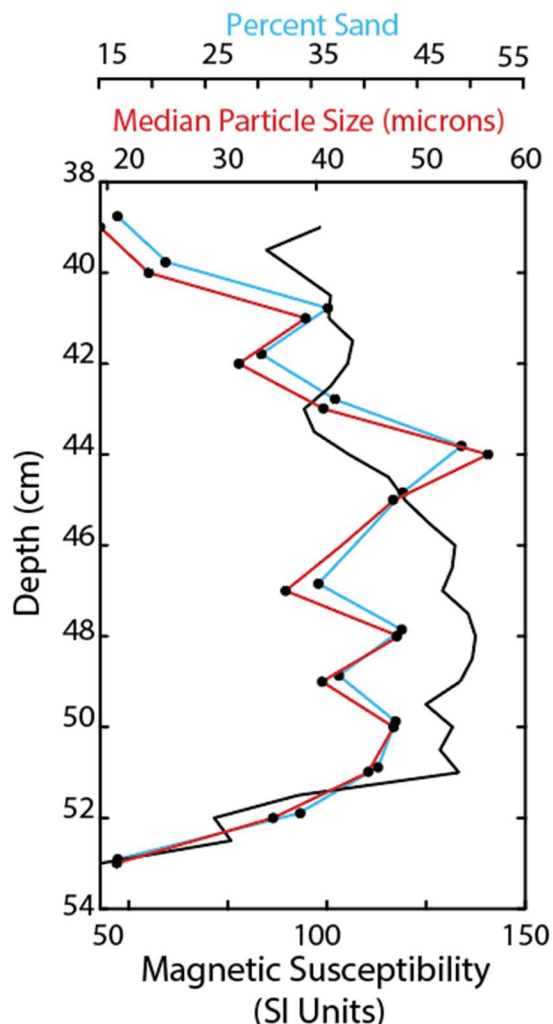


Figure 5. Percent sand, shown by the red line, and magnetic susceptibility, shown by black line, in the thickest event layer identified in core 7A-1G between 38.5 and 53.5 cm depth. The correlation coefficient between percent sand and magnetic susceptibility is 0.55, suggesting magnetic susceptibility may be used as a proxy to approximate particle size. Median particle size is shown by the blue line. The correlation coefficient between median particle size and magnetic susceptibility is 0.63.

2.5 Diatom Analysis

Diatom smear slides were created for a suite of 27 samples (Appendix C). A toothpick was used to collect a small amount of sample and place it on a glass slide with 2-3 drops of deionized water. The sediment was evenly distributed on the slide using the toothpick. The glass slide was placed on a hot plate set to a low temperature setting until dry. 1-2 drops of mounting medium were added on top of the dried sediment. A glass cover was pressed on top of the medium to spread it out on the slide.

The slide was then placed under an ultraviolet light to cure for 3-5 minutes. Once the mounting medium was dried, the slide was stored in a box until the number of planktonic and benthic diatoms were counted using a Nikon Eclipse compound and petrographic microscope, equipped with a motorized stage and Nikon DS color digital camera. Diatoms were visible at 40x magnification. An area of each slide with evenly distributed sediment was identified and the stage was systematically moved along the X and Y axes until at least 400 unique diatoms were counted. Planktonic diatoms were classified based on their centric morphology and presence of radial symmetry. Benthic diatoms exhibit a pennate morphology, indicated by bilateral symmetry. The percentage of planktonic taxa was determined using the following equation (Kroon et al., 1993).

$$\% \text{ Planktonic} = \frac{\sum \text{planktonic taxa}}{\sum \text{planktonic taxa and benthic taxa}} \times 100$$

Each count was performed three times to ensure reproducibility and consistent identification. The degree of diatom preservation was also estimated qualitatively based on the relief of the silica casing and abundance of fragmented or broken diatom valves. A qualitative estimate of the total abundance of diatoms was noted for each sample (Appendix C).

2.6 Loss on Ignition

Total organic carbon in samples from cores 7A-1G, 8A-1G, and 9A-1G was estimated by loss on ignition. Samples were thawed approximately 1 hour prior to analyses. Approximately 1 gram of sediment from each sample was weighed out in glass vials and covered with aluminum foil (wet weight). Samples were then freeze-dried for 18 hours, and then weighed again (dry weight). The difference in wet weight and dry weight is used to determine the percentage of moisture and dry sediment content (Hieri et al., 2001). Samples were then baked in a kiln at 510°C for 2 hours. Once cooled, the samples were weighed (baked weight) to estimate the percentage of total organic matter (Catianis et al., 2014). It was assumed the percent carbonate is negligible based on the lack of carbonate facies in the surrounding geology. The percent loss on ignition was calculated using the following formula (Dean, 1974).

$$\% \text{LOI} = \frac{\text{dry weight} - \text{baked weight}}{\text{dry weight}} \times 100$$

2.7 X-ray Fluorescence Core Scanning

The elemental composition was measured for selected samples using x-ray fluorescence (XRF). Subsamples collected from the gravity cores were scanned individually using a Bruker TRACER 5i handheld XRF spectrometer. Samples were thawed 1 hour prior to measurements. Using a steel spatula, the sample was placed on a small segment of commercial polyethylene film (Saran Wrap). The excess film was folded over the top of the sample, so the base of the sample was covered by a single layer. Each sample was flattened and smoothed on one side and placed on the detector window of the TRACER 5i. Each sample was scanned 5 times for 60 seconds to measure 17 major elements, using the Oxide3 phase and Geo-exploration setting. Between each sample run, the sample was rotated slightly on the detector window to ensure each scan was not biased to the elemental composition of a singular grain or the covering film. Elemental data was calibrated using a USGS “mudstone” standard (SGR-1) and statistical standardization via ARTAX software (Bruker, 2015).

2.8 Sand Petrology

Thin sections were prepared for samples found at the base of an event layer (See Appendix A). Prior to preparation, samples were thawed for one hour. Samples were rinsed with deionized water repeatedly in a 125 μm stainless steel sieve to remove finer material. The >125 micron fraction was then placed into a 50 mL glass beaker. Samples were covered and baked in an oven for 3-4 hours at low heat until dry throughout. Dried samples were removed from the beaker and funneled into a plastic 50 mL vial. The sample was then submerged in a sodium polytungstate (PST) solution (density= 1.6 g cm^{-3}), and the samples were shaken for 30 seconds to allow materials to mix. Samples were covered and allowed to settle overnight (~24 hours) giving ample time for plant debris with density <1.6 to float to the surface. After 24 hours, the floating organic material was decanted, and the sand that collected on the bottom of the vials was rinsed through a standard commercial coffee filter to remove the PST. Each sample was rinsed until water was clear to ensure the PST was removed. Sediment was then rinsed from the coffee filter, placed into 50 mL beakers and baked at low heat until dry throughout. Once dry, samples were placed into small plastic vials with caps and sealed with parafilm. The samples were sent to National Petrographic Service Inc. in

Rosenberg Texas, where they were embedded in clear epoxy and cut into thin sections. Once thin sections were produced, each was examined for mineral composition. A mineral point-count was performed to estimate the percentages of volcanic lithic and sedimentary lithic grains. 300 points were counted per section to ensure an acceptable level of precision (Galehouse, 1971). Each count was performed twice to ensure reproducibility.

2.9 Statistical Approach to Classify Event Layers

A series of principal component analyses was performed using MATLAB software (MathWorks, 2019), in an attempt to distinguish different types of event layers from background sediment. A principal component analysis aims to maximize the variance within data along two principal components based on high-resolution geophysical logging and geochemical data. Thirteen iterations of the analyses were performed, each informed by various combinations of geophysical and geochemical, and color parameters.

3. RESULTS

3.1 Identification of Event Layers



























































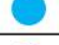




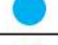

















The uppermost 0.8 meters of sediment in Lake Crescent contains numerous event layers. The “steady-state” or “background” sedimentation is represented by the diatom-rich, finely laminated to massive, light tan-brown, fine silt that dominates the majority of the gravity cores. There are no annual varves visible in the background sediments, which are a mixture of detrital particles delivered from the surrounding catchment from streams and surface runoff along with diatom frustules primarily derived from in-lake productivity. Small fragments of terrestrial plant debris are disseminated throughout the background sediments.

In contrast, event layers interstratified with the background sediments are characterized by abrupt basal contacts marked by increases in grain size and color change. The upper contacts of these layers tend to be more gradual, with progressive upward fining into background sediment in most cases. In some cases, the tops of the layers are characterized by a fine clay cap. Multiple event layers are present in every core collected from Lake Crescent, however the color and structure of the event layers

are variable across the basin. Most event layers can only be correlated between a few cores. Event layer thickness and distribution with depth varies amongst the cores (Table 2). Cores collected near the delta contain a higher number of event layers. Event layers found in the gravity cores are often indicated by an increase in the magnetic susceptibility and density in geophysical logs. Three types of event layers were identified in the gravity cores and correlated across the lake basin.

Event layers in the cores are classified based on thickness and color. Event layer type one (EL1) was indicated by a relative increase in magnetic susceptibility and density compared to background sediments (Appendix G). EL1 layers range from 1-4 cm in thickness and are mostly composed of sand-sized grains. EL1 layers appear red-brown or dark-colored. There is an observed decrease in color parameter L^* and an increase in a^* (Fig. 6).

Table 2. Summary of correlated event layers in the southern basin, including color, range of thickness, qualitative particle size, and relative magnetic susceptibility response. Magnetic susceptibility response is indicated by the color, darker blue represents a very high response and light blue shows a low response. Particle size is shown by the diameter of circles, ranging from coarse sand to silt sized-grains. Boxes are empty when an event layer was not identified in a particular core.

Event Layer ID	Event Layer Thickness (cm)	Color	West-East Transect						North-South Transect		
			12A-1G	11A-1G	10A-1G	7A-1G	6A-1G	5A-1G	9A-1G	7A-1G	8A-1G
EL1-A	0.5-3	Red-brown to dark brown; light-colored clay cap									
EL1-B	1-4.5	Red-brown to dark brown; light-colored clay cap									
EL1-C	1-3	Red-brown to light brown									
EL1-D	2-3	Dark to light brown									
EL1-E	0.5-4	Dark-colored									
EL1-F	0.5	Black to dark brown									
EL3-A	1-15	Black to red brown; light-colored clay cap									
EL1-G	0.5-1	Dark red-brown; light colored clay cap									
EL1-H	0.5-2.5	Dark red-brown to black									
EL1-I	0.5-1.5	Black to dark brown									
EL1-J	0.5-1.5	Black to dark brown									
EL1-K	1-2	Dark red-brown to black									
EL1-L	1.5-3	Red-brown to light brown; light-colored clay cap									
EL1-M	0.5	Light brown to red-brown									
EL1-N	0.5	Red-brown									

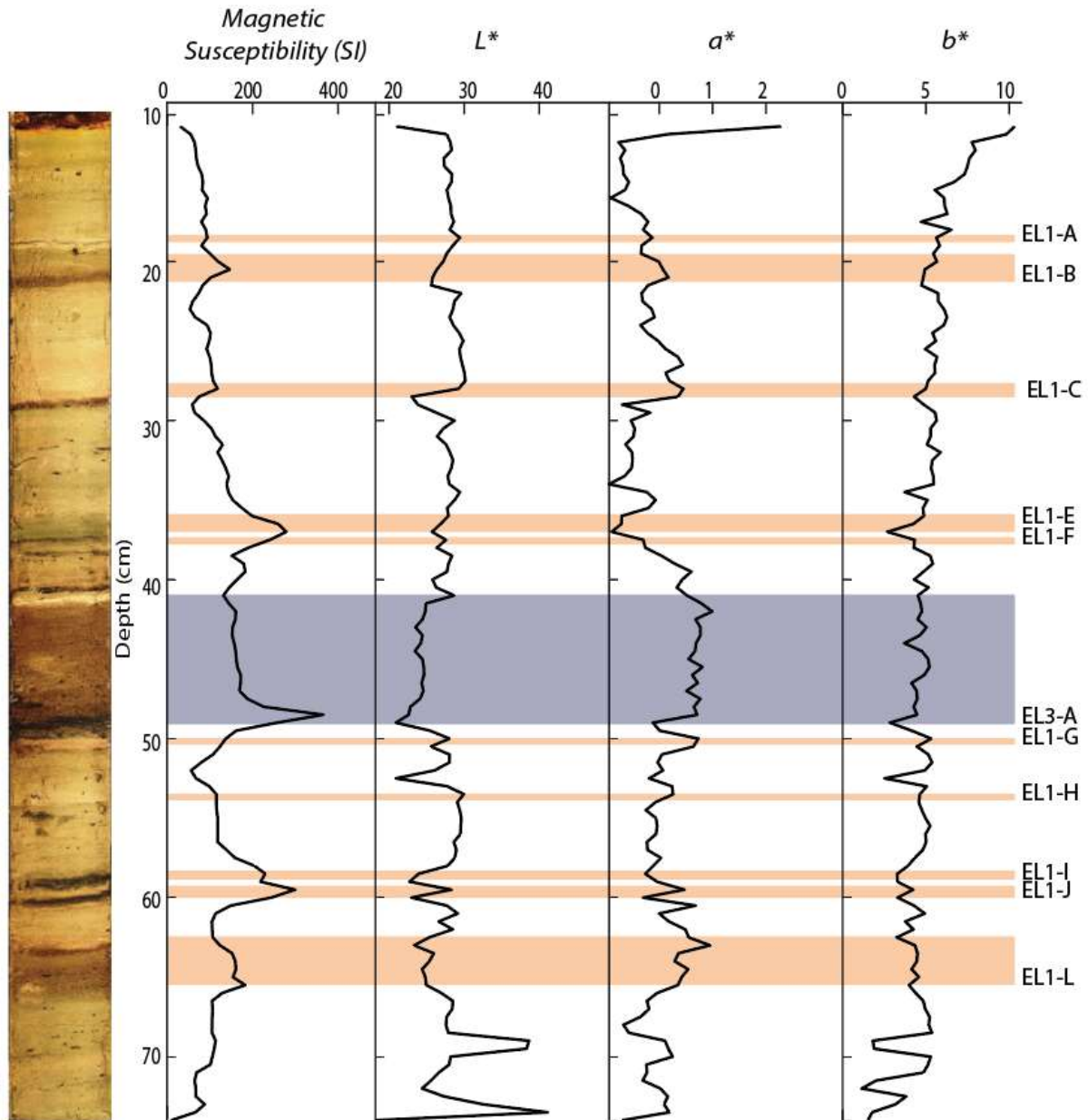


Figure 6. Profiles of color parameters a^* , b^* , and L^* with depth for core 6A-1G alongside core image. The purple shading represents EL3-A. Orange shading indicates the presence of EL1 deposits.

The thickest EL1 deposit is 4 cm thick and found in core 5A-1G. Plant debris is commonly incorporated throughout the deposit. Most EL1 layers are thin red-brown laminae, often identified by an increase in color parameter a^* (Fig. 6). Other EL1 deposits are thin (0.5-1.5 cm thick) and dark-colored. EL1 layers may be capped by thin clay laminae.

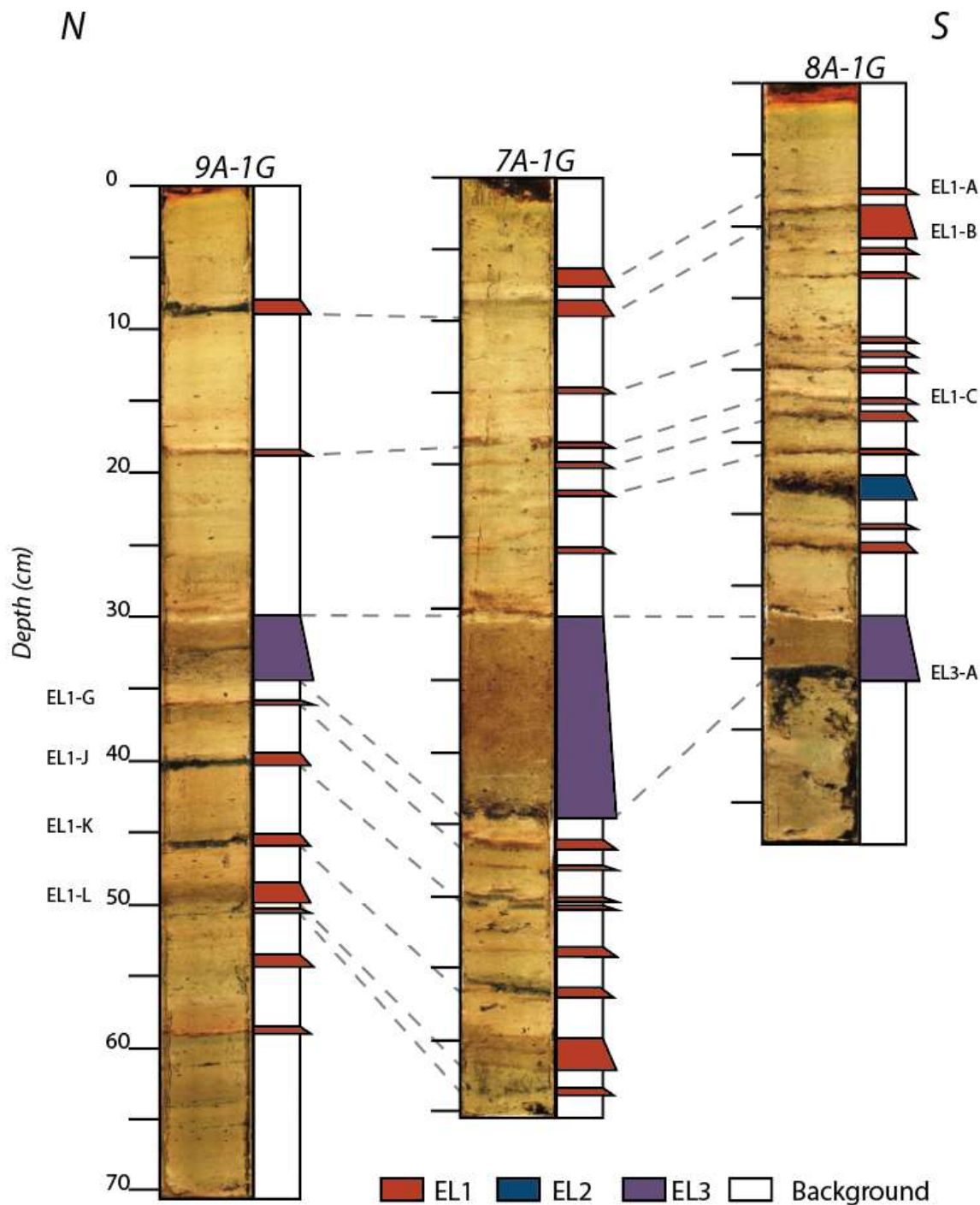


Figure 7. Correlation of event layers in cores 9A-1G, 7A-1G, and 8A-1G, respectively along the north-south transect in the southern basin. Cores are hung on the top of EL3-A. Tick mark intervals depict 5 cm in depth from top of the core. The base of 8A-1G was partially disturbed during recovery.

The top of 8A-1G contains ten EL1 layers, while the base of 8A-1G is disturbed, distorting the presence of any event layers. Core 9A-1G has at least seven EL1 layers

(Fig. 7). In the upper 10 cm of cores 11A-1G and 5A-1G, thin EL1 deposits, EL1-A and EL1-B, are both overlain by additional thin coarse pulses (Fig. 7). However, the thin EL1 deposits are not overlain by a shared clay cap. Two EL1 layers were correlated between the three cores along the north-south transect (Fig. 7). At least nine EL1 deposits can be correlated between two of the cores along the N-S transect.

The second type of event layer in the cores, designated EL2, exhibit a significant decrease in bulk density relative to underlying and overlying sediments and an upward decrease in magnetic susceptibility. EL2 deposits are dominated by terrestrial plant material. This type of layer was only identified in cores 13A-1G and 8A-1G, which are close to the Barnes Creek delta and southern shoreline respectively. There was a maximum of five unique EL2 deposits identified. Event layers were correlated along the west-east transect in the southern basin (Fig. 7).

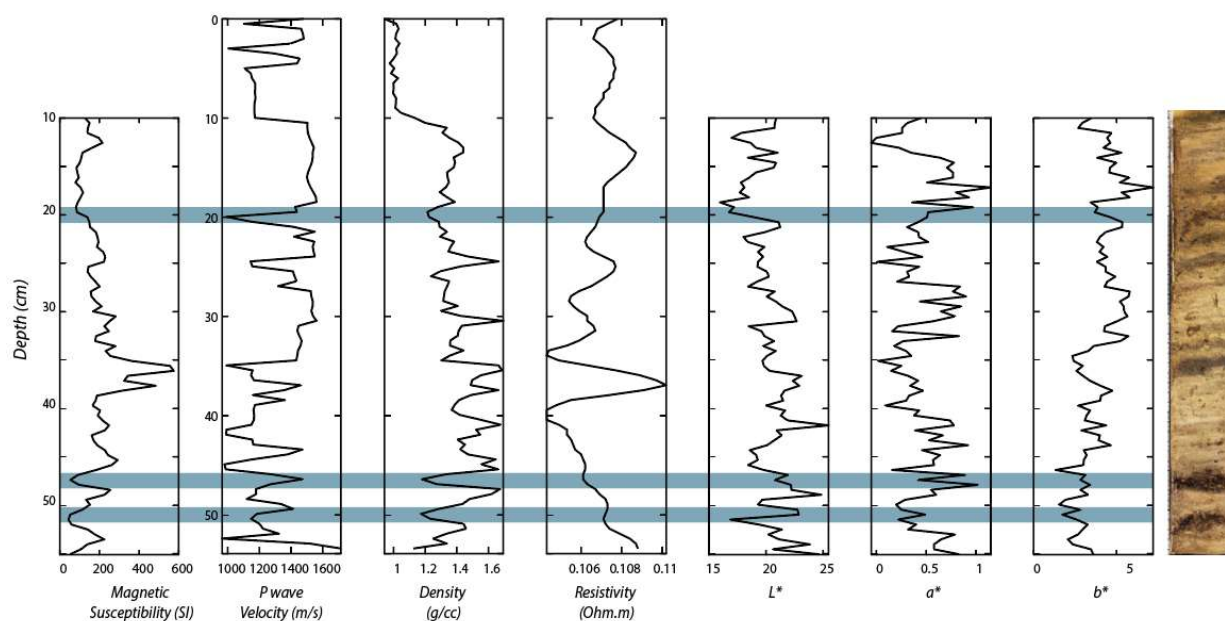


Figure 8. Core 13A-1G shown alongside geophysical data and color parameter profiles. EL2 deposits are highlighted in dark blue lines. EL2 deposits are dominated by woody debris. EL2 deposits are indicated by an abrupt negative response to magnetic susceptibility and low bulk density, consistent with the amount of observed void space.

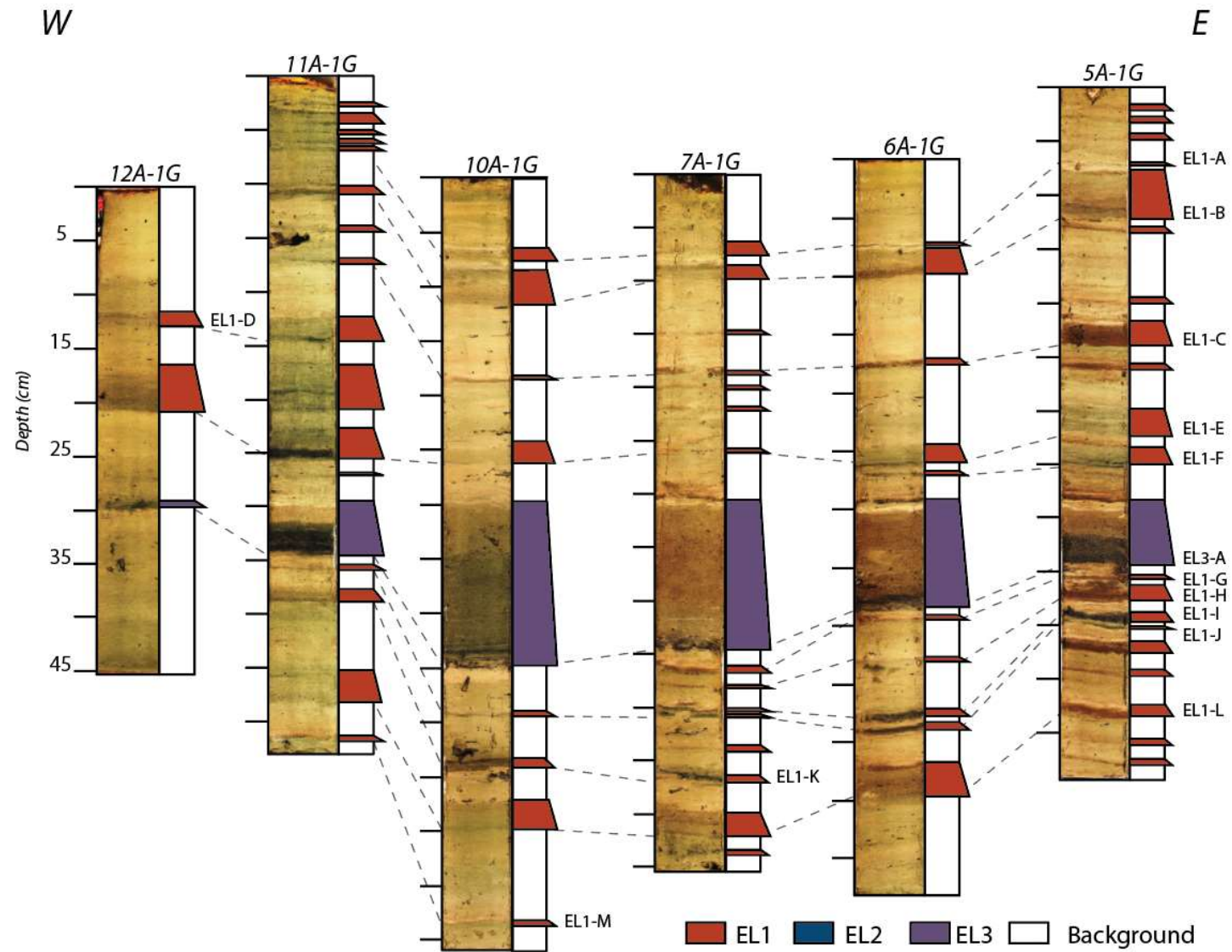


Figure 9. Correlation of event layers along the west- east transect and proposed classification of sediment deposits. Cores are hung on the top of EL3-A.

3.2 Characterization of Event Layer 3 (EL3-A)

Of the numerous event layers present in the cores, the most prominent is EL3-A, observed across the southern basin (Fig. 10). EL3-A is present in cores 5A-1G to 12A-1G and is found at varying depths and thickness (3 to 15 cm) in cores collected from the southern basin (Fig. 9). The sharp base of EL3-A is dark-colored and visibly coarse. The basal contact of EL3-A is also indicated in the geophysical profiles by an abrupt increase in acoustic velocity, bulk density, and magnetic susceptibility, exemplified in core 10A-1G (Fig. 10). Color parameters L^* , a^* , and b^* exhibit a sudden decrease at the base of EL3-A (Fig. 10). L^* , a^* , and b^* are relatively uniform in the lower half of the layer and then gradually increase upward. This pattern was observed in EL3-A across the basin.

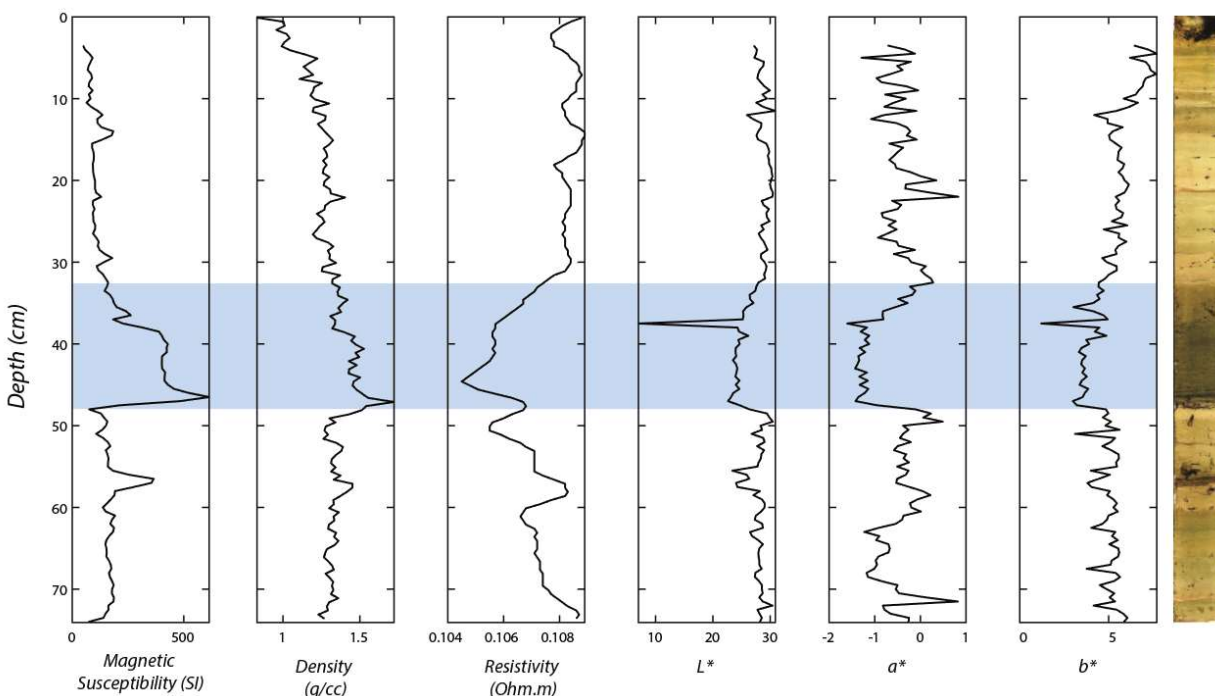


Figure 10. Profiles of magnetic susceptibility, L^* , a^* , and b^* measured during split core logging. Bulk density and resistivity profiles measured using whole core logger for core 10A-1G. EL3-A is highlighted in blue.

3.2.1 Particle Size Analysis

D90 particle size was used to interpret trends in EL3-A vertically and across the southern basin. D90 describes the diameter of the 90th percentile of particles in a particle size distribution, i.e., the diameter of the 10% coarsest particles. Examination of

particle size trends through EL3-A indicate median, mean, standard deviation, and D90 reveal similar trends, however trends in D90 grain size with depth are more pronounced (Fig. 11).

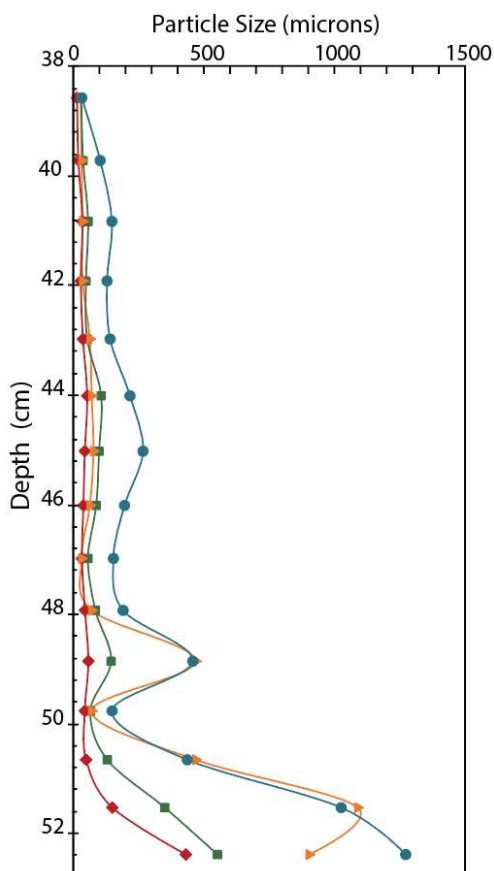


Figure 11. Comparison of median (red diamond), mean (orange diamond), standard deviation (green square), and D90 (blue circle) particle size trends in EL3-A from core 7A-1G.

The base of the EL3-A is abrupt and composed of poorly-sorted fine gravel, sand, and coarse silt. Fine to medium-sized gravel was observed in cores 8A-1G and 10A-1G during sample preparation. There is also evidence that indicates the deposition of EL3-A may have disturbed the underlying sediment in core 8A-1G. The sediment beneath EL3-A in 8A-1G appears overturned or disturbed. The particle size results indicated particle size coarsens, then fines upward in the layer. There were two fining-upward sequences observed in cores along the west-east transect of the southern basin, 10A-1G, 7A-1G, 6A-1G, and 5A-1G (Appendix K). The particle size analysis of core 7A-1G revealed a coarse sandy pulse in the middle of the deposit (Fig. 12). The

second coarse pulse was not detected in 9A-1G and was less apparent in 8A-1G (Appendix K).

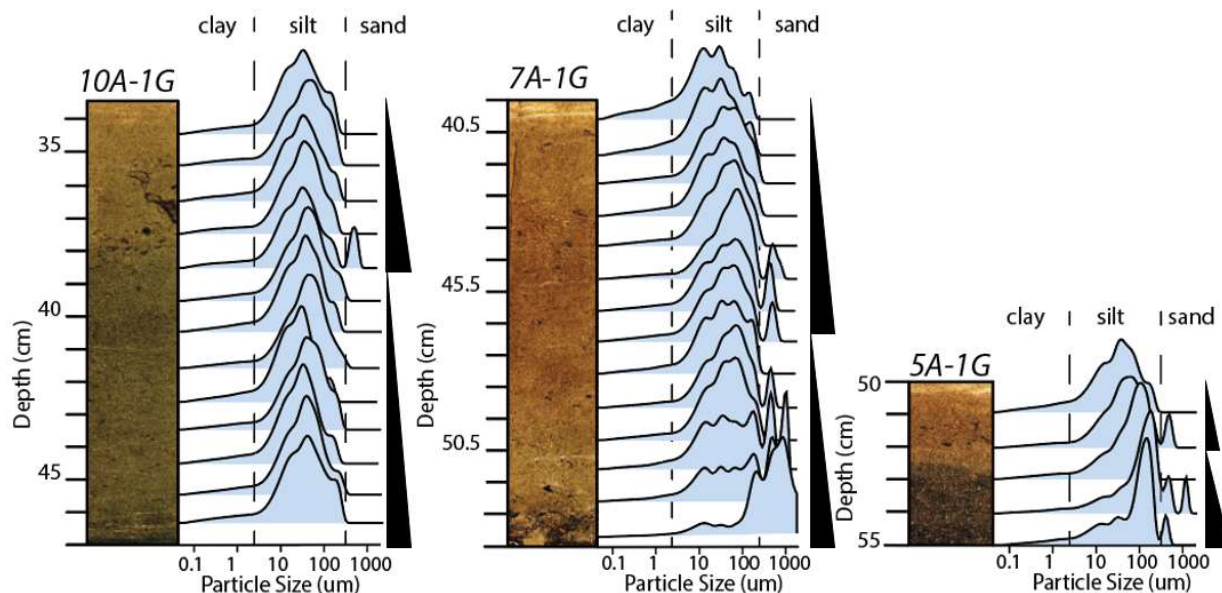


Figure 12. Particle size distribution (blue lines) in EL3-A from core 10A-1G, 7A-1G, and 5A-1G shown alongside core images. Black triangles indicate fining-upward sequences observed.

The particle size of the turbidite varied across the southern lake basin. D90 particle size measured at the base and top of EL3-A increased towards the east, with proximity to the delta (Fig. 13). D90 particle size at the base and top of EL3-A also increased towards the southern slope based on measurements of EL3-A in cores 9A-1G, 7A-1G, and 8A-1G (Fig. 14).

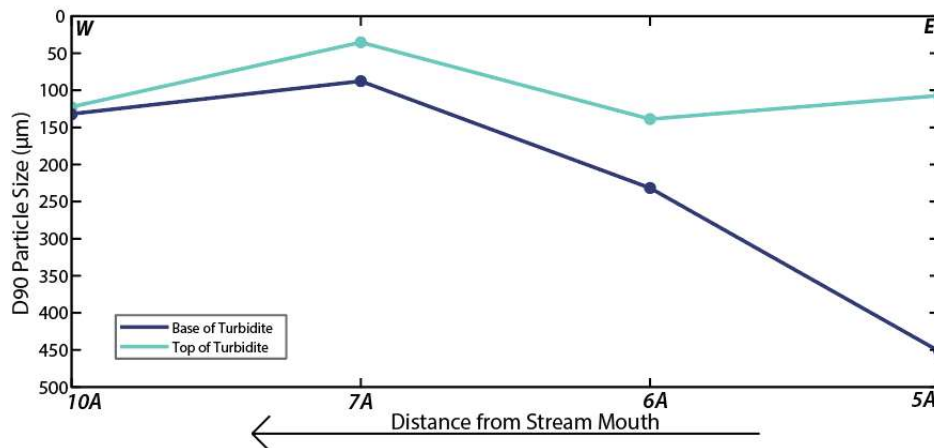


Figure 13. D90 particle size in EL3-A observed in four cores collected across the southern basin along the west-east transect. Standard deviation for the D90 particle size at the base of the turbidite is 162.2. The standard deviation towards the top of the turbidite is 45.3.

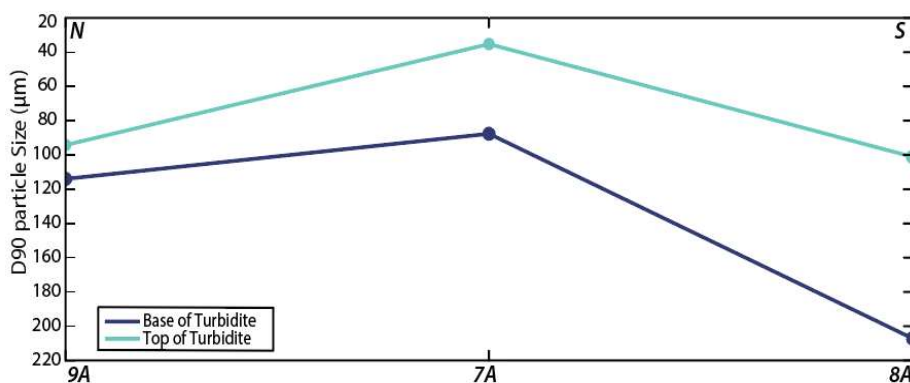


Figure 14. D90 particle size in EL3-A observed in the cores collected along the north-south transect of the southern basin. The standard deviation for D90 particle size at the base and top of the turbidite is 62.8 and 36.2, respectively.

3.2.2 Diatom Analysis

Planktonic diatoms are more abundant than benthic types in all of the samples examined. The samples collected from background sediment exhibit an average P:B ratio of 3.82 ± 0.09 . The P:B ratio in the background sediment was consistent in each of these cores (Appendix C). The assemblages examined from background sediment from cores 7A-1G, 8A-1G, and 10A-1G exhibited P:B ratios of 3.74, 3.80, and 3.92, respectively. Planktonic diatoms observed in the background sediment are abundant and partially to well preserved. Benthic diatoms were generally well preserved.

Assemblages were also examined from various EL1 deposits from the southern basin in cores 8A-1G, 9A-1G, and 12A-1G. The average P:B in the event layers was 2.9 ± 0.05 . EL3-A exhibited a P:B ratio of 2.6 ± 0.08 in cores 5A-1G, 7A-1G, 8A-1G, 9A-1G, and 10A-1G. Diatoms were common or abundant and partially preserved or occasionally fragmented in EL3-A. EL3-A was rich in diatoms throughout the layer across all cores sampled (Fig. 15). The diatom assemblages at the base of EL3-A in these cores contains 71.8% planktonic taxa, while the diatom assemblages from the top of EL3-A contains 75.2% planktonic taxa (Appendix C). Benthic diatoms in the EL3-A deposits across the southern basin are larger and more abundant compared to the background sediment. The base of EL3-A exhibited the lowest P:B but the difference is not statistically significant from the top of EL3-A (Fig. 15). The lower P:B indicates benthic diatoms are more abundant in EL3-A, compared to the background sediment (Fig. 11).

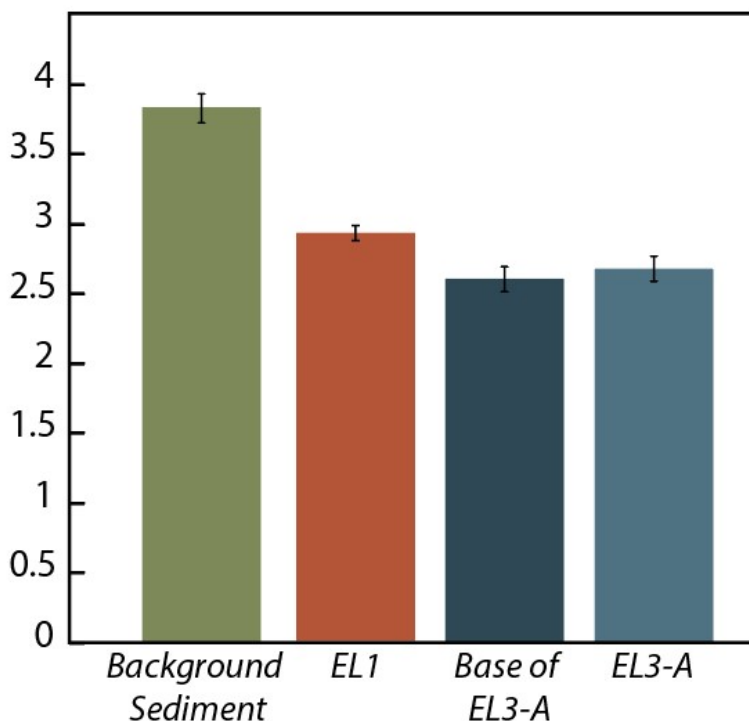


Figure 15. Comparison of P:B in samples from background sediment, EL1s, EL3-A, and the base of EL3-A, in cores 10A-1G, 9A-1G, 8A-1G, 7A-1G, and 5A-1G. The P:B ratio in background sediment is 1.1 greater than the P:B ratio determined in EL3-A deposits.

The ratio of P:B in EL3-A varies in cores across the southern basin (Appendix C). The ratio of P:B in EL3-A was highest in core 7A-1G and 8A-1G (Fig. 16). In contrast,

10A-1G exhibited the lowest average P:B ratio at 2.5 ± 0.05 . Diatom assemblages were also examined from samples collected at the sediment-water interface from cores 12A-1G and 8A-1G, however diatoms were sparser in these samples than deeper in the cores. As a result, only a total of 200 diatoms were identified rather than 400 as were counted in the other samples (Appendix C). These surficial samples exhibited the highest percent of planktonic taxa at 93.2% compared to the other types of samples examined.

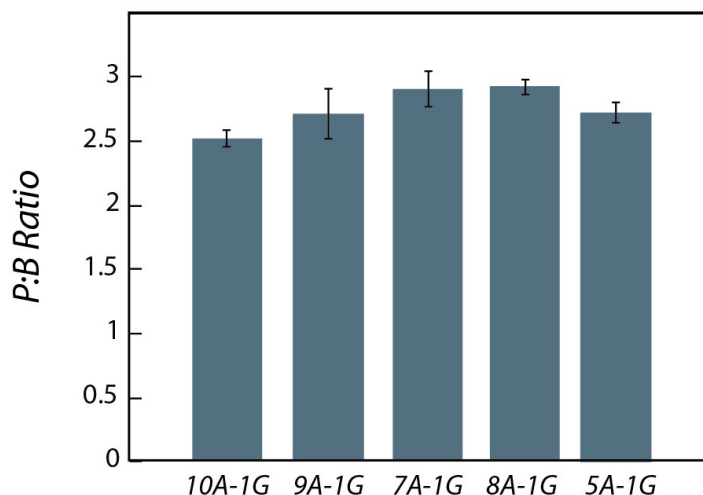


Figure 16. Comparison of P:B ratio in EL3-A across the southern basin. See Appendix C for section depths of samples and ratio of P:B taxa.

3.2.3 Sand Petrology

The sand petrology of the base of EL3-A in cores along the west-east transect in the southern basin was examined by point counting of volcanic-lithic and sedimentary-lithic rock fragments in thin sections (Appendix B). The base of EL3-A in 8A-1G exhibited the greatest contribution of sedimentary clasts at 48% (Fig. 17). In core 7A-1G, the sedimentary contribution at the base of EL3-A was only 37%. The percent of sedimentary clasts decreased from 8A-1G to 7A-1G along the north-south transect across the southern basin (Fig. 18). Along the east-west transect, the base of EL3-A in 5A-1G has the highest contribution of volcanic clasts at 91%. Percent sedimentary-lithic clasts is greatest towards the middle of the southern basin, and then decreases at the expense of volcanic-lithic clasts in the west. (Fig. 17). In addition to sedimentary and volcanic lithic fragments, quartz, alkali feldspar, mica, pyroxene and chert were identified.

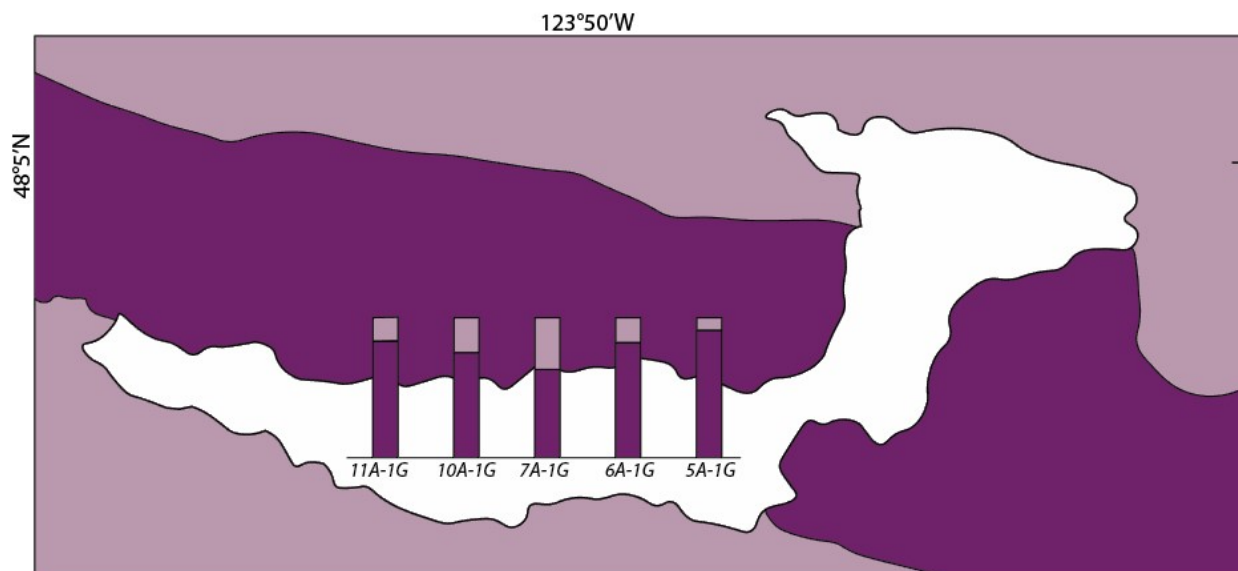


Figure 17. Comparison of volcanic-lithic (dark purple) and sedimentary-lithic (light purple) content of EL3-A samples along the west-east transect overlaid on a simplified geologic map of Lake Crescent. The dark purple on the geologic map represents the Crescent Formation basalt and the light purple represents marine sedimentary rocks from the Adwell Formation and Blue Mountain Unit.

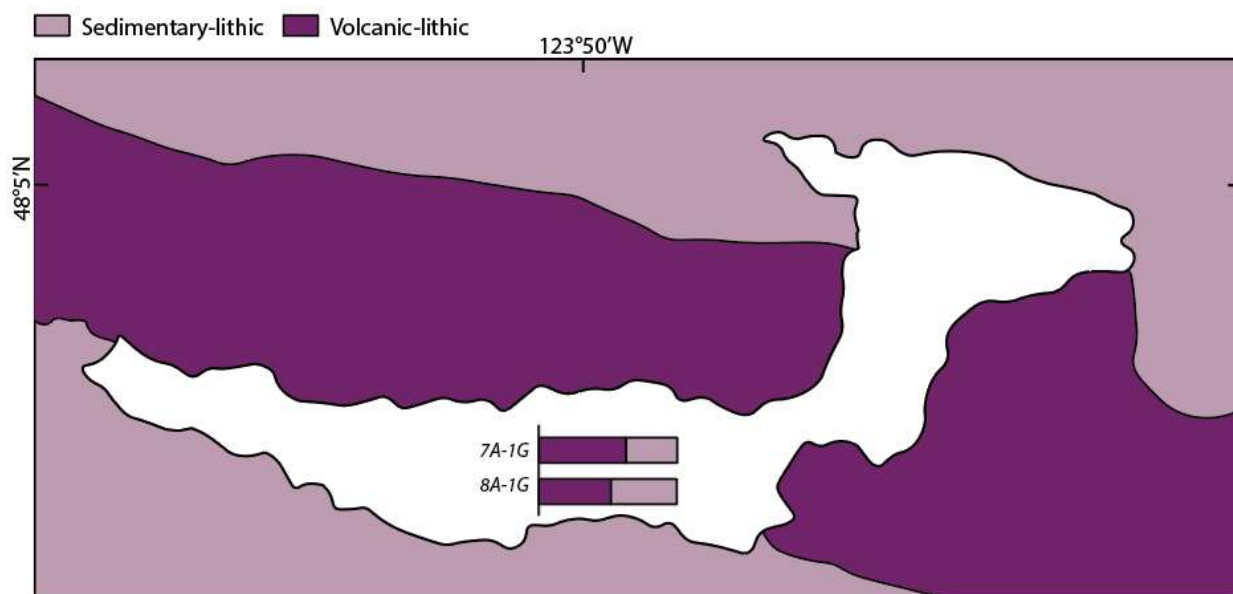


Figure 18. Comparison of volcanic-lithic (dark purple) and sedimentary-lithic (light purple) content from EL3-A deposits along the north-south transect.

3.2.4 X-Ray Fluorescence

XRF scanning was performed on samples from EL3-A in cores collected along the north-south transect in the southern basin (7A-1G, 8A-1G and 9A-1G). The number of samples from EL3-A in cores 8A-1G and 9A-1G is limited, thus the EL3-A from core

7A-1G offers a more detailed perspective on vertical geochemical variations within the layer. EL3-A in core 7A-1G exhibited an upward increase in Fe/Ti. The ratio of Si/Ti varied slightly but exhibited a sharp increase halfway through EL3-A in core 7A-1G (Fig. 19). At the top of EL3-A, there is an abrupt increase in Ca/Al and Ca/Ti. Al and Ti vary throughout EL3-A in all cores (Appendix F).

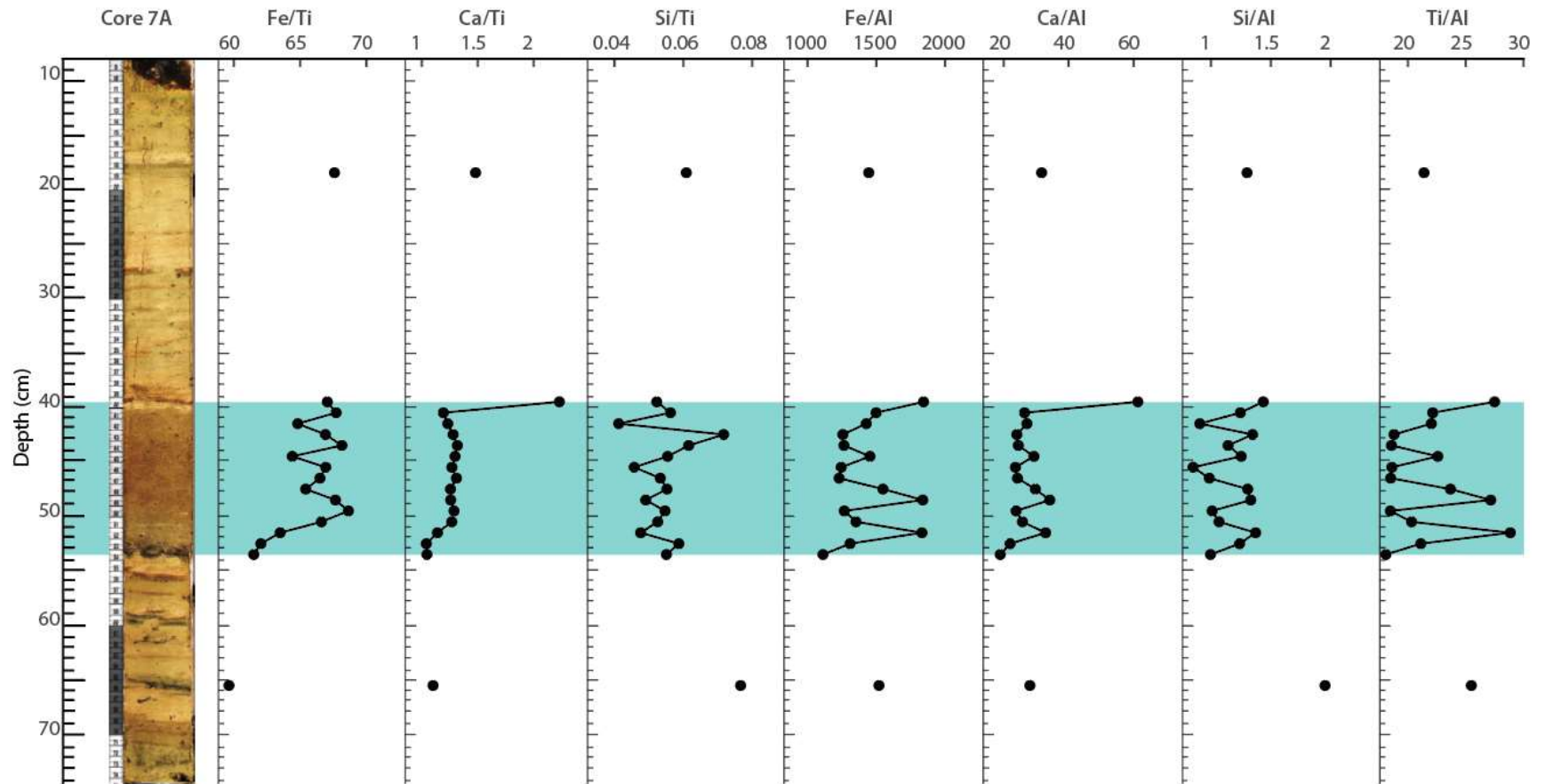


Figure 19. Elemental ratios collected using x-ray fluorescence core scanning in core 7A-1G from the 2018 suite of gravity cores. The light green box represents EL3-A.

The piston cores collected during the 2015 expedition (Pollen, 2016; Joyner, 2016; Leithold et al., 2019) were scanned using XRF at the Large Lakes Observatory in Duluth. The geochemical data from the 2018 gravity cores were used in conjunction with the geochemical data from the core segments SHAKE15-6A-1K-1, 6A-1K-2, 6A-1K-3, and 6A-1K-4 (herein named 6A-1K). Four principal component analyses were performed on the chemical data collected from both the 2018 gravity cores and the data previously collected from piston core 6A-1K. The goal of the principal component analysis (PCA) was to determine statistical parameters that may differentiate various types of event layers from background sediment. The first PCA (*PCA-a*) was run on all data using 20 elements. The 20 selected elements chosen include As, Al, Br, Ca, Cl, Cu, Fe, K, Mg, Mn, Ni, P, Rb, Si, Sr, Ti, V, Y, Zn, and Zr. The second analysis (*PCA-b*) was run on the same samples from the previous model using 10 elements. The 10 elements selected for *PCA-b*, *PCA-c*, and *PCA-d* include Al, Ca, Fe, K, Mg, Mn, Si, Ti, Zn, and Zr. The selection of elements is based on elemental composition of minerals that are commonly associated with the surrounding geology and the loadings from *PCA-a* (Babcock et al., 1992). Si, Ca, Al, Zr, and K are common in marine sedimentary rocks in the Blue Mountain Unit, which include sandstones, mudstones, and conglomerates. In contrast, The Crescent Formation is composed of submarine basalt, characterized by calcic plagioclase, pyroxene, and minor amounts of iron oxides (Glassley, 1974). A third model (*PCA-c*) was run only on chemical data collected from 6A-1G, 7A-1G, 8A-1G and 9A-1G using 10 elements to minimize effects of textural differences and compaction in 6A-1K. The goal of *PCA-c* was to determine the dominant elements in EL3-A, and to determine if there are statistical differences in composition across the basin. Subsequently, *PCA-d* was informed on only the 6A-1K chemical data and the same 10 elements used in *PCA-b* and *PCA-c*.

The loadings for each principal component (PC) emphasize their importance in determining compounded variables, PC1 and PC2, in each model. High loadings have greater importance in each PC. PC1s from each analysis explain the greatest amount of variance. The loadings for the elements with the principal component are presented in Figure 20 for each model. The amount of variance explained increased with the

decreased number of variables used to inform each model. The amount of variance explained is further increased by limiting the number of samples included in the model.

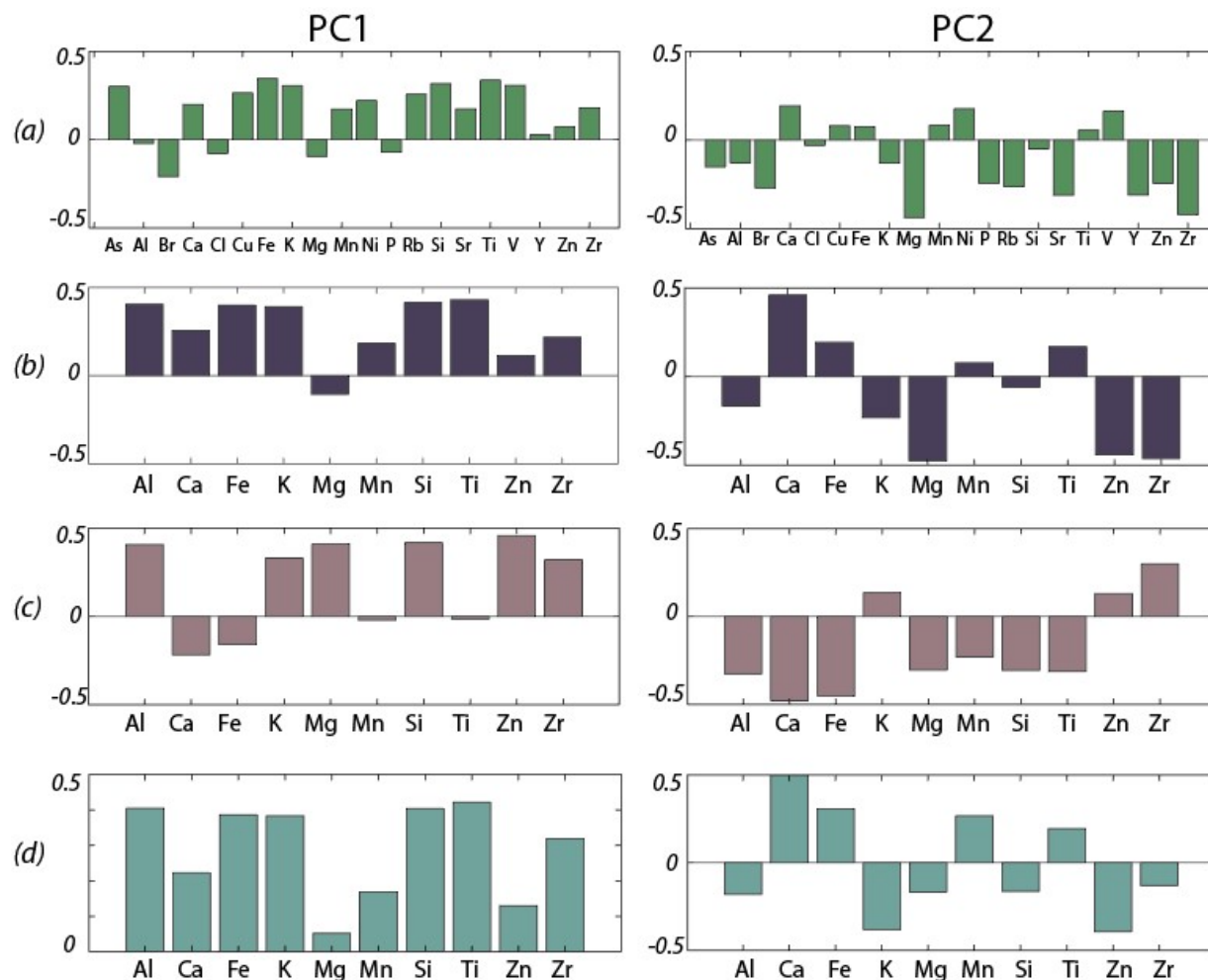


Figure 20. Loadings of elements for principal components (PC1 and PC2, respectively) for four different principal component analyses of chemical data. *PCA(a)* was performed using 20 elements for XRF core scanning from SHAKE18 cores (7A-1G, 8A-1G, and 9A-1G) and SHAKE15 core 6A-1K (sections 1-4). *PCA(b)* was performed on the same cores using only 10 elements from the previous run. *PCA(c)* was performed using the same 10 elements but only on samples from the previously listed SHAKE18 cores. *PCA(d)* was performed on chemical data from SHAKE15 6A-1K (sections 1-4).

Most notably, PC1 from *PCA-c* highlights the contribution of Al, K, Mg, Si, Zn and Zr in maximizing variance between chemical data from 6A-1G and 9A-1G (Fig. 21). *PCA-c* revealed differences in composition in EL3-A along the north-south transect of the southern basin. In the same model, PC2 strongly considers Al, Ca, Fe, Mg, Mn, Si, and Ti. The first PC1 from the model *PCA-c*, is strongly related to elements often associated with clay minerals or sedimentary rocks, including Al, K, Mg, Si, Zn, and Zr.

PC1 explains 34.84% of the variance. The second PC2 from *PCA-c*, also weighs Ca, Fe, and Ti but the variance explained is only 28.58%. The amount of variance is better explained in *PCA-d*. PC1 explains 48.72% and PC2 explains 14.15% of the variance.

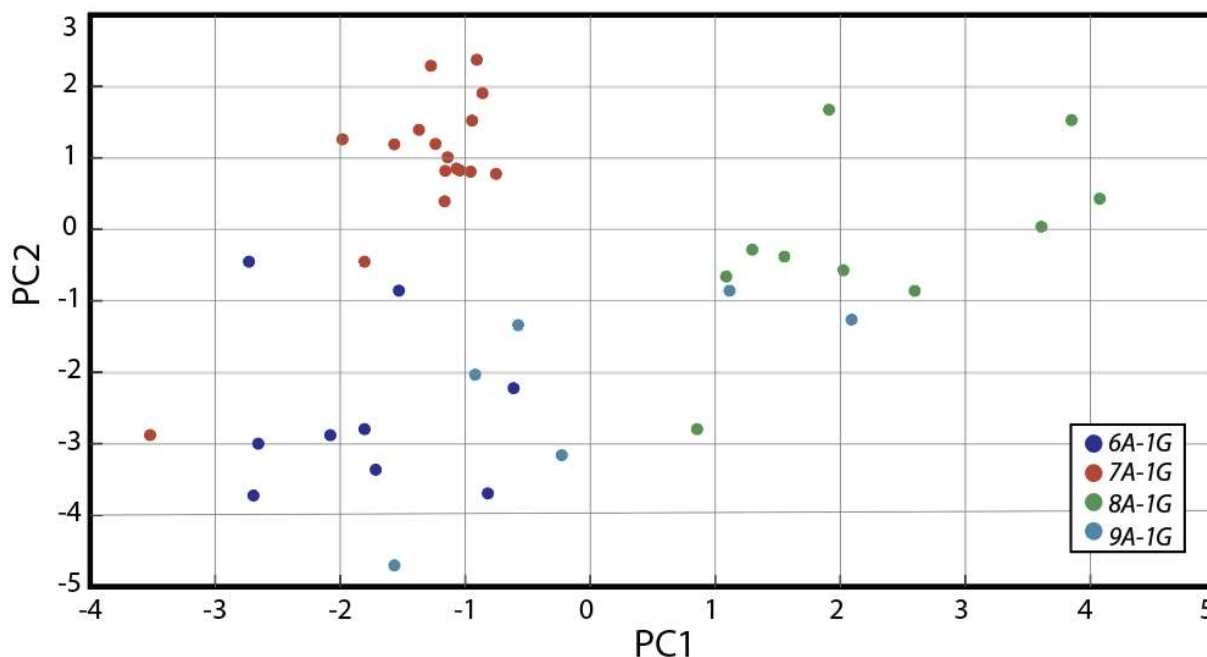


Figure 21. *PCA(c)* model including scores. PC1 explains 33.84% variance PC2 explains 27.4% variance.

3.2.5 Loss on Ignition

The loss on ignition (LOI) analysis performed on EL3-A samples from cores 7A-1G, 8A-1G, and 9A-1G are used to approximate trends in percent organic carbon. In samples from 8A-1G, the percent LOI generally increased from the base to the top of EL3-A. Percent LOI increased upwards in EL3-A in core 8A-1G. The percent LOI from within EL3-A in 7A-1G is variable with depth. The %LOI in EL3-A is characterized by high percent LOI at the base of the deposit, followed by a gradual up-core decrease (Fig. 24). The average percent LOI in EL3-A from 7A-1G is 0.58%. Of the samples measured in 9A-1G, the upper surface of EL3-A (34.5-35.5 cm) shows the highest %LOI from samples measured. The average percent LOI in EL3-A from 9A-1G $0.43 \pm 0.02\%$.

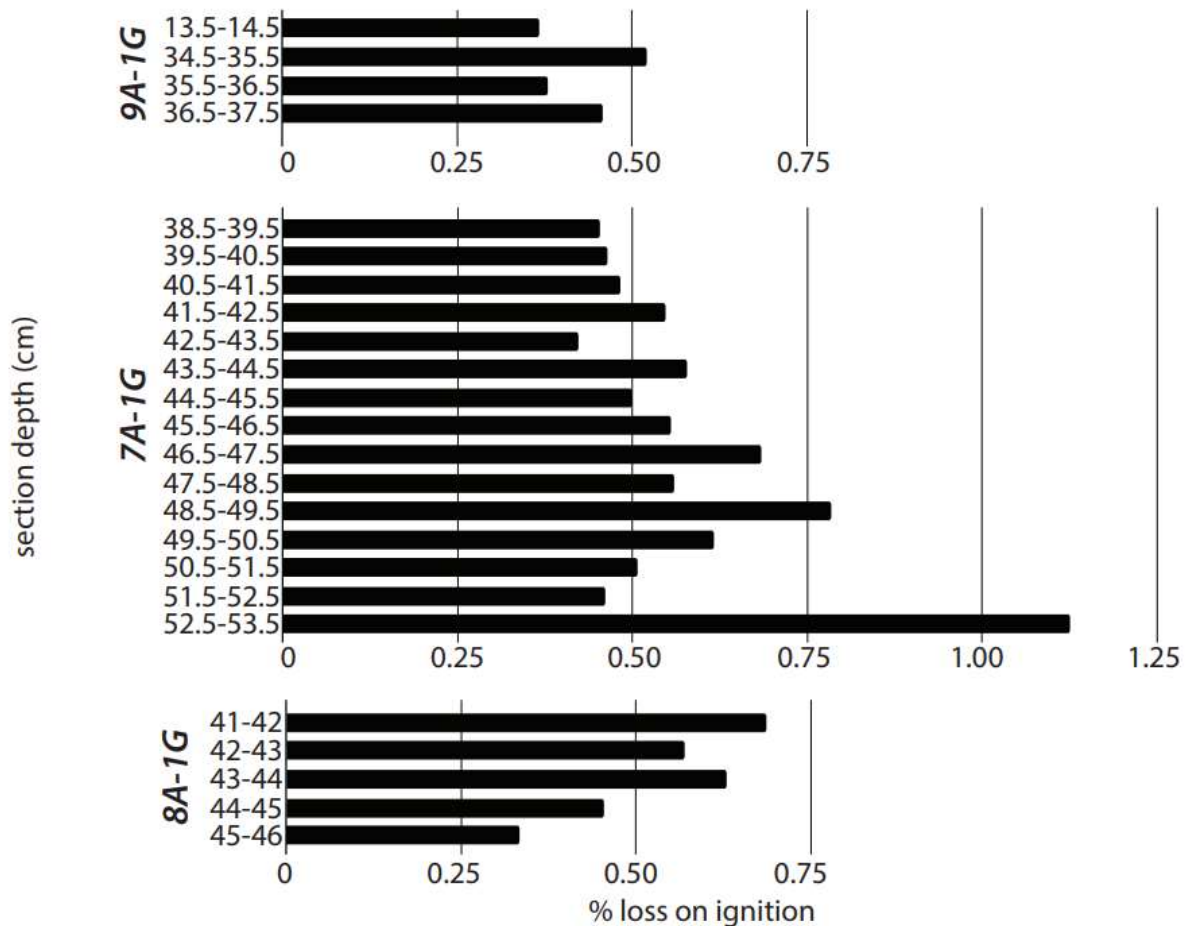


Figure 22. Percent loss on ignition from samples in EL3-A along the north-south transect. Sample 9A-1G-13.5 represents background sediment.

3.3 Age Constraints and Event Free Depth

Calibrated radiocarbon ages are used to constrain the age of EL3-A in cores 10A-1G and 7A-1G, where EL3-A is thickest (Table 3). Calibrated radiocarbon dates from rootlets and leaf fragments provided ages that agree with the event-free age depth model based on previously collected ^{14}C data from Moran et al (2013). Two samples were taken from below EL3-A in cores 7A-1G and 10A-1G and produced calibrated radiocarbon ages that pre-date the 1700 Cascadia event (Fig. 23). In core 10A-1G, the calibrated age range below EL3-A is 451-504 cal yr BP. The sample retrieved from above EL3-A in 10A-1G produced a calibrated date of 64-118 cal yr BP. Two samples were taken from within the EL3-A in core 7A-1G and produced calibrated radiocarbon ages much older than the sample from below event layer in cores 7A-1G and 10A-1G (Table 3). The radiocarbon dates were insufficient to determine age models for cores

10A-1G and 7A-1G. Age-depth 10A-1G was adjusted for compaction but resulted in negligible difference in the upper 0.8 m of sediment.

Table 3. Summary of radiocarbon dating of materials collected above, within, and below turbidite 1. Dates reported in cal BP refer to present as 1950.

Core	Section Depth (cm)	Position Relative to EL3-A	Radiocarbon Age BP (1 sigma)	Calibrated 2 σ age range (cal. BP)	Material Dated
7A	43.0-44.0	Within	500 +/-15	512-538	Rootlets/ wood debris
7A	52.5-53.5	Within	430 +/-20	475-518	Wood debris, leaf fragments, rootlets
7A	61.0-61.0	Below	380 +/-15	435-501	Twig
10A	30.5-31.5	Above	135 +/-15	64-118	Fir needles
10A	60.5-61.5	Below	390 +/-15	451-504	Rootlets

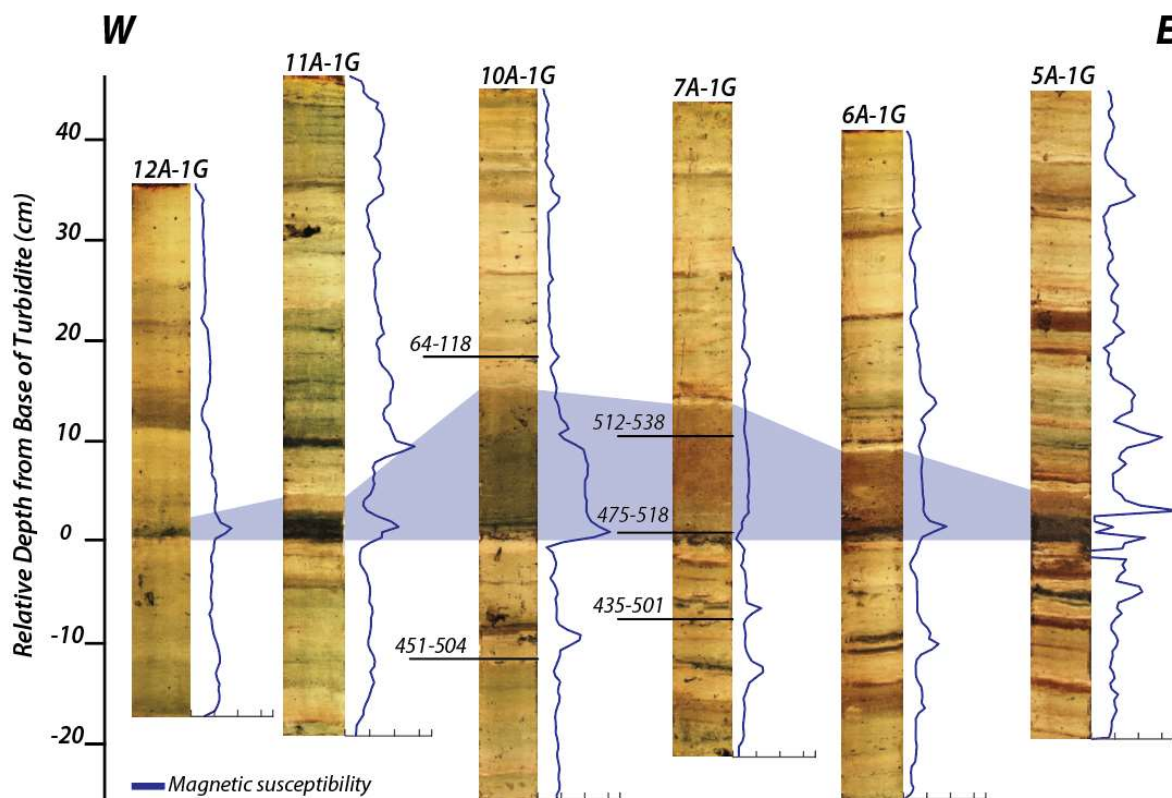


Figure 23. Correlation of EL3-A in cores 12-1G, 11A-1G, 10A-1G, 7A-1G, 6A-1G, and 5A-1G along the west-east transect. Cores are hung on the basal contact of EL3-A. Magnetic susceptibility is shown by the dark purple lines, ranging from 0-650 SI units in each core. Calibrated radiocarbon age ranges are shown at depth in cal yr BP.

Event layers disrupt the background sedimentation by rapidly depositing a larger volume of sediment in a brief period of time, thus the presence of event layers must be considered when determining age at depth. The total thickness of event layers was calculated for each core to determine the event-free depth (Table 4). EL3-A was consistently the thickest event layer that could be identified in cores, ranging from 4 to 15 cm in thickness. Based on radiocarbon dating, the average event-free sediment accumulation rate for the Kasten cores collected by Moran et al. (2013) is 0.79 mm/yr. The sediment accumulation rates derived from the Moran et al. (2013) core LS04 was used to interpolate the age-depth relationship in core 10A-1G (Fig. 24).

Table 4. Event free length and percentage of core that is composed of event layers determined for each gravity core.

Core ID	Total Length (cm)	Event Free length (cm)	% Core composed of ELs	Number of ELs
1A-1G	43.5	35	19.54	6
2A-1G	39	32.5	16.67	5
3A-1G	50.5	43.5	13.86	7
4A-1G	59	52.5	11.76	6
5A-1G	61.5	41.3	32.85	19
6A-1G	62.5	47	24.64	10
7A-1G	73	52.2	28.49	10
8A-1G	50	39.9	20.2	11
9A-1G	69.5	61.6	11.37	7
10A-1G	70.5	54.2	23.12	7
11A-1G	61.5	53.8	12.52	11
12A-1G	49.5	44.8	9.49	3
13A-1G	44	27.5	37.5	11

Based on the application of steady background sediment accumulation rates from Moran et al. (2013), the approximate age of EL1-A is 1946-1953 AD. EL1-B and EL1-C were deposited around 1938-1946 and 1858-1874, respectively (Fig. 24). EL3-A dates from approximately 1715-1747 AD.

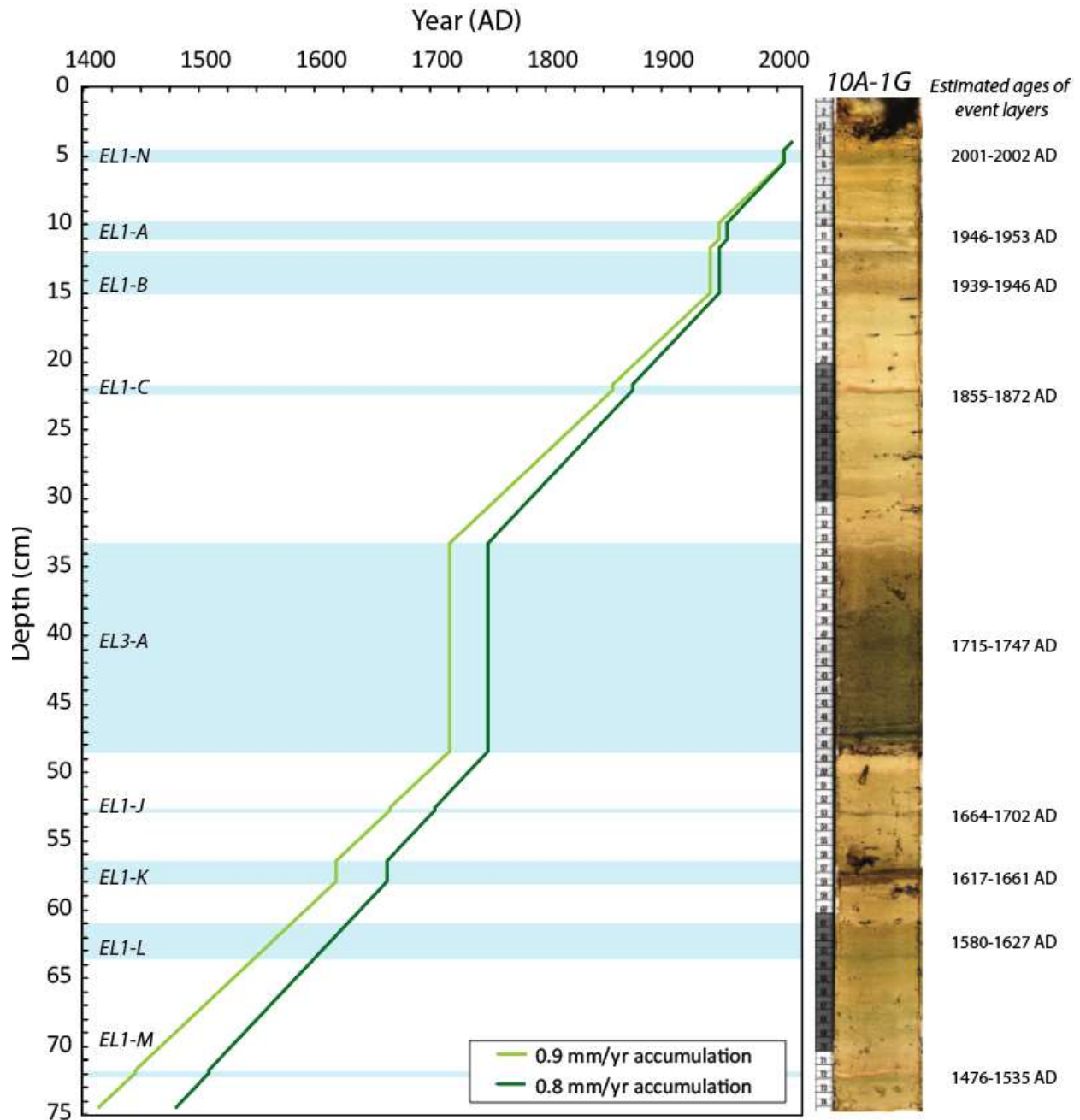


Figure 24. Core image of 10A-1G alongside event-free age constructed using an accumulation rate determined by Moran et al. (2013) and Pollen (2016). The age-depth model is adjusted for presence of identified event layers. The dark green line indicates age at depth determined using an accumulation rate of 0.8 mm/yr. The light green line indicates age at depth determined using 0.9 mm/yr. Light blue intervals indicate event layers. The upper 4 cm of the core photo is Zorbitrol. Approximately 0.5-1 cm of sediment at the surface appears disturbed.

4. DISCUSSION AND INTERPRETATION

4.1 Interpretation of Event Layers

Characterization of event layers in the sediment record may allow for the differentiation of mechanisms involved in their formation, and thus permitting speculation on their origins. During flood events, tributaries may be able to contribute a sufficient sediment load to form a hypopycnal or hyperpycnal plume, depending on the density of the material being transported into the lake. In both scenarios, sediment and plant material from contributing streams travels across the lake as a plume and eventually settles out of the water column, resulting in a fining upward grain size trend (Gilli et al., 2013). These deposits are often dominated by terrestrial plant detritus. Terrestrial plant material can also accumulate on deltas or alluvial fans. During seismic or flood events, increased sediment loading or shaking can remobilize the plant debris. Turbidites may form through a variety of mechanisms including remobilization of lacustrine sediments from the lake margins or deltas. Earthquake-induced slope failures can trigger turbidity currents that transport sediment across the basin floor.

To better understand the origin of the sediment incorporated in the event layers, the relative abundance of diatoms was examined in background sediments and event layers. It is expected that sediment that has been remobilized from within the lake basin will exhibit a relatively higher abundance of diatoms compared to sediment derived from fluvial inputs. The abundance of diatoms in EL1 and EL3 layers argues against the sediment originating directly from fluvial inputs. The diatom abundance in EL2 layers was low and did not allow for a statistically significant count, which may indicate that the plant debris was derived directly from Barnes Creek. Based on the relative abundance of diatoms in EL1 deposits and EL3, it is concluded that these deposits formed from the disturbance, suspension, and redeposition of sediment from within the lake basin.

The variations in thickness, mineralogy, and grain size in the EL1 deposits reflect the variety of potential sources and events responsible for depositing that sediment. Numerous EL1 deposits can be correlated across multiple cores in the southern basin, while others only appear in cores close to the shoreline. Given the widespread occurrence of EL1 deposits in cores across the basin, EL1 deposits are conceivably

deposited on the lake bottom via turbidity currents that originated from small subaqueous slope failures. However, it remains unclear if all EL1 layers resulted from slope failures triggered by earthquake-induced shaking. It is important to note that several EL1 deposits can only be correlated between a few cores and the greatest number of EL1 deposits appear in cores closer to Barnes Creek delta. Given the limited spatial extent of these thin turbidite layers, it is unlikely they originated from a basin-wide trigger, such as an earthquake.

In contrast, EL1-A, EL1-B, and EL1-C can be correlated in all cores recovered from the southern basin suggesting they may represent more widespread sediment remobilization in the lake. Based on the age determined using the event-free sediment accumulation rates, EL1-A may have been deposited as a result of ground shaking from the 1949 Olympia earthquake. EL1-B was deposited around 1938-1946, overlapping in time with the 1946 Vancouver Island earthquake. EL1-C was likely deposited between 1858 and 1874, overlapping the 1872 Entiat earthquake. Finally, EL1-N only appears in core 10A-1G however, it may not appear in additional cores due to disruption of the sediment-water interface, and it may record the 2001 Nisqually earthquake.

Daily discharge data from the Elwha River stream gauge were examined for evidence of extreme flooding events that may coincide with the estimated ages of EL1-A, EL1-B, and EL1-N (Fig. 26). The estimated age of deposition for EL1-C pre-dates the installation of the USGS stream gauge, thus was not compared to the daily discharge data. A daily discharge of 1.6450×10^4 ft³/sec is assigned as the minimum for flooding, just below the current minimum for the minor flood stage. The lack of high discharge in the Elwha River during the previously mentioned time periods suggest flooding events are unlikely triggers of event layers EL1-A, EL1-B, and EL1-N. Rather, based on the coincidence of major earthquakes with their estimated times of deposition, they appear to be seismic in origin.

The relative thickness of each event layer was compared to the Modified Mercalli Intensity reconstructed by the USGS (2016) near Lake Crescent for each of the corresponding earthquakes (Fig. 25). The simulation of the AD 1700 Cascadia subduction earthquake suggests Lake Crescent would experience a shaking intensity of VII. That event is represented as the thickest turbidite deposited in the lake in the last

~450 years of sediment accumulation. Modelled intensity scenarios for the Vancouver Island earthquake (USGS, 2016) indicate the event would result in a shaking intensity of VI at Lake Crescent, and it is hypothesized to have produced a turbidite up to 5 cm thick (Fig. 25). The Nisqually and Olympia earthquakes are reconstructed to have resulted in a shaking intensity of V near Lake Crescent, where they may have each been responsible for 2-cm-thick turbidites. Finally, the thinnest of the turbidites present in multiple cores and correlated with a historical seismic event, the Entiat earthquake, was possibly generated by III intensity shaking at Lake Crescent.

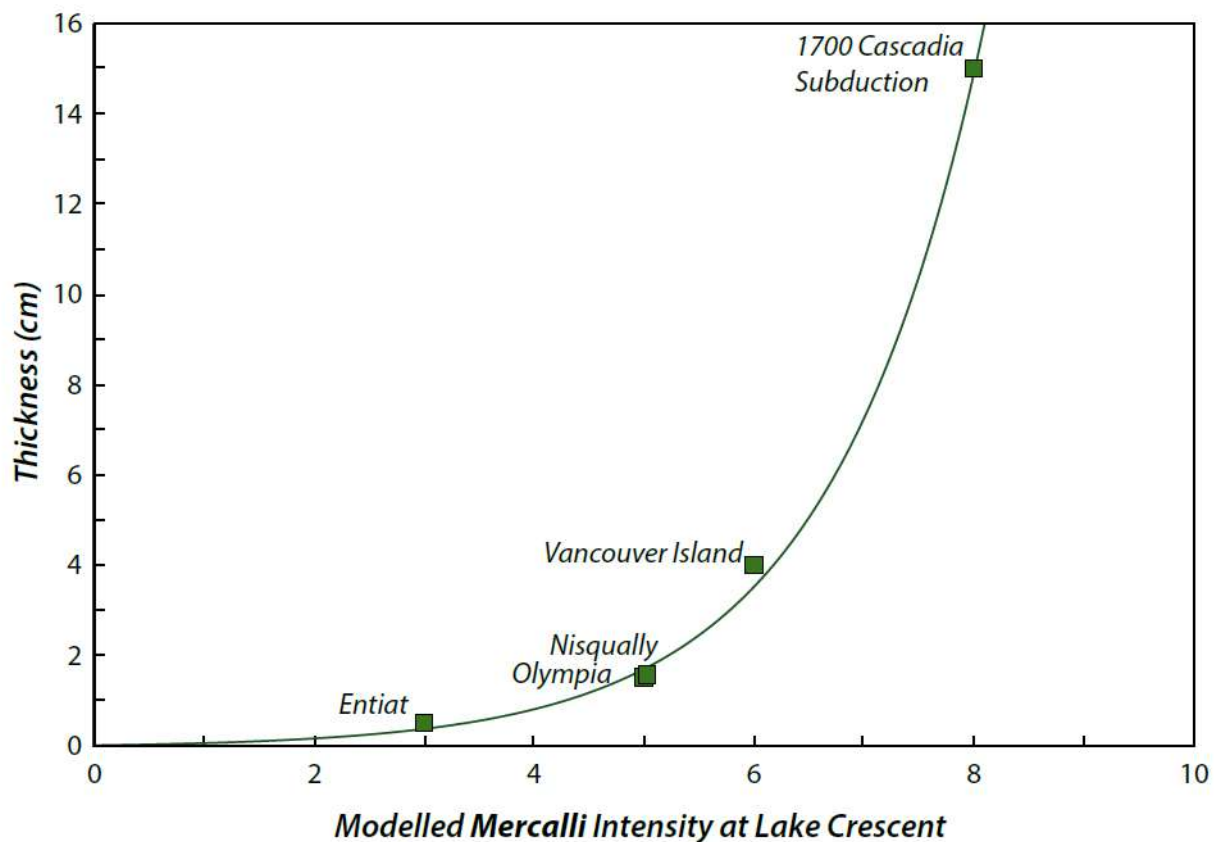


Figure 25. Relationship of the thickness of event layers and modelled intensity of shaking at Lake Crescent during earthquakes hypothesized to have been responsible for their deposition. Event layers include EL1-A, EL1-B, EL1-C, EL1-N, and EL3-A (USGS, 2016).

The event layers classified as EL2 deposits in 13A-1G are interpreted as flood deposits. The abrupt change from a clastic-dominated background facies to one predominantly composed of woody detritus may be the result of a minor slope failure of Barnes Creek delta or plant debris settling out of the water column after a flood. The

limited spatial extent of the EL2 deposits argues against a seismic trigger. It is possible that Barnes Creek delta failed during episodic flood events. Comparison of the Elwha River discharge to the estimated timing of EL2 deposits in 13A-1G favors a flood-induced trigger for their deposition (Fig. 26), during high stream discharge events that occurred in 1956, 1961, 1975, 1980, 1982, 1990, 1996, 1997, 2001, and 2007.

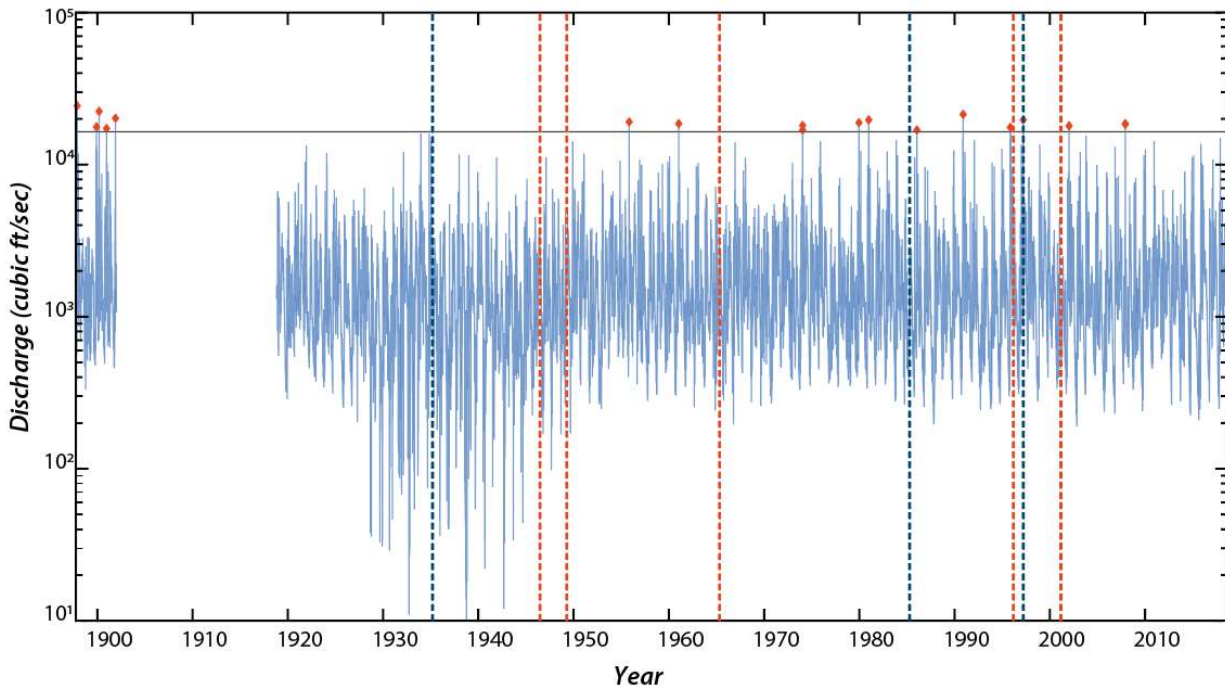


Figure 26. Blue line shows daily discharge data collected from USGS 12045500 Elwha River Stream Gauge Station at McDonald Bridge near Port Angeles, WA. Red diamonds indicate days where discharge exceeded $1.6450 \times 10^4 \text{ ft}^3/\text{sec}$ (1 standard deviation). Red dashed lines indicate dates of the Vancouver Island, Olympia, Tacoma, Nisqually, and Duvall earthquakes, from left to right. Blue dashed lines show approximated timing of EL2 layers found in 13A-1G.

4.2 Interpretation of EL3-A

The presence of EL3-A across the full extent of the sampling transect in the southern basin indicates that a large volume of sediment was mobilized prior to its deposition (Fig 9). Magnetic susceptibility and density profiles corresponding to the EL3-A event layer are highly variable across the southern basin, indicating the broad range in particle size and the material incorporated into EL3-A (Appendix G).

Based on visual examination of cores and particle size analysis, EL3-A is interpreted as a stacked turbidite. Stacked turbidites are sedimentary deposits formed

by near simultaneous turbidity currents, commonly associated with earthquake shaking (Van Daele et al., 2017). They are characterized by multiple distinctive coarse-grained pulses, a shared clay cap and coarsening trends in more than one direction within the lake basin, as would be expected for sediment derived from multiple lake-slope failures (Fig. 12). The grain size structure of EL3-A exhibits two fining upward sequences in cores 6A-1G and 5A-1G. The coarse pulses are indicated by a distinct increase in the magnetic susceptibility and bulk density profiles. In core 7A-1G, however, the coarse fraction of sediment at the base of EL3-A is understated in the magnetic susceptibility profiles and particle size analysis, which may be a result of material having been sampled just below the base of EL3-A or the presence of organic material. Particle size and magnetic susceptibility trends across the basin suggest the event caused at least two separate slope failures. D90 particle size at the base of the turbidite fines away from the delta along the west-east transect, suggesting a delta front failure may have been initiated by earthquake shaking (Fig. 13 and 14). Cores 8A-1G and 9A-1G exhibit a single fining upward sequence. The overturned sediment beneath EL3-A in 8A-1G may be a result of the deposition of EL3-A or interpreted as a slump deposit. Along the north-south transect, D90 particle size at the base of EL3-A fines away from the southern slope, suggesting the southern slope failed nearly synchronously (Fig. 12). The lack of a fine cap between the coarse pulses also supports the conclusion that the pulses occurred near-simultaneously. EL3-A in cores 5A-1G, 6A-1G, 7A-1G, 8A-1G, 9A-1G is overlain by a clay cap, visible in core photos and indicated by the abrupt decrease in magnetic susceptibility and increase in L^* (Fig. 26; Appendix G).

The relative abundance of planktonic and benthic diatoms in EL3-A compared to background sediments also provides information about the processes responsible for its deposition. While both planktonic and benthic diatoms are photosynthetic, benthic diatoms are restricted to the shallow lake margins where sunlight reaches the lake bottom (Rosén et al., 2009), which for Lake Crescent extends to a depth of about 30 m (Hampton et al., 2011). Planktonic taxa can be found in open waters across the lake basin, including at the lake margins. Planktonic diatoms fall through the water column and are abundant in background sediment (Wang et al., 2013). The greater abundance of benthic diatoms in EL3-A compared to background sediment suggests the sediment

incorporated into EL3-A was remobilized from the shallow portion of subaqueous slopes that included depths within the photic zone. This result could also reflect the sorting of diatoms during transport and deposition of the layer, as is similarly reflected in the general fining upward of the EL3-A deposits (Figs. 12 and 27).

Variations in the mineralogy of the sand at the base of EL3-A is also interpreted as an indication of multiple probable sediment sources that contributed to the event layer. The apparent increase in volcanic clasts with proximity to the eastern end of the south basin points to the incorporation into the turbidite of basaltic sediment from either the Barnes Creek delta or the northern slope of the south basin, where Crescent Formation basalts crop out (Figs. 2 and 17). The abundance of sedimentary-lithic grains at the base of EL3-A along the north-south transect in the southern basin suggests that sediment from the southern slope of the south basin, where marine sedimentary rocks crop out (Schasse, 2003), was also incorporated into the turbidite (Fig. 18). Along the west-east transect in the southern basin, volcanic content increases toward the edges of the basin. The highest volcanic-lithic content was observed at the base of EL3-A in cores 12A-1G and 5A-1G. In contrast, the layer in core 8A-1G had the lowest contribution of volcanic sedimentary grains, which was in sharp contrast to the composition of the sand in its northern neighbor, 7A-1G. The increase in sedimentary lithic content towards the southern slope of the south basin affirms the notion that the southern slope failed during this event. More specifically, the southern slope failure was likely limited to the middle of the southern basin, given the lower sedimentary input observed in cores 11A-1G and 6A-1G. Conversely, an additional failure from the western or northwestern slope may have contributed to the higher proportion of volcanic grains. The change in mineral composition at the base of EL3-A across the basin further suggests slope failures occurred near simultaneously. Results from the sand petrology analysis are not considered representative of the entire turbidite with depth; however, they indicate how mineralogy changes across the basin, namely the mineralogy of the initial coarse pulse of sediment. Sorting of grain sizes can influence mineralogy. The upward decrease in L^* in EL3-A may be attributed to the influx of volcanic-lithic and mafic mineral grains, such as pyroxene or illite. The upward increase in a^* throughout EL3-A suggests the presence of iron oxide minerals.

The PCA model (specifically PCA-c) provides a statistical method to understand the contribution of volcanic versus sedimentary clastics to the EL3 layer. Principal component 1(PC1) from this model is strongly loaded by elements associated with clays weathered from sedimentary rocks, including Si, K, and Zn (McLennan, 1993). The sample from EL3-A in core 8A-1G, closest to the southern slope, scored high along PC1, suggesting EL3-A in 8A-1G has a relatively large contribution of these elements. In contrast, principal component 2 (PC2) is strongly influenced by Fe, Ca, and Ti associated with plagioclase feldspar, pyroxene, and iron-titanium oxides such as magnetite. Samples from EL3-A in 7A-1G are clustered toward a higher PC2 score and lower PC1 score, compared to the layer in cores 8A-1G and 9A-1G. This result suggests that the mineralogy throughout EL3-A in 7A-1G is dominated by basaltic sediment. Samples from EL3-A in cores 8A-1G and 9A-1G, in contrast, are distributed along the positive end of PC1, suggesting that the turbidite found at the north and south edges of the basin has a mixed mineralogy.

Finally, percent loss on ignition provides perspective on the distribution of organic carbon in the turbidite along the north-south transect in the basin (e.g., De Vos et al., 2005). The base of 7A-1G appears uneven and the LOI and visual examination indicates the base is overlain by plant material (Fig. 27). Organic material may mask the signal in the magnetic susceptibility at the base of EL3-A in several cores. The turbidite in Core 8A-1G is characterized by an upward increase in %LOI, indicative of an increase in percent organic matter. The distinct increase in 8A-1G is likely a result of the settling of plant material from the southern slope. In contrast, the %LOI observed in 7A-1G is highly variable, lacking any trend with depth (Fig. 15). The average %LOI is greatest in core 8A-1G, indicating a potential source of organic carbon exists near to the southern slope of the south basin. This may suggest that terrestrial plant material derived from the southern margin of the south basin was incorporated into the turbidite during the slope failure, resulting in higher organic carbon content by volume.

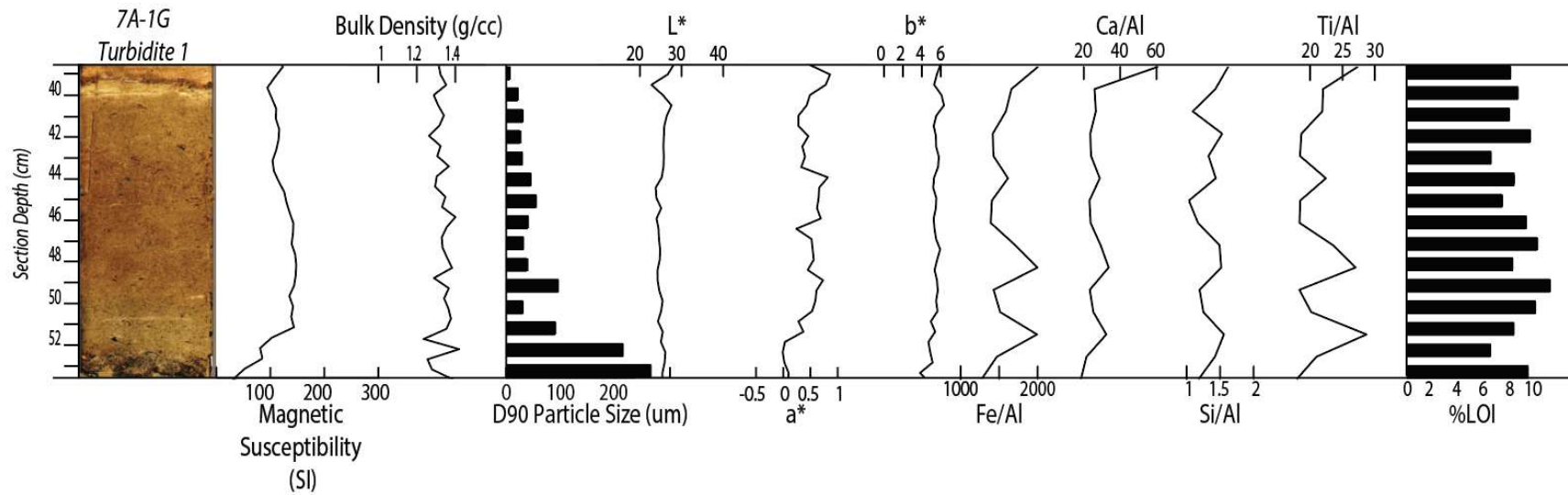


Figure 27. Representative turbidite from core image of 7A-1G alongside profiles of magnetic susceptibility (SI), bulk density (g/cc), D90 particle size, color parameters (L^* , a^* , and b^*), ratios of geochemical data, and percent loss on ignition.

4.2.1 Attribution of EL3-A to the 1700 AD Cascadia Earthquake

Numerous types of geologic evidence suggest the Cascadia subduction zone is capable of producing earthquakes with magnitudes exceeding 8.0-9.0 (Atwater, 1987; Goldfinger et al., 2012). Age constraints for EL3-A in the SHAKE18 suite of gravity cores suggest that this event layer was deposited during the 1700 A.D. Cascadia earthquake. The sediment accumulation rates from Moran et al. (2013) suggest EL3-A was deposited around 1715. This difference in age may be attributed to the error associated with radiocarbon dating or approximation of the “zero-age” at the top of the slightly disturbed surface of core 10A. EL3-A is the largest event layer recorded in the last ~450 years of sedimentation in Lake Crescent, consistent with the regional paleoseismic record that indicates that the AD1700 event was the only great earthquake in this time span. Numerous event layers in the sediment record further suggest that the lake is sensitive to disturbances, alluding to the fact that Lake Crescent should have been affected by intense ground shaking and movement associated with previous subduction earthquakes. Figure 27 serves as an example of the characteristics in grain size D90 profile shape that should be mirrored in turbidites identified deeper in the sediment record of Lake Crescent. EL3-A from core 7A-1G is used as a frame of reference to identify additional event layers deeper in the late Holocene record that exhibit similar profiles. Given its proximity to the 7A-1G coring location and previously documented suite of decimeter-scale turbidites, core 6A-1K from the 2015 suite of Kullenberg cores is examined. Magnetic susceptibility, bulk density, and L^* from the geophysical logs in the decimeter-scale turbidites were examined for similarities shared with EL3-A from core 7A-1G.

4.3 Interpretation of turbidites in SHAKE15

Approximate ages of basin-wide event layers identified as turbidites were taken from a study by Pollen (2016). Identified event layers are indicated in Table 5. Visual comparison of EL3-A to event layers in the SHAKE15-6A-1K reveals similarities in thickness, color, and structure, suggesting there may be shared trigger mechanisms or processes responsible for the deposition of the individual layers (Fig. 27). The 6A-1K core was collected within close proximity to the 7A-1G core.

Eleven unique event layers were identified in the four sections of 6A-1K that resemble the EL3-A deposit, ranging from 6-24 cm in thickness (Table 5). In core section 6A-1K-1, two were identified ranging in thickness from 7-24 cm. Section 6A-1K-2, contained at least five EL3-A-style event layers, ranging from 15-24 cm in thickness. Finally, the third section of 6A-1K contained four event layers that exhibit similar characteristics (Fig. 28). Pollen (2016) determined the approximate age of each of these event layers (Table 4). All of these event layers show sharp basal contacts and sandy lower intervals with high magnetic susceptibility response, overlain by homogenous to normally graded finer sediments. A dark-colored basaltic sand was observed in turbidites that Pollen (2016) labeled SH15-T2, SH15-T5, and SH15-T7 (Fig. 28). It is conceivable that several of the identified turbidites in 6A-1K were deposited as a result of a subduction earthquake. However, it remains unclear if each of the eleven turbidites in 6A-1K formed during a subduction earthquake or another seismogenic trigger was responsible.

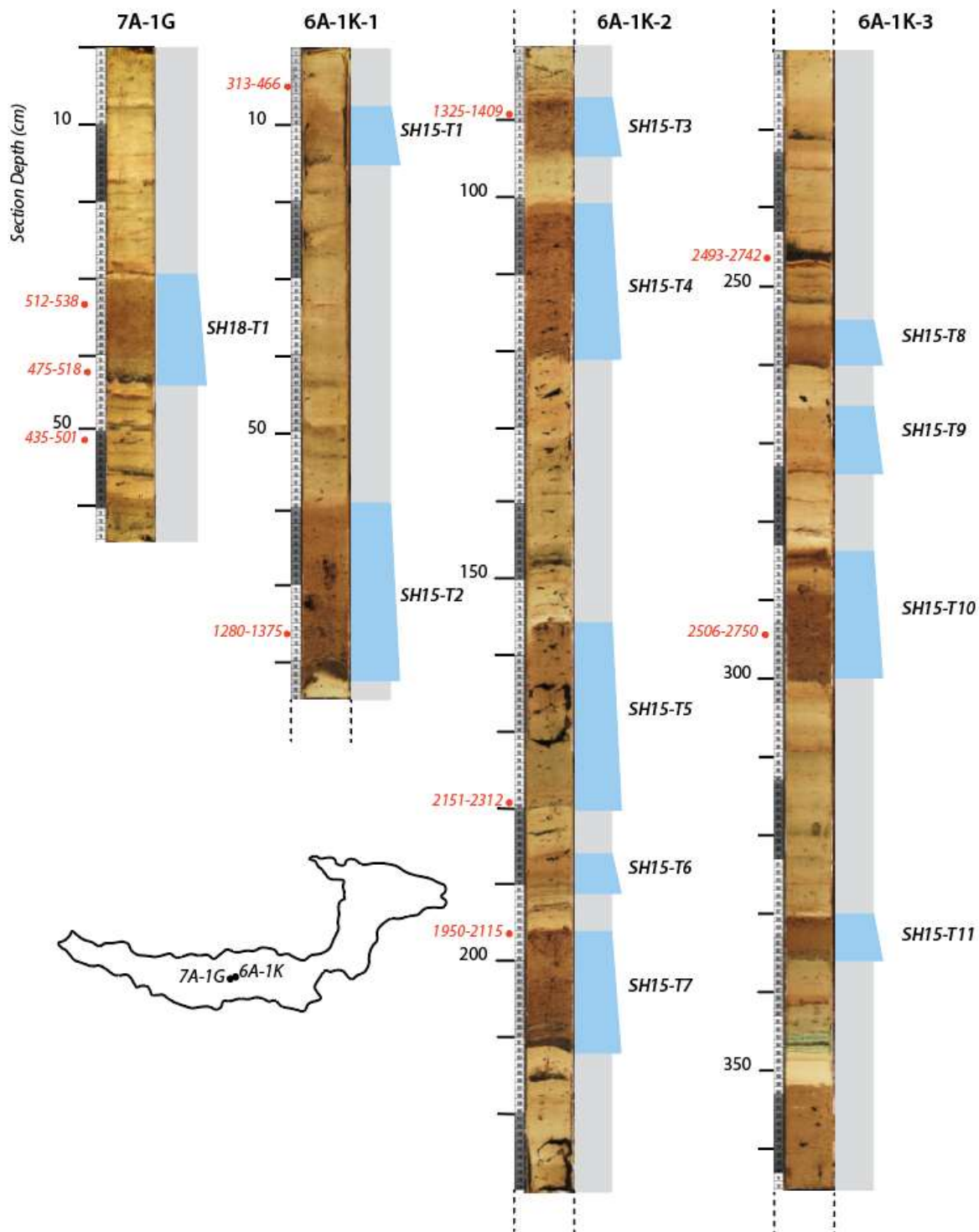


Figure 28. Visual comparison of the EL3-A-style deposits identified in SHAKE2018 with similar layers in the SHAKE2015 cores, indicated by the blue polygons. Eleven turbidite deposits in sections 1, 2, and 3 from core SHAKE15-6A-1K are shown alongside core images and graphic interpretation. The EL3-A deposit in core SHAKE18-7A is correlative to SH15-T1. Calibrated radiocarbon dates (red text) are reported in Leithold et al., 2019.

Notable similarities of proposed event layers in the SHAKE2015 cores to EL3-A include a thickness ≥ 9 cm, a distinct increase in grain size at the base of the turbidite, a black or dark-colored sandy bottom, and incorporation of terrestrial plant debris. The decimeter-scale turbidites described in 6A-1K represent the equivalent of at least 100 years of background sedimentation that was presumably deposited in a matter of hours to days (Pollen, 2016) and are comparable to the thickness of EL3-A identified in the 2018 gravity cores. The substantial thickness of both EL3-A and the SHAKE15 turbidites suggest a basin wide trigger mechanism that is able to overcome lake-slope stability is responsible for the deposition of the previously mentioned layers. EL3-A layers exhibit a fining upward grain structure or appear massive throughout, which is also observed in the grain size structure of turbidites in the 6A-1K (Pollen, 2016). The upper part of SHAKE15 turbidites can be massive to normally graded silty sediment. In 2018 gravity cores 10A-1G, 7A-1G, 6A-1G, and 5A-1G, EL3-A has a thick, dark-colored, multi-pulsed, sandy base, ranging from 1-3 cm in thickness, also observed in SH15-T7 and SH15-T8. Variations in chemical profiles and color indicate that sediment from multiple sources is incorporated into the SHAKE15 turbidites, however additional mineralogical data is required to determine the origin of the sedimentary components. The sand petrology and grain size analyses of EL3-A also indicated that sediment was incorporated from multiple sources within the lake basin. Terrestrial plant material and woody debris appear in several of the turbidites from 6A-1K. Several of the identified SHAKE15 turbidites in 6A-1K deposits are capped by finely laminated clay (Pollen, 2016; Fig. 28).

Table 5. Summary of EL3-A-style deposits identified in core 6A-1K (sections 1-3). Ages were obtained from radiocarbon dating and extrapolation using an age model developed previously for Lake Crescent by Pollen (2016) and Leithold et al. (2019). Calibrated ages indicated with an asterisk were obtained through radiocarbon dating. Ages in the parentheses were extrapolated from the sediment depth-age model (Pollen, 2016).

Event Layer ID	Core ID	Section Depth in Core 6A (cm)	6A-1K Age (BP)	Event Layer Thickness (cm)	Presence in SHAKE15 cores
SH15-EL3-A	6A-1K-1	8	854 (796-925)*	7	South Basin
SH15-T2	6A-1K-1	60	1318 (1280-1375)*	24	South Basin
SH15-T3	6A-1K-2	7	(1325-1409)*	8	North/ South Basin
SH15-T4	6A-1K-2	21	1468 (1393-1526)*	20	North/ South Basin
SH15-T5	6A-1K-2	76	1682** (2151-2312)*	24	North/ South Basin
SH15-T6	6A-1K-2	106	NA	6	North/ South Basin
SH15-T7	6A-1K-3	116	2028 (1950-2115)*	15.5	North/ South Basin
SH15-T8	6A-1K-3	33	2528 (2436-2660)	8	North/ South Basin
SH15-T9	6A-1K-3	52.5	NA	8.5	South Basin
SH15-T10	6A-1K-3	69.5	2722 (2506-2750)	11	North/ South Basin
SH15-T11	6A-1K-3	117	NA	6	South Basin

The presence of multiple EL3-A-style deposits deeper in the sediment record denote the strong possibility that similar event layers occur regularly throughout the sediment record of Lake Crescent, and likely resulted from seismic events rather than floods. Due to the physical and chemical similarities to EL3-A, the previously mentioned

event layers are inferred to be seismically-triggered deposits. However, the source of the earthquake for each identified layer cannot be distinguished based on this information alone.

5. CONCLUSIONS

5.1 Summary

Radiocarbon data and accumulation rates strongly suggest that the EL3-A event deposit found in Lake Crescent gravity cores formed as a result of multiple slope failures around 1700 AD during the great earthquake triggered by rupture of the Cascadia subduction zone. EL3-A is the most prominent event layer, in terms of thickness and spatial extent, identified in the most recent ~500 years of the late Holocene sediment record of Lake Crescent. Based on the interpretations of lateral changes in particle size, sand petrology, and diatom analysis, ground shaking from the M_w 9 earthquake likely caused the Barnes Creek delta front and southern lake margin slopes to fail nearly simultaneously, remobilizing large volumes of sediment down into the deep southern basin. The presence of similar turbidites deeper in the sediment record suggests that numerous large earthquakes have affected the lake in the last ~3,000 years of sedimentation, some likely subduction earthquakes. Identification of a stacked turbidite related to the Cascadia subduction earthquake provides a fingerprint to interpret the recurrence interval for intense earthquake shaking at Lake Crescent.

The late Holocene sedimentary record of Lake Crescent preserved at least 15 unique event layers that can be correlated across the southern lake basin. Three EL1 deposits, inferred to be minor turbidites, can be correlated with historical earthquakes triggered at some distance from the lake by crustal faults or deep in the subducting slab based on the accumulation rates from Moran et al. (2013) and Pollen (2016). The daily discharge data from the nearby Elwha River suggests that the EL1 deposits identified in the last 100 years of sedimentation are inconsistent with the timing of flood events; however, organic-rich EL2 deposits preserved primarily in the delta-proximal core 13A-1G may be the result of enhanced stream discharge into Lake Crescent. Identification of turbidites deeper in the sediment record (e.g., from SHAKE15 piston cores) that present similar characteristics to the event layers identified here support the presence of seismically-induced event deposits in Lake Crescent. The abundance of distinct event

layers suggest that Lake Crescent is a sensitive archive of seismic events, and may allow for the distinction of subduction zone and regional crustal earthquake events, including those occurring in upper-plate (Vancouver Island, 1946 (M_w 7.0 – 7.5) and Entiat 1872 (M_w 6.5 – 7.0) and intra-plate settings (1949 Olympia (M_w 6.7) and 2001 Nisqually (6.8 M_w)).

REFERENCES

1. Atwater BF. (1987) Evidence for great Holocene earthquakes along the outer coast of Washington state. *Science* v. 236, p. 942-944.
2. Atwater, B.F., Hemphill-Haley, E. (1997) Recurrence intervals for great earthquakes of the past 3,500 years at northeastern Willapa Bay, Washington. U.S. Geological Survey Professional Paper 1576, p. 81-103.
3. Atwater, B. F., Moore, A. L. (1992) A Tsunami about 1000 Years Ago in Puget Sound, Washington. *Science* 258: p. 614-7.
4. Atwater, B.F., Musumi-Rokkaku, S., Satake, K., Tsuji, Y., Ueda, K., and Yamaguchi, D.K. (2016) The orphan tsunami of 1700: Japanese clues to a parent earthquake in North America: University of Washington Press.
5. Babcock, R. S., Burmester, R. F., Engebretson, D. C., Warnock, A., & Clark, K. P. (1992) A rifted margin origin for the Crescent Basalts and related rocks in the northern Coast Range volcanic province, Washington and British Columbia. *Journal of Geophysical Research*, v. 97(B5), p. 6799–6821.
6. Bodle, R.R. and Murphy, L.M. 1948, U.S. Department of Commerce, Coast and Geodetic Survey, Serial Number 714, U.S. Government Printing Office, p. 17-22.
https://assets.pnsn.org/HIST_CAT/1946.html [March 18, 2019]
7. Bragée, P., Mazier, F., Rosén, P., Fredh, D., Broström, A., Granéli, W., and Hammarlund, D. (2013) Forcing mechanisms behind variations in total organic carbon (TOC) concentration of lake waters during the past eight centuries and palaeolimnological evidence from southern Sweden. *Biogeosciences Discussions*, v. 10, p. 19969–20003.

8. Clague, J. J. (2002) The earthquake threat in southwestern British Columbia: A geologic perspective. *Natural Hazards* v. 26, p. 7–34.
9. Daniell, J. E., Schaefer, A. M., & Wenzel, F. (2017) Losses Associated with Secondary Effects in Earthquakes. *Frontiers in Built Environment* v. 3, p. 1–14.
10. Dean, W. E. Jr. (1974) Determination of carbonate and organic matter in calcareous sediments and sedimentary rocks by loss on ignition: Comparison with other methods. *Journal of Sedimentary Petrology* v. 44, p. 242–248.
11. DeMets, C., & Dixon, T. H. (1999) New kinematic models for Pacific-North America motion from 3 Ma to present, I: Evidence for steady motion and biases in the NUVEL-1A model. *Geophysical Research Letters* v. 26(13), p. 1921–1924.
12. Debret, M., Desmet, M., Balsam, W., Copard, Y., Francus, P., & Laj, C. (2006). Spectrophotometer analysis of Holocene sediments from an anoxic fjord: Saanich Inlet, British Columbia, Canada. *Marine Geology*, v. 229(1–2), p. 15–28.
13. Galehouse, J. S. (1971) Point counting. In *Procedures in Sedimentary Petrology*: Wiley Interscience: New York, NY, USA p. 385–407.
14. Gassley, W., (1974) Geochemistry and Tectonics of the Crescent Volcanic Rocks, Olympic Peninsula, Washington. *Geological Society of America Bulletin* v. 85, p. 785-794.
15. Gilli, A., Anselmetti, F.S., Glur, L., Wirth, S.B., 2013. Lake sediments as archives of recurrence rates and intensities of past flood events. In: Schneuwly-Bollschweiler, M., Stoffel, M., Rudolf-Miklau, F. (Eds.), *Dating Torrential Processes on Fans and Cones e Methods and Their Application for Hazard and Risk Assessment*, *Advances in Global Change research* v. 47, p. 225-242.

16. Goldfinger, C., Nelson, C. H., & Johnson, J. E. (2003) Holocene Earthquake Records From the Cascadia Subduction Zone and Northern San Andreas Fault based on Precise Dating of Offshore Turbidites. *Annual Review of Earth and Planetary Sciences* v. 31, p. 555–577.
17. Goldfinger, C. (2011) Submarine Paleoseismology Based on Turbidite Records. *Annual Review of Marine Science*, v. 3, p. 35–66.
18. Goldfinger, C., Nelson, C.H., Morey, A.E., Johnson, J.E., Patton, J.R., Karabanov, E., Gutiérrez- Pastor, J., Eriksson, A.T., Gràcia, E., Dunhill, G., Enkin, R.J., Dallimore, A., Vallier, T. (2012) Turbidite Event History—Methods and Implications for Holocene Paleoseismicity of the Cascadia Subduction Zone. *U.S. Geological Survey Professional Paper 1661–F* p. 332.
19. Gu, Z., Rioual, P., Mackay, A. W., Leng, M. J., Kendrick, C. P., Wang, L., ... Panizzo, V. N. (2012) Influence of the ratio of planktonic to benthic diatoms on lacustrine organic matter $\delta^{13}\text{C}$ from Erlongwan maar lake, northeast China. *Organic Geochemistry* v. 54, p. 62–68.
20. Hampton S.E., Fradkin, S.C., Leavit, P.R., and Rosenberger, E.E. (2011) Disproportionate importance of nearshore habitat for the food web of a deep oligotrophic lake. *Marine and Freshwater Research*, v. 62, p.350-358.
21. Heaton, T. H., and Hartzell, S. H. (1986) Source Characteristics of Hypothetical Subduction Earthquakes in the Northwestern United States. *Bulletin of the Seismological Society of America*, v. 76(3), p. 675–708.

22. Heiri, O., Lotter, A., & Lemcke, G. (2001). Loss on ignition as a method for estimating organic and carbonate content in sediments. *Journal of Paleolimnology*, v. 25, p. 101–110.
23. Highland, L. M. (2001) An account of Preliminary Landslide Damage and Losses resulting from the February 28, 2001, Nisqually, Washington, Earthquake. U.S. Geologic Survey Report 03-211
24. Hilbe, M., & Anselmetti, F. S. (2014) Signatures of slope failures and river-delta collapses in a perialpine lake (Lake Lucerne, Switzerland). *Sedimentology*, v. 61(7), p.1883–1907.
25. Howarth, J. D., Fitzsimons, S. J., Norris, R. J., & Jacobsen, G. E. (2014). Lake sediments record high intensity shaking that provides insight into the location and rupture length of large earthquakes on the Alpine Fault , New Zealand. *Earth and Planetary Science Letters* v.403, p. 340–351.
26. Hutchinson, I., & Clague, J. (2017). Were they all giants? Perspectives on late Holocene plate-boundary earthquakes at the northern end of the Cascadia subduction zone. *Quaternary Science Reviews* v.169, p. 29–49.
27. Hutchinson, I., Butler, V.L., Campbell, S.K., Sterling, S.L., Etnier, M.A., Bovy, K.M. (2019) Impacts of resource fluctuations and recurrent tsunamis on the occupational history of Číxwicən, a Salishan village on the southern shore of the Strait of Juan de Fuca, Washington State, U.S.A. *journal of Archaeological Science: Reports*, v. 23, p. 1131-1142.

28. Jacoby, G. C., D. E. Bunker, and B. E. Benson. (1997) Tree-ring Evidence for an A.D. 1700 Cascadia Earthquake in Washington and Northern Oregon. *Geology* v. 25(11), p. 999–1000.
29. Keefer, D. K. (2002) Investigating landslides caused by earthquakes - A historical review. *Surveys in Geophysics* v.23, p. 473–510.
30. Kingston, J. C., Lowe, R. E., Stoermer, E.F., Ladewski, T.B. (2008). Spatial and Temporal Distribution of Benthic Diatoms in Northern Lake Michigan. *Ecological Society of America*, v. 64(6), p.1566–1580.
31. Kroon, D., Alexander, I., and Darling, K. (1993). Planktonic and Benthic Foraminiferal abundances and their ratios (P/B) as expressions of Middle-Late Quaternary changes in water mass distribution and flow intensity on the Northeastern Australian Margin. *Proceedings of the Ocean Drilling Program: Scientific Results*, v. 133(133), p. 181–188.
32. Kulkarni, R., Wong, I., Zachariasen, J., Goldfinger, C., & Lawrence, M. (2013). Statistical analyses of great earthquake recurrence along the Cascadia subduction zone. *Bulletin of the Seismological Society of America*, v. 103(6), p.3205–3221.
33. Leithold, E. L., Wegmann, K. W., Bohnenstiehl, D. R., Joyner, C. N., & Pollen, A. F. (2019) Repeated megaturbidite deposition in Lake Crescent, Washington, USA, triggered by Holocene ruptures of the Lake Creek-Boundary Creek fault. *GSA Bulletin*.
34. Leithold, E. L., Wegmann, K. W., Bohnenstiehl, D. R., Smith, S. G., Noren, A., and O'Grady, R. (2018) Slope failures within and upstream of Lake Quinault,

- Washington, as uneven responses to Holocene earthquakes along the Cascadia subduction zone. *Quaternary Research (United States)*, v. 89, p. 178–200.
35. McCaffrey, R., Qamar, A. I., King, R.W., Wells, R., Khazaradze, G., Williams, C.A., Stevens, C.W., Vollick, J.J., and Zwick, P.C. (2007) Fault locking, block rotation and crustal deformation in Pacific Northwest. *Geophysical Journal. V.* 169, p. 1315-1340.
 36. McMillan, A. D. and Hutchinson, I. (2005). When the Mountain Dwarfs Danced: Aboriginal Traditions of Paleoseismic Events along the Cascadia Subduction Zone of Western North America. *Ethnohistory*, v. 49(1), p.41–68.
 37. Moernaut, J., Van Daele, M., Strasser, M., Clare, M. A., Heirman, K., Viel, M., De Batist, M. (2017) Lacustrine turbidites produced by surficial slope sediment remobilization: A mechanism for continuous and sensitive turbidite paleoseismic records. *Marine Geology*, v. 384, p. 159–176.
 38. Moran, P.W., Cox, S.E., Embrey, S.S., Huffman, R.L., Olsen, T.D., Fradkin, S.C. (2013) Sources and sinks of nitrogen and phosphorus in a deep, oligotrophic lake, Lake Crescent, Olympic National Park, Washington: U.S. Geological Survey Report 5107. p. 1-56.
 39. Nelson, A.R., Kelsey, H.M., Witter, R.C. (2005) Great earthquakes of variable magnitude at the Cascadia subduction zone. *Quaternary Research* v. 65, p. 354-365.
 40. Olsson, I. (1986) Radiometric methods. In: Berglund B (ed) *Handbook of Holocene Palaeoecology and Palaeohydrology*: Wiley, Chichester, p. 273–312.

41. McLennan, S. M., Hemming, S., McDaniel, D. K., and Hanson, G. N., 1993, Geochemical approaches to sedimentation, provenance, and tectonics, in Johnsson, M. J., and Basu, A., eds., processes controlling the composition of clastic sediments: Boulder, Colorado, Geological Society of America Special Paper 284, p. 21-40
42. PNSN. Some details of felt report, aftershocks, and other earthquakes.
<https://assets.pnsn.org/notable/Duvall/duval.notes.html> [March 18, 2019]
43. Pollen, A. F. (2016) The Sedimentary Record of Past Earthquakes Identified in Holocene Sediments of Lake Crescent, Washington (Master's Thesis). Retrieved from <https://repository.lib.ncsu.edu/bitstream/handle/1840.16/11366/etd.pdf?sequence=2&isAllowed=y>
44. Pringle, P., Wegmann, K., Pontbriand, D., and Walker, 2010, Some recent discoveries pertaining to subfossil forests in the Pacific Northwest: Examples from Lake Crescent and Lower Dry Beds Lakes, Olympic Mountains, Washington: Northwest Scientific Association, 82nd Annual Meeting, March 24–27, Centralia College, Washington State, USA, p. 77–78.
45. Reimer, P., Bard, E., Bayliss, A., Beck, J., Blackwell, P., Bronk Ramsey, C., Buck, C., Cheng, H., Edwards, R., Friedrich, M., Grootes, P., Guilderson, T., Hafliðason, H., Hajdas, I., Hatté, C., Heaton, T., Hoffmann, D., Hogg, A., Hughen, K., Kaiser, K., Kromer, B., Manning, S., Niu, M., Reimer, R., Richards, D., Scott, E., Southon, J., Staff, R., Turney, C., Van Der Plicht, J. (2013) IntCal13 and Marine13 Radiocarbon Age Calibration Curves 0–50,000 Years cal BP. Radiocarbon v. 55(4), p. 1869-1887.

46. Rosén, P., Cunningham, L., Vonk, J., & Karlsson, J. (2009) Effects of climate on organic carbon and the ratio of planktonic to benthic primary producers in a subarctic lake during the past 45 years. *Limnology and Oceanography*, v. 54(5), p. 1723–1732.
47. Satake, K., Shimazaki, Y., Tsuji, and K. Uyeda. (1996) Time and Size of a Great Earthquake in Cascadia Inferred from Japanese Tsunami Records of January 1700. *Nature* v. 379, p. 246–249.
48. Schasse, H.W. (2003) Geologic map of the Washington portion of the Port Angeles 1:100,000 quadrangle. Washington Division of Geology and Earth Resources Open File Report, 1 Sheet.
49. Schlolaut, G., Brauer, A., Marshall, M. H., Nakagawa, T., Staff, R. A., Bronk Ramsey, C., ... Haraguchi, T. (2014). Event layers in the Japanese Lake Suigetsu “SG06” sediment core: Description, interpretation and climatic implications. *Quaternary Science Reviews*, v. 83, p. 157–170.
50. Schreiber, N., Garcia, E., Kroon, A., Ilsøe, P. C., Kjær, K. H., & Andersen, T. J. (2014). Pattern recognition on X-ray fluorescence records from copenhagen lake sediments using principal component analysis. *Water, Air, and Soil Pollution*, v. 225(12), p. 224-235.
51. Sumner, E. J., Siti, M. I., McNeill, L. C., Talling, P. J., Henstock, T. J., Wynn, R. B., Permana, H. (2013) Can turbidites be used to reconstruct a paleoearthquake record for the central Sumatran margin? *Geology* v. 41(7), p. 763–766.
52. USGS. (2016) Shakemap Scenario: uscasc9.0_expanded_peak_se. Earthquake Hazards Program. M 9.0 (Cascadia).

http://earthquake.usgs.gov/earthquakes/shakemap/global/shake/casc9.0_expand_peak_se/ [March 25, 2019]

53. Van Daele, M., Moernaut, J., Doom, L., Boes, E., Fontijn, K., Heirman, K., De Batist, M. (2015) A comparison of the sedimentary records of the 1960 and 2010 great Chilean earthquakes in 17 lakes: Implications for quantitative lacustrine palaeoseismology. *Sedimentology*, v. 62, p.1466–1496.
54. Van Daele, M., Meyer, I., Moernaut, J., De Decker, S., Verschuren, D., & De Batist, M. (2017). A revised classification and terminology for stacked and amalgamated turbidites in environments dominated by (hemi)pelagic sedimentation. *Sedimentary Geology*, v. 357, p. 72–82.
55. Van Daele, M., Araya-cornejo, C., Pille, T., Vanneste, K., Moernaut, J., Schmidt, S. Cisternas, M. (2019). Distinguishing intraplate from megathrust earthquakes using lacustrine turbidites, v. 47(2), p. 1–4.
56. Washington Military Department (2015) This month in history: Two major earthquakes hit Puget Sound. Washington emergency Management Division.
<https://mil.wa.gov/blog/news/post/big-1965-earthquake-happened-50-years-ago>
[March 18, 2019]
57. Wells, R.E., Weaver, C.S., Blakely, R.J. (1998) Fore-arc migration in Cascadia and its neotectonic significance. *Geology* v. 26(8), p. 759-762.

APPENDICES

APPENDIX A. Summary of gravity coring sites.

Core ID	Latitude	Longitude	Length (cm)	Depth of Core Top (m)	Depth of Core Bottom (m)	Water Depth (m)	Surface Water Elevation (m)
SHAKE-CRSC18-1A-G-1	48.09334	-123.79646	51	0	0.51	10.7	177.1
SHAKE-CRSC18-2A-G-1	48.08214	-123.7882	50	0	0.5	144.2	177.1
SHAKE-CRSC18-3A-G-1	48.08958	-123.77111	51	0.06	0.57	141.7	177.1
SHAKE-CRSC18-4A-G-1	48.08938	-123.78054	70	0	0.7	143.3	177.1
SHAKE-CRSC18-5A-G-1	48.05669	-123.81651	74	0	0.74	178.0	177.1
SHAKE-CRSC18-6A-G-1	48.05801	-123.82771	74	0	0.74	183.5	177.1
SHAKE-CRSC18-7A-G-1	48.05802	-123.84009	74	0	0.74	184.1	177.1
SHAKE-CRSC18-8A-G-1	48.05466	-123.84011	56	0	0.56	180.4	177.1
SHAKE-CRSC18-9A-G-1	48.06067	-123.84049	74	0	0.74	183.8	177.1
SHAKE-CRSC18-10A-G-1	48.05751	-123.85372	74	0	0.74	184.1	177.1
SHAKE-CRSC18-11A-G-1	48.05793	-123.86555	72.5	0	0.725	172.5	177.1
SHAKE-CRSC18-12A-G-1	48.06403	-123.89274	51	0.05	0.56	81.9	177.1
SHAKE-CRSC18-13A-G-1	48.05815	-123.80574	54	0	0.54	153.9	177.1

APPENDIX B. Summary of point counts performed on samples from the base of EL3-A along the west-east transect in the southern basin.

Core	Section Depth (cm)	Percent Volcanic-Lithic	Percent Sedimentary-Lithic
5A	54-55	91	9
6A	49-49.5	82	18
7A	52.5-53.5	76	24
8A	45-46	52	48
10A	46.5-47	71	29
11A	54-55	63	37

APPENDIX C. Ratios of planktonic to benthic diatom valves in samples collected from EL3-A and background sediment. Examination of assemblages was performed at 20x magnification. Samples exhibiting highest relative abundance are described as abundant, next highest is listed as common, then few and rare.

Core ID	Section Depth (cm)	Sed. Package	% Planktonic	Average % Planktonic	Ratio of P: B	Average Ratio of P: B	Abundance	Preservation
7A-1G	40.5-41.5	EL3-A	0.77	0.76	3.34	3.20	abundant	fragmented / partially preserved
7A-1G		EL3-A	0.76		3.21			
7A-1G		EL3-A	0.75		3.04			
7A-1G	43.5-44.5	EL3-A	0.72	0.73	2.54	2.64	abundant	fragmented / partially preserved
7A-1G		EL3-A	0.74		2.77			
7A-1G		EL3-A	0.72		2.60			
7A-1G	48.5-49.5	EL3-A	0.73	0.71	2.64	2.47	abundant	fragmented / partially preserved
7A-1G		EL3-A	0.69		2.25			
7A-1G		EL3-A	0.72		2.51			
7A-1G	52.5-53.5	EL3-A	0.71	0.72	2.48	2.58	abundant	fragmented / partially preserved
7A-1G		EL3-A	0.74		2.85			
7A-1G		EL3-A	0.71		2.42			
7A-1G	17.5-18	Background	0.77	0.79	3.40	3.74	common/abundant	partially preserved/pristine
7A-1G		Background	0.80		4.06			
7A-1G		Background	0.79		3.76			
10A-1G	65-65.5	Background	0.78	0.80	3.55	3.92	common/abundant	partially preserved/pristine
10A-1G		Background	0.81		4.26			
10A-1G		Background	0.80		3.94			
10A-1G	33.5-34.5	EL3-A	0.74	0.74	2.81	2.78	abundant / common	fragmented / partially preserved
10A-1G		EL3-A	0.73		2.67			
10A-1G		EL3-A	0.74		2.85			
10A-1G	38.5-39.5	EL3-A	0.70	0.71	2.36	2.50	abundant	fragmented / partially preserved
10A-1G		EL3-A	0.72		2.54			
10A-1G		EL3-A	0.72		2.60			

10A-1G	42.5-43.5	EL3-A	0.70	0.70	2.33	2.34	abundant	fragmented / partially preserved
10A-1G		EL3-A	0.69		2.25			
10A-1G		EL3-A	0.71		2.45			
10A-1G	46.5-47	EL3-A	0.71	0.71	2.42	2.41	abundant	fragmented / partially preserved
10A-1G		EL3-A	0.72		2.51			
10A-1G		EL3-A	0.70		2.31			
5A-1G	50-51	EL3-A	0.76	0.76	3.21	3.10	common/abundant	fragmented / partially preserved
5A-1G		EL3-A	0.75		2.96			
5A-1G		EL3-A	0.76		3.12			
5A-1G	51-52	EL3-A	0.70	0.71	2.36	2.50	abundant	fragmented / partially preserved
5A-1G		EL3-A	0.72		2.54			
5A-1G		EL3-A	0.72		2.60			
5A-1G	53-54	EL3-A	0.71	0.72	2.45	2.56	abundant	fragmented / partially preserved
5A-1G		EL3-A	0.73		2.67			
5A-1G		EL3-A	0.72		2.57			
5A-1G	54-55	EL3-A	0.74	0.73	2.77	2.75	common	partially preserved
5A-1G		EL3-A	0.73		2.64			
5A-1G		EL3-A	0.74		2.85			
9A-1G	13.5-14.5	EL1	0.77	0.78	3.35	3.45	common	partially preserved/pristine
9A-1G		EL1	0.78		3.60			
9A-1G		EL1	0.77		3.40			
9A-1G	50.5-51	EL3-A	0.79	0.78	3.65	3.50	common	fragmented / partially preserved
9A-1G		EL3-A	0.78		3.44			
9A-1G		EL3-A	0.77		3.40			
9A-1G	45-45.5	EL3-A	0.71	0.71	2.39	2.40	common/abundant	fragmented / partially preserved
9A-1G		EL3-A	0.70		2.31			
9A-1G		EL3-A	0.72		2.51			
9A-1G	54-55	EL3-A	0.69	0.69	2.17	2.24	abundant	fragmented / partially preserved
9A-1G		EL3-A	0.70		2.33			
9A-1G		EL3-A	0.69		2.20			

8A-1G	19-20	Background	0.79	0.79	3.71	3.80	common/ abundant	partially preserved/ pristine
8A-1G		Background	0.80		3.94			
8A-1G		Background	0.79		3.76			
8A-1G	44-44.5	EL3-A	0.73	0.73	2.64	2.72	abundant	fragmented / partially preserved
8A-1G		EL3-A	0.74		2.85			
8A-1G		EL3-A	0.73		2.67			
8A-1G	43-44	EL3-A	0.75	0.75	3.04	2.94	abundant	fragmented / partially preserved
8A-1G		EL3-A	0.75		2.96			
8A-1G		EL3-A	0.74		2.81			
8A-1G	41-42	EL3-A	0.76	0.75	3.21	3.07	abundant	fragmented / partially preserved
8A-1G		EL3-A	0.75		2.96			
8A-1G		EL3-A	0.75		3.04			
8A-1G	5.5-6	Surface Interface	0.94	0.92	14.38	11.75	few/com mon	partially preserved/ pristine
8A-1G		Surface Interface	0.92		10.76			
8A-1G		Surface Interface	0.91		10.11			
8A-1G	36-36.5	EL1	0.73	0.72	2.70	2.62	common	partially preserved
8A-1G		EL1	0.72		2.51			
8A-1G		EL1	0.73		2.64			
12A-1G	32.5- 33.5	EL1	0.73	0.73	2.74	2.72	common	partially preserved
12A-1G		EL1	0.74		2.77			
12A-1G		EL1	0.73		2.64			
12A-1G	22-23	EL1	0.75	0.74	2.92	2.91	common	partially preserved
12A-1G		EL1	0.74		2.81			
12A-1G		EL1	0.75		3.00			
12A-1G	0.5-1	Surface Interface	0.96	0.94	24.00	17.84	few	partially preserved/ pristine
12A-1G		Surface Interface	0.95		17.18			
12A-1G		Surface Interface	0.93		12.33			

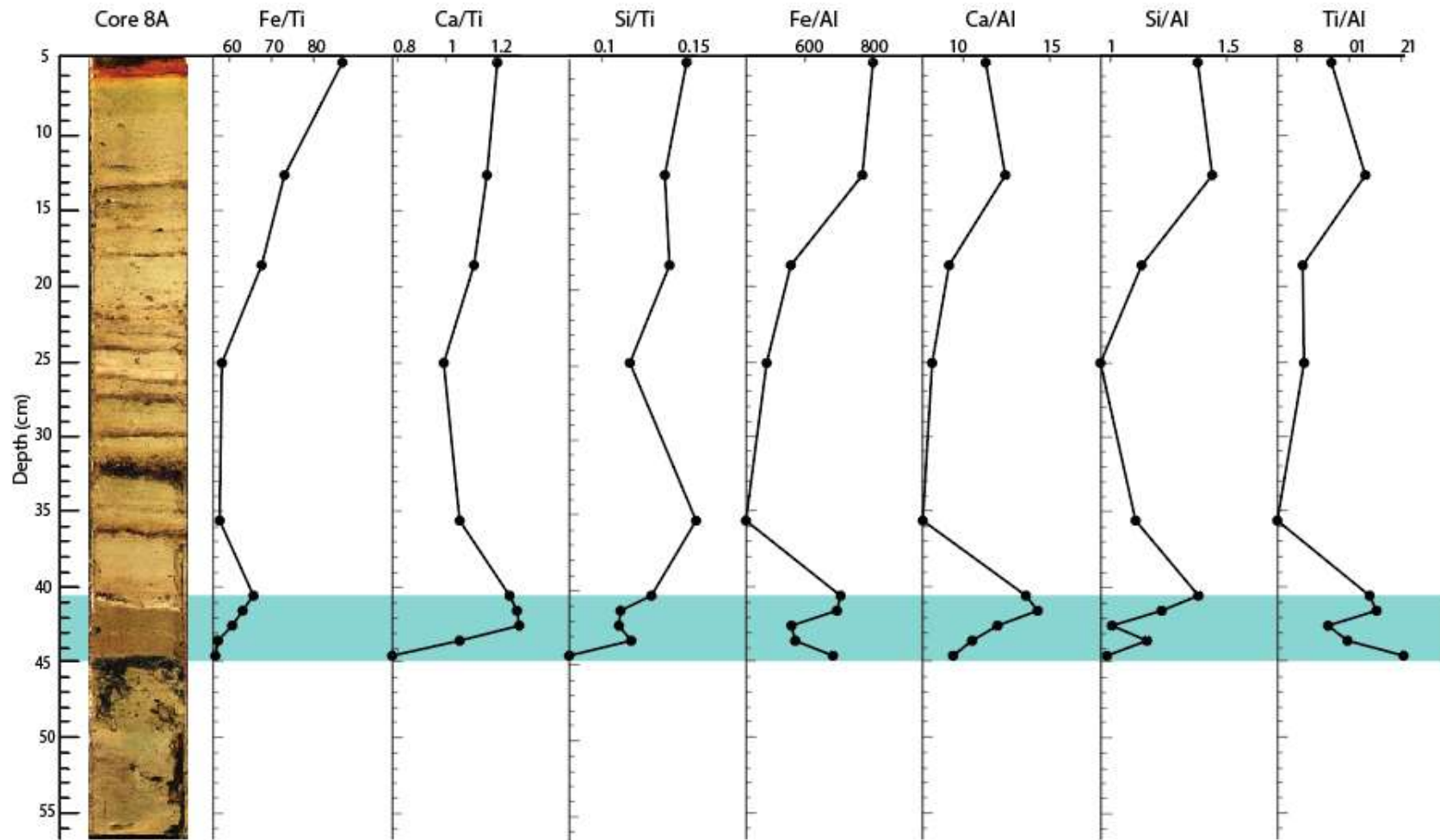
APPENDIX D. Summary of loss on ignition analysis performed on samples from EL3-A in cores 7A-1G, 8A-1G, and 9A-1G.

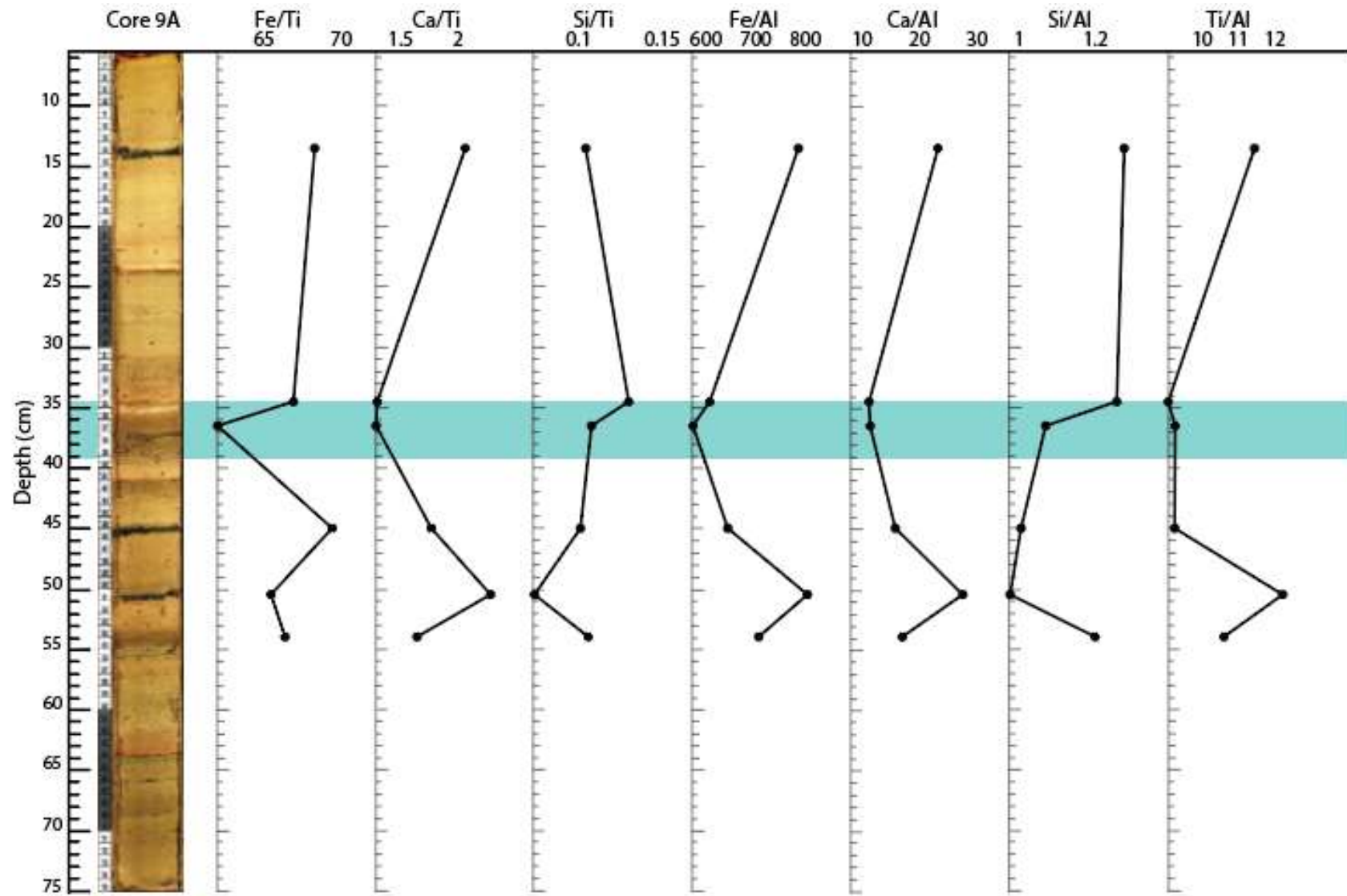
Core ID	Wet-Dry Weight(g)	Dry-Baked Weight (g)	Wet-Baked Weight (g)	LOI %	Average LOI%
9A-1G	0.52	0.03	0.55	0.37	0.4324
9A-1G	0.67	0.04	0.71	0.52	
9A-1G	0.44	0.03	0.47	0.38	
9A-1G	0.58	0.04	0.61	0.46	
7A-1G	0.62	0.03	0.66	0.45	0.58
7A-1G	0.68	0.04	0.71	0.47	
7A-1G	0.62	0.04	0.65	0.48	
7A-1G	0.75	0.04	0.79	0.55	
7A-1G	0.50	0.03	0.53	0.42	
7A-1G	0.64	0.04	0.68	0.58	
7A-1G	0.56	0.04	0.60	0.50	
7A-1G	0.74	0.04	0.78	0.56	
7A-1G	0.82	0.05	0.88	0.68	
7A-1G	0.63	0.04	0.67	0.56	
7A-1G	0.91	0.06	0.97	0.78	
7A-1G	0.81	0.05	0.86	0.62	
7A-1G	0.66	0.04	0.70	0.51	
7A-1G	0.49	0.04	0.53	0.46	
7A-1G	0.70	0.09	0.79	1.13	
8A-1G	0.99	0.06	1.05	0.69	0.54
8A-1G	0.83	0.05	0.88	0.57	
8A-1G	0.71	0.05	0.76	0.63	
8A-1G	0.51	0.04	0.55	0.45	
8A-1G	0.23	0.03	0.26	0.33	

APPENDIX E. Summary of EL3-A thickness in the southern basin.

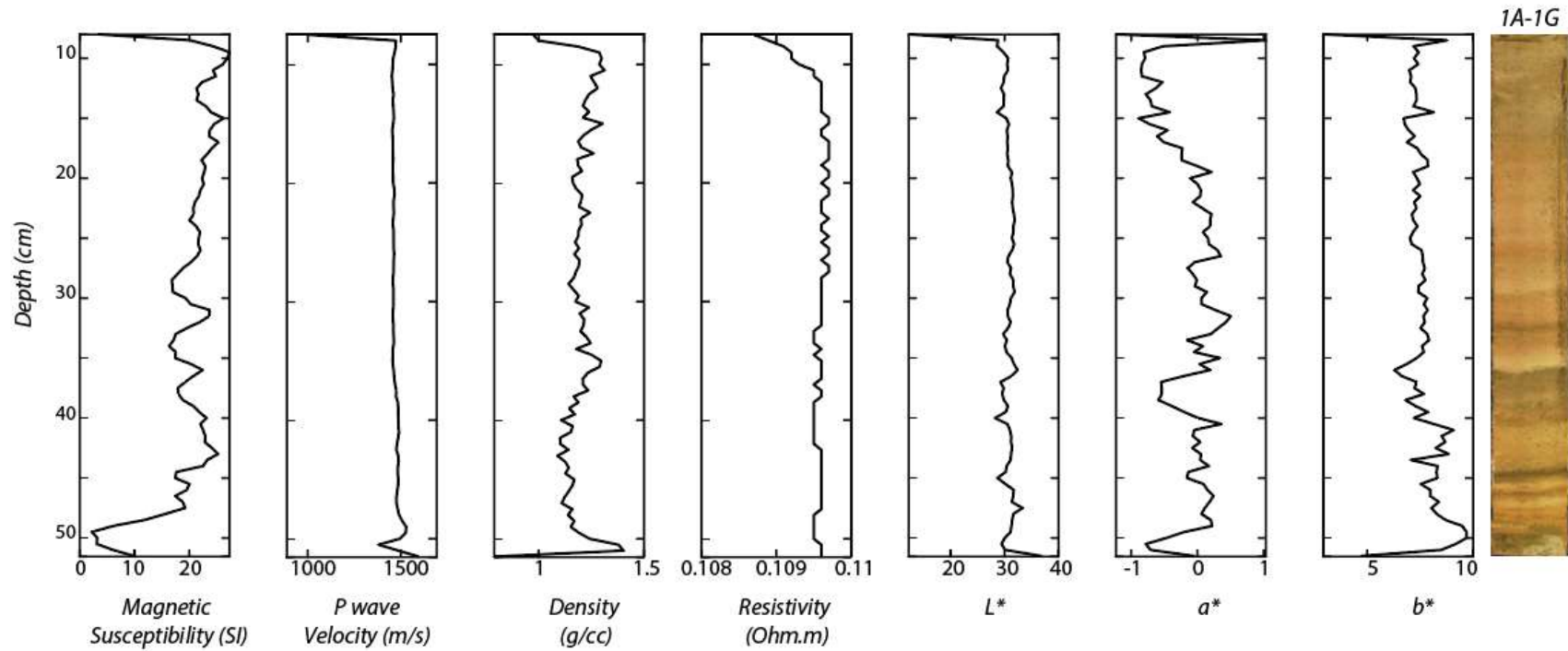
Core ID	Thickness (cm)	Depth to Upper surface of EL3-A from Lake Bottom (cm)
<i>1A-1G</i>	3.0	20.0
<i>2A-1G</i>	N/A	N/A
<i>3A-1G</i>	3.0	31.0
<i>4A-1G</i>	2.0	35.0
<i>5A-1G</i>	5.0	39.0
<i>6A-1G</i>	9.5	29.5
<i>7A-1G</i>	14.0	29.5
<i>8A-1G</i>	4.5	35.5
<i>9A-1G</i>	4.0	29.0
<i>10A-1G</i>	15.5	29.0
<i>11A-1G</i>	5.0	39.0
<i>12A-1G</i>	1.5	31.0
<i>13A-1G</i>	N/A	N/A

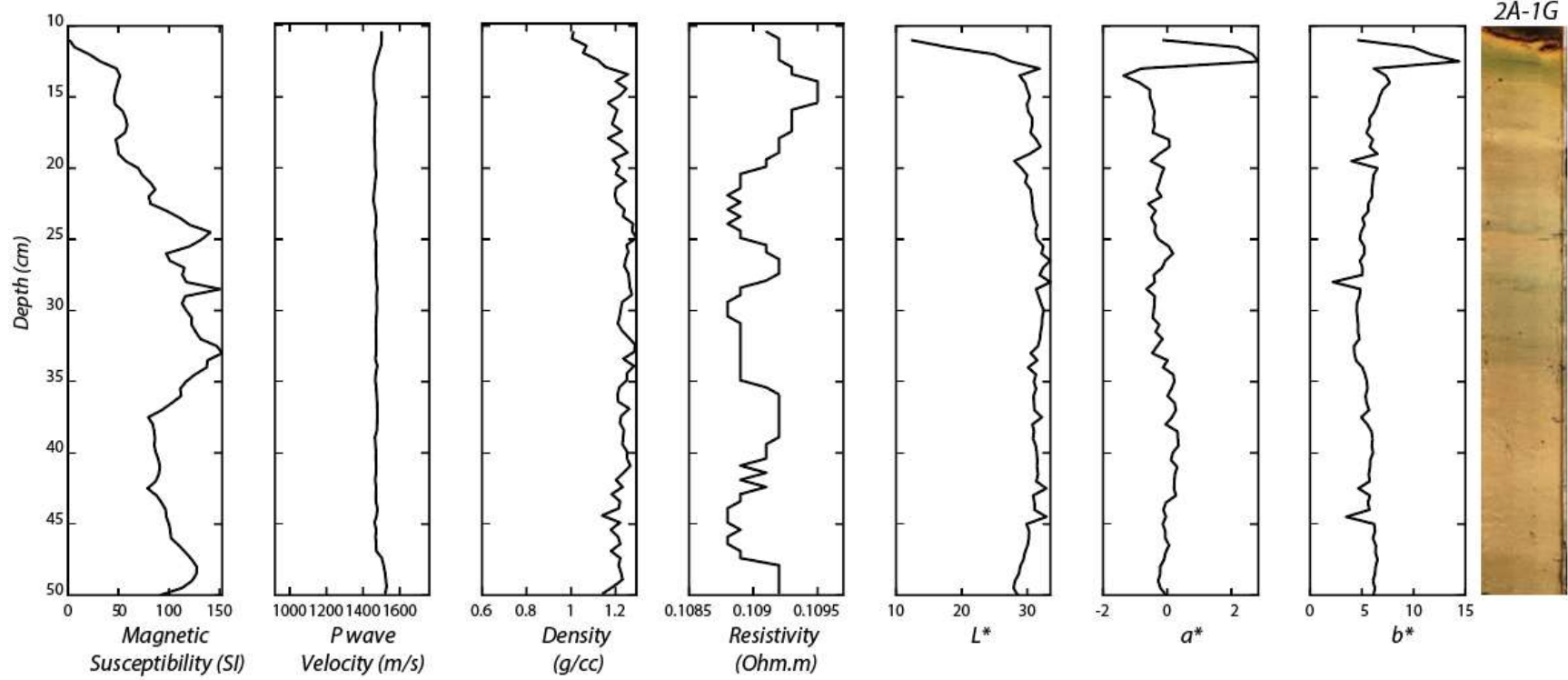
APPENDIX F. CRSC18 gravity cores from the north-south transect of the southern basin alongside elemental ratios from xrf analysis. Green box indicates EL3-A.

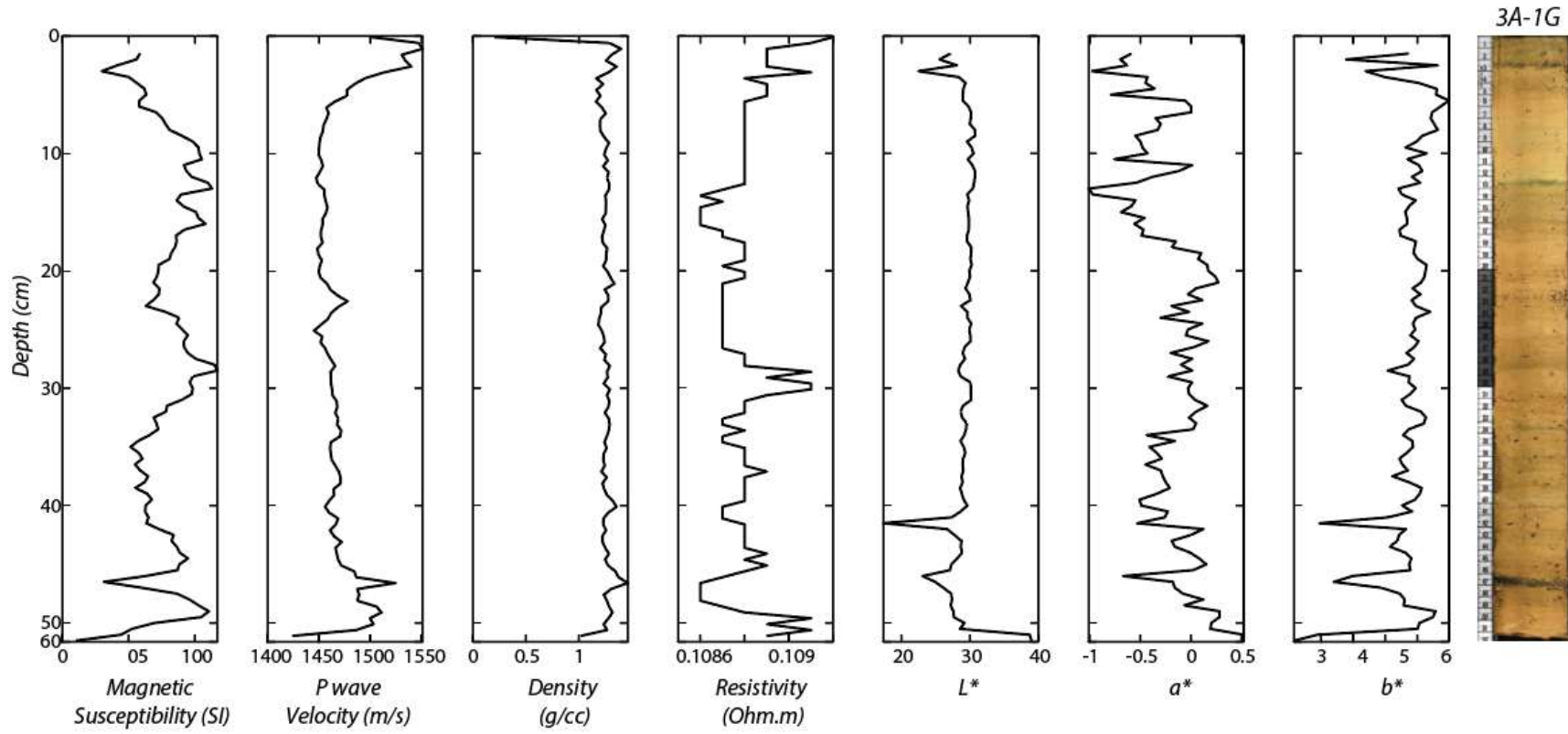


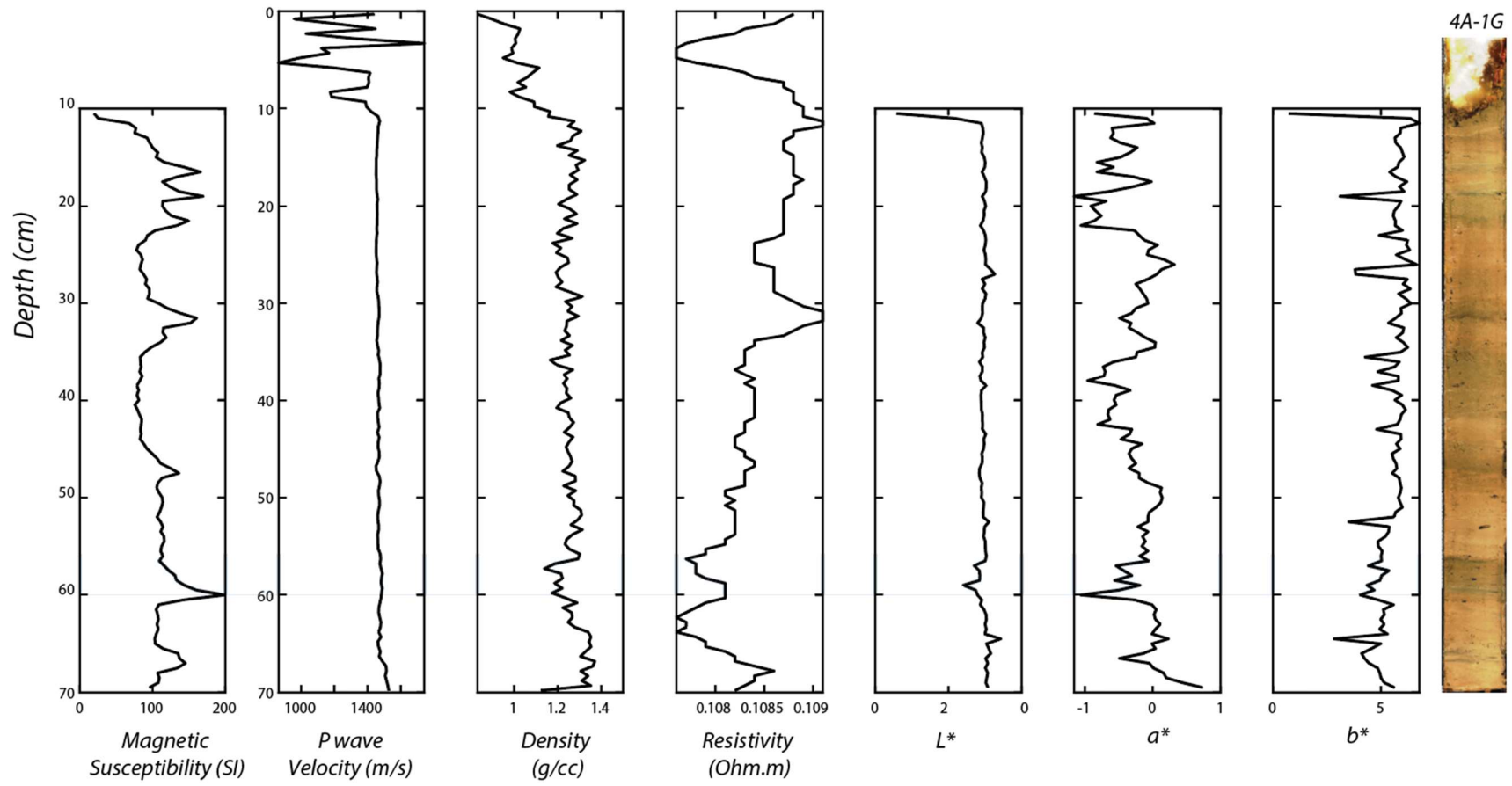


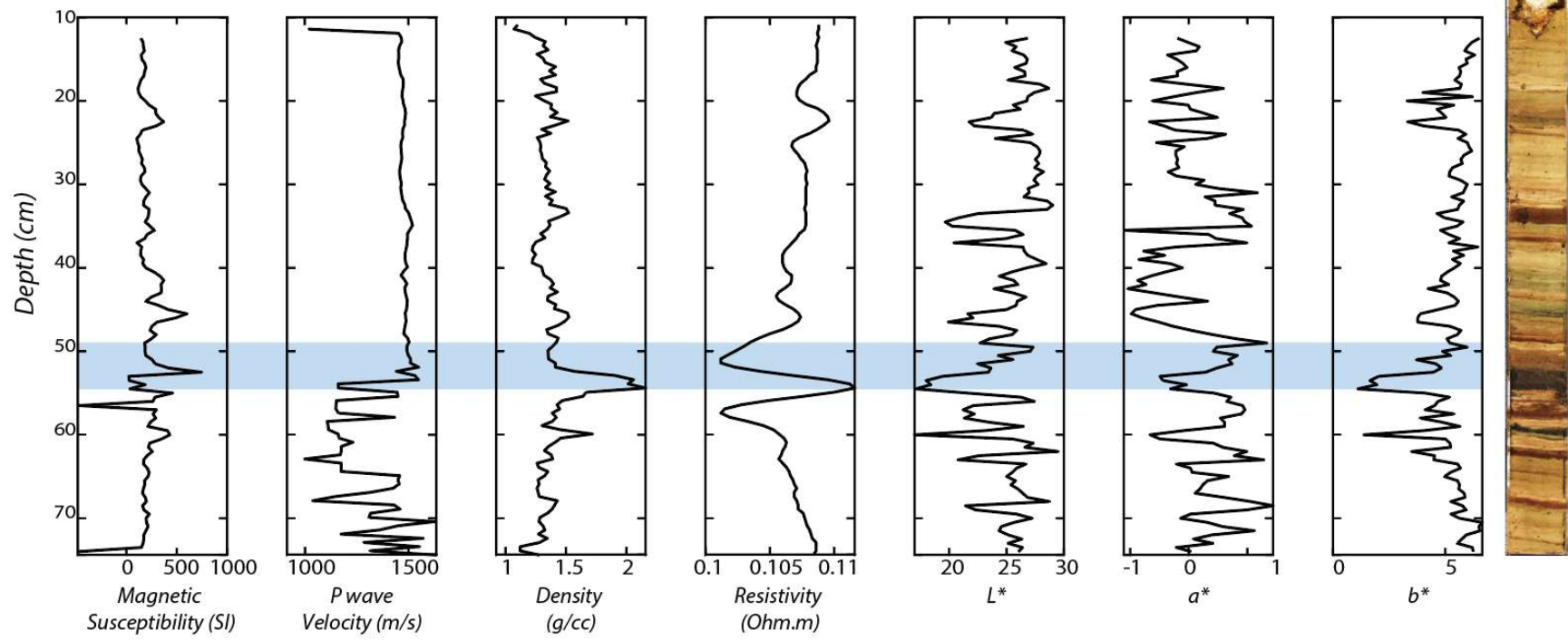
APPENDIX G. Geophysical logging data and color parameters profiles alongside core images of CRSC18 gravity cores. EL3-A is indicated by blue. EL3-A does not clearly present in cores collected from the northern basin, thus remain unmarked.

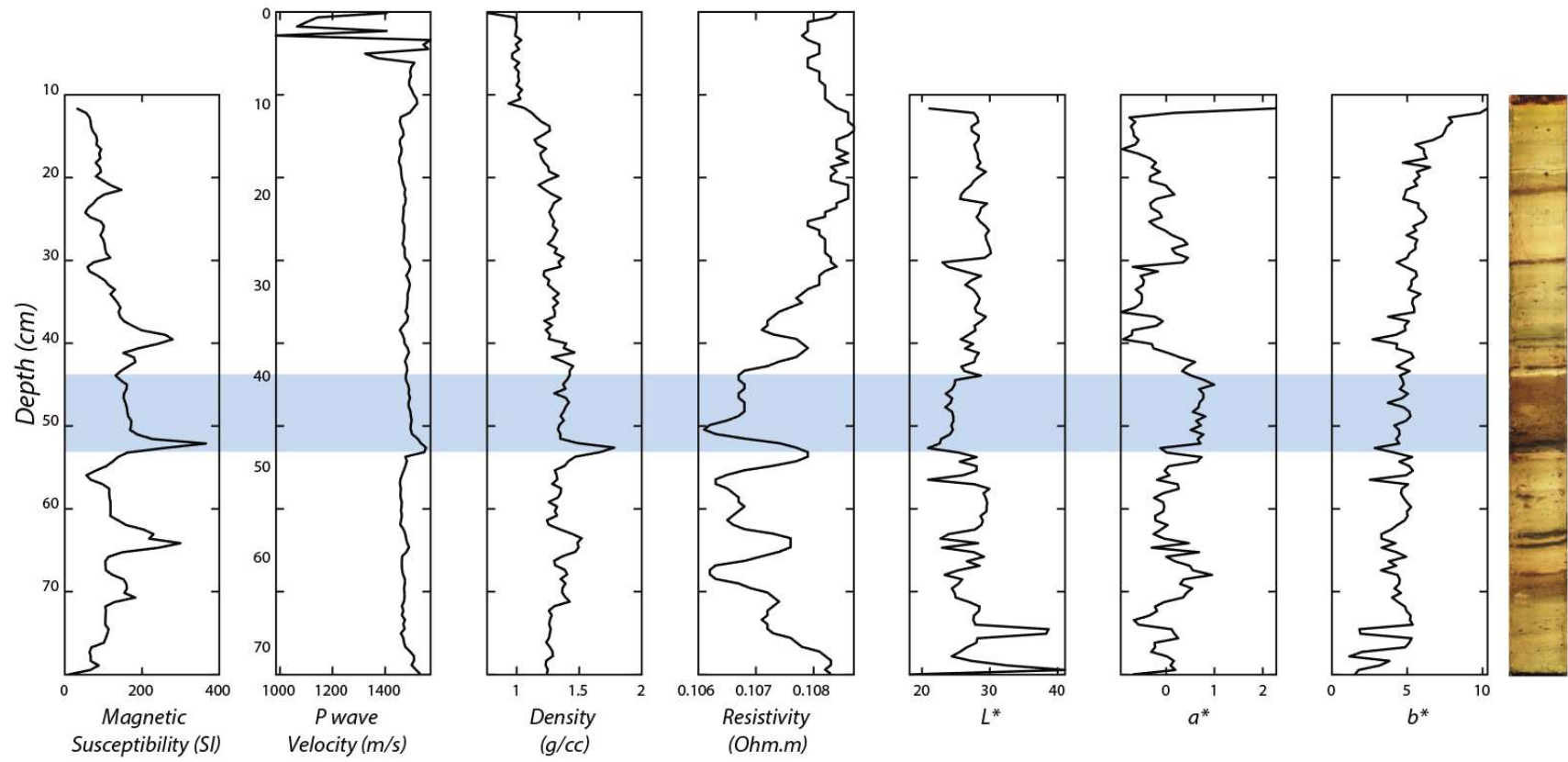


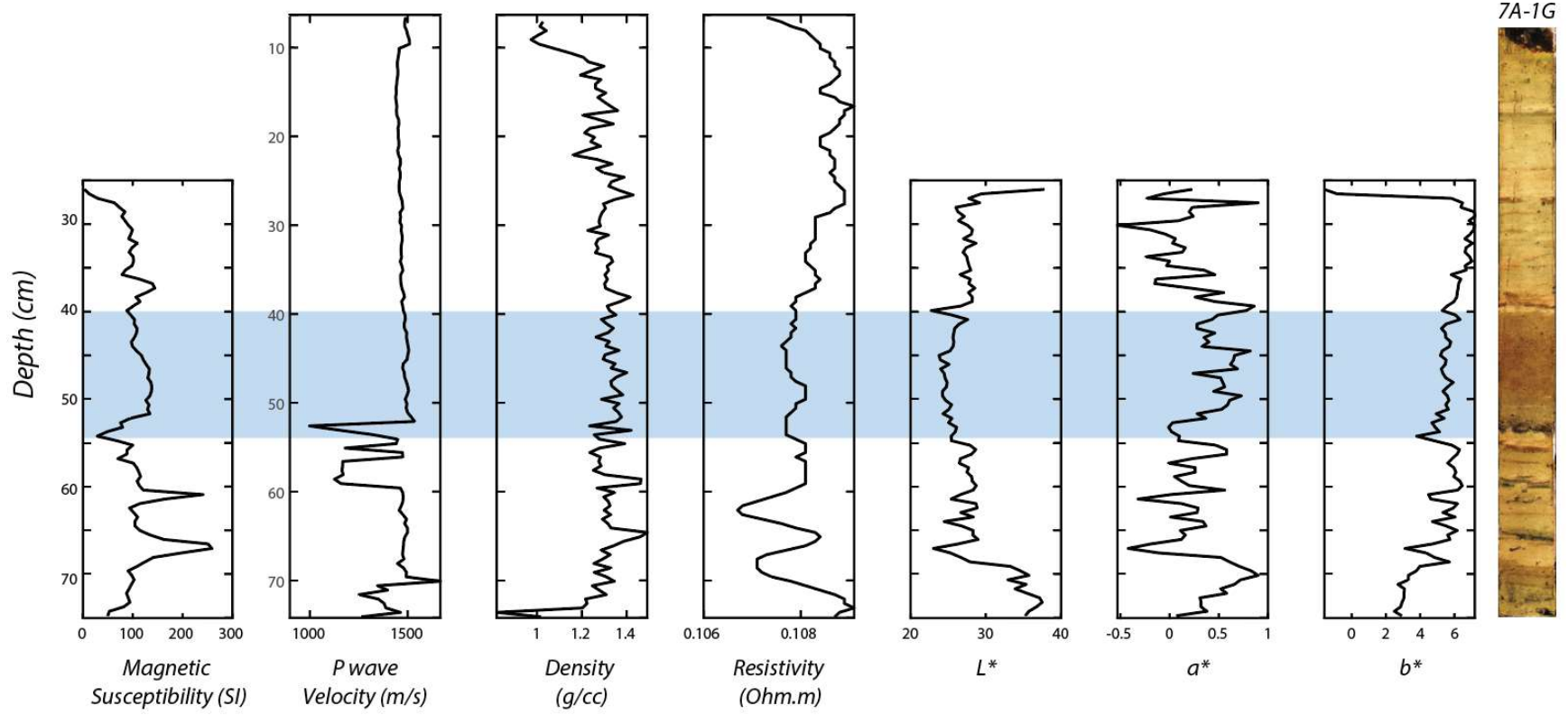




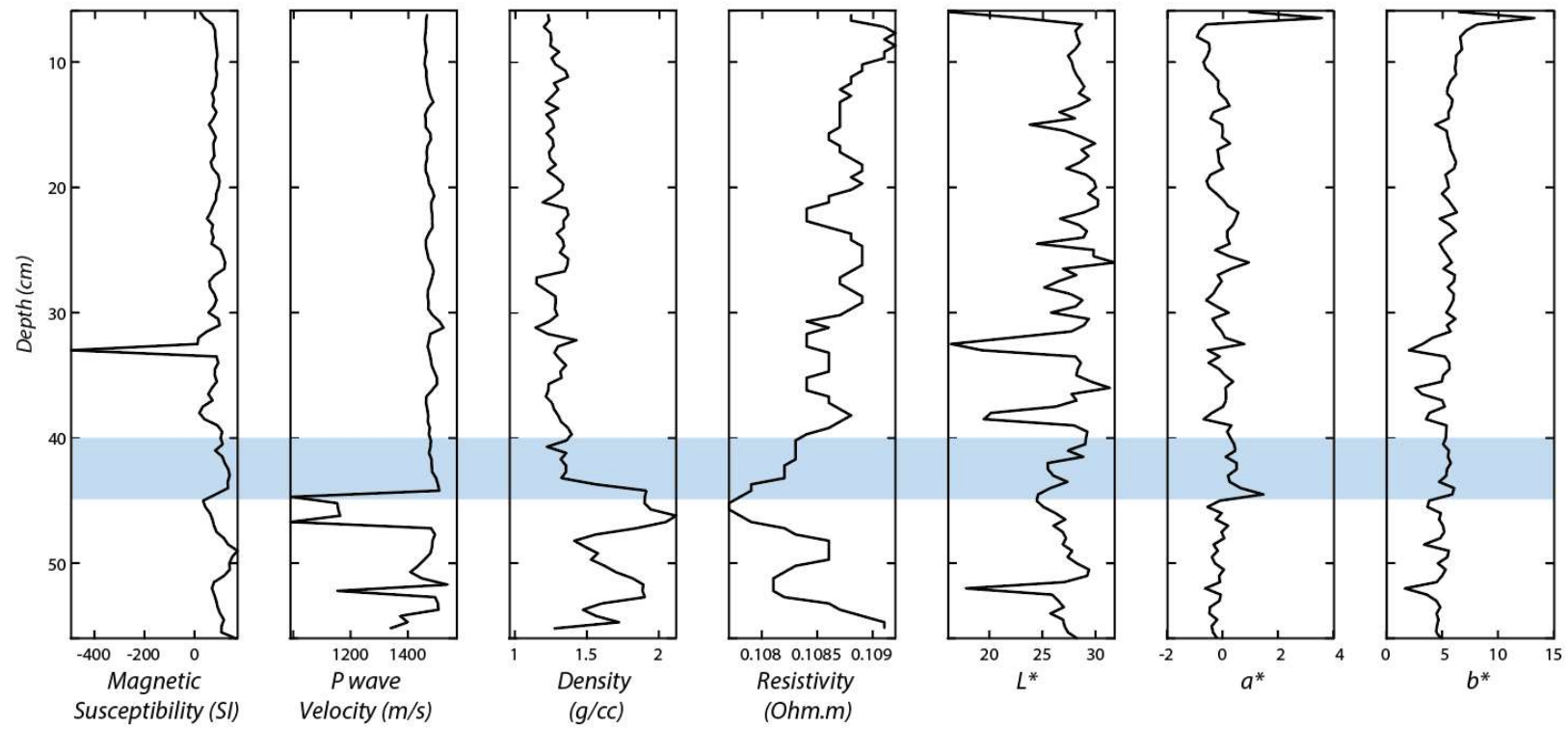


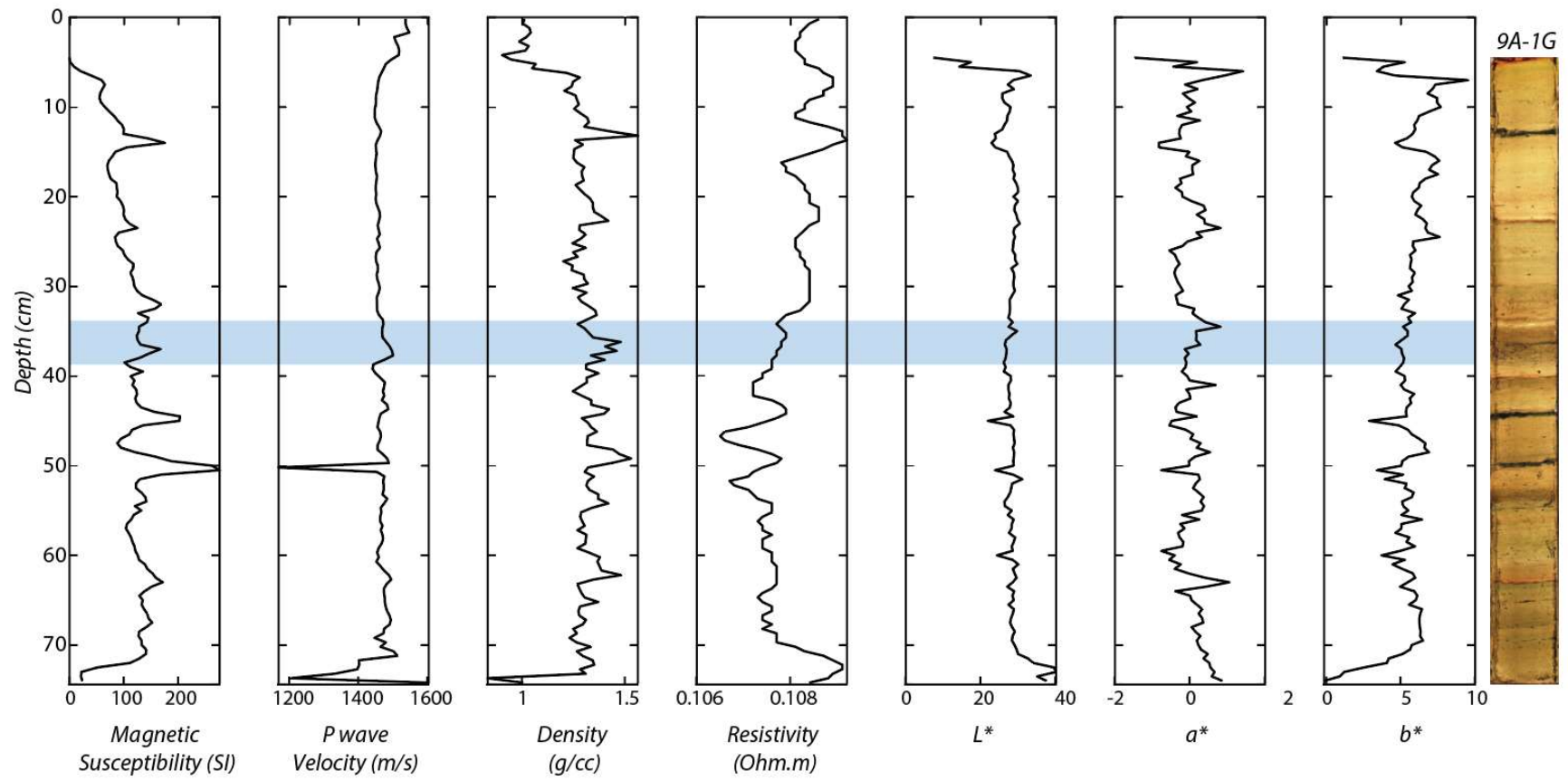


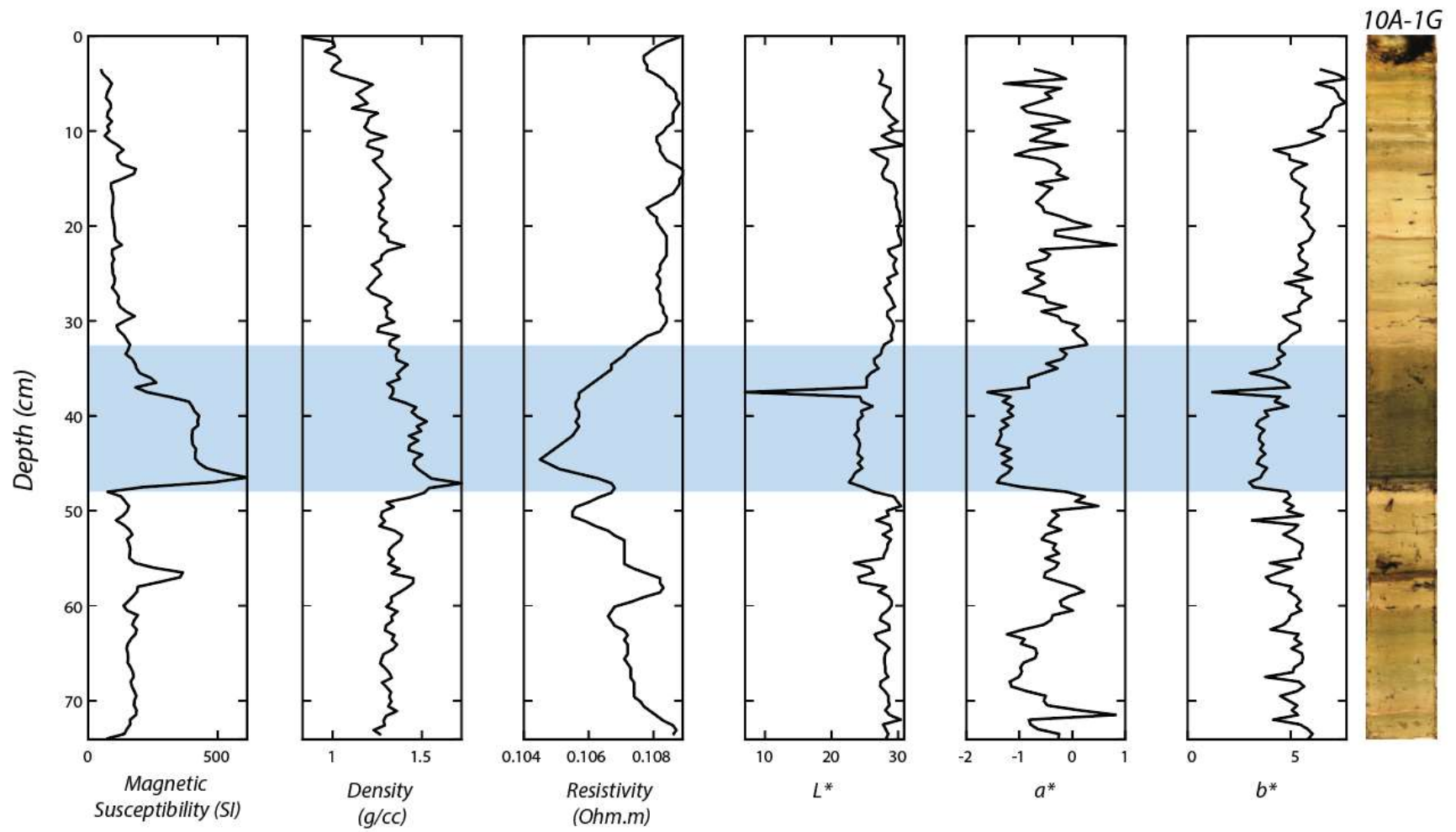




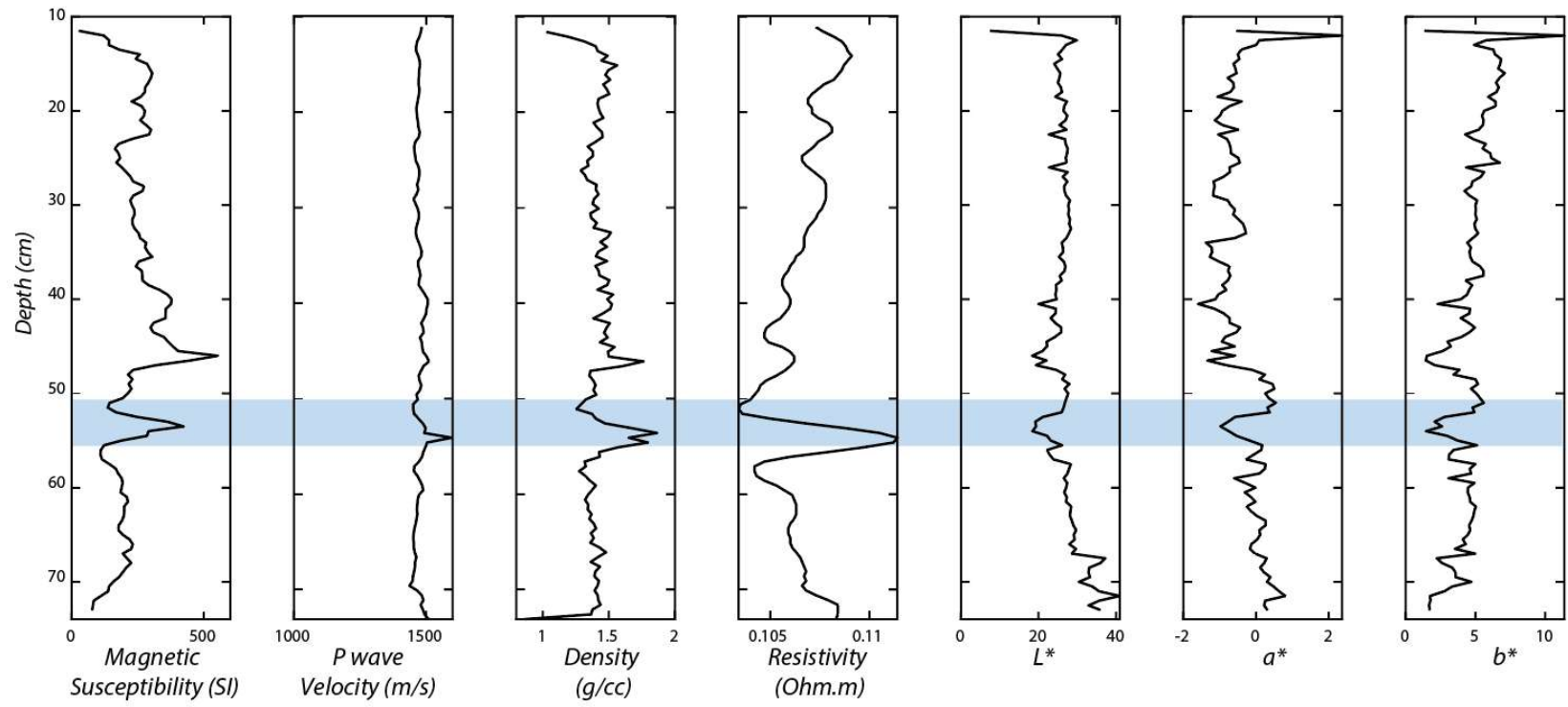
8A-1G

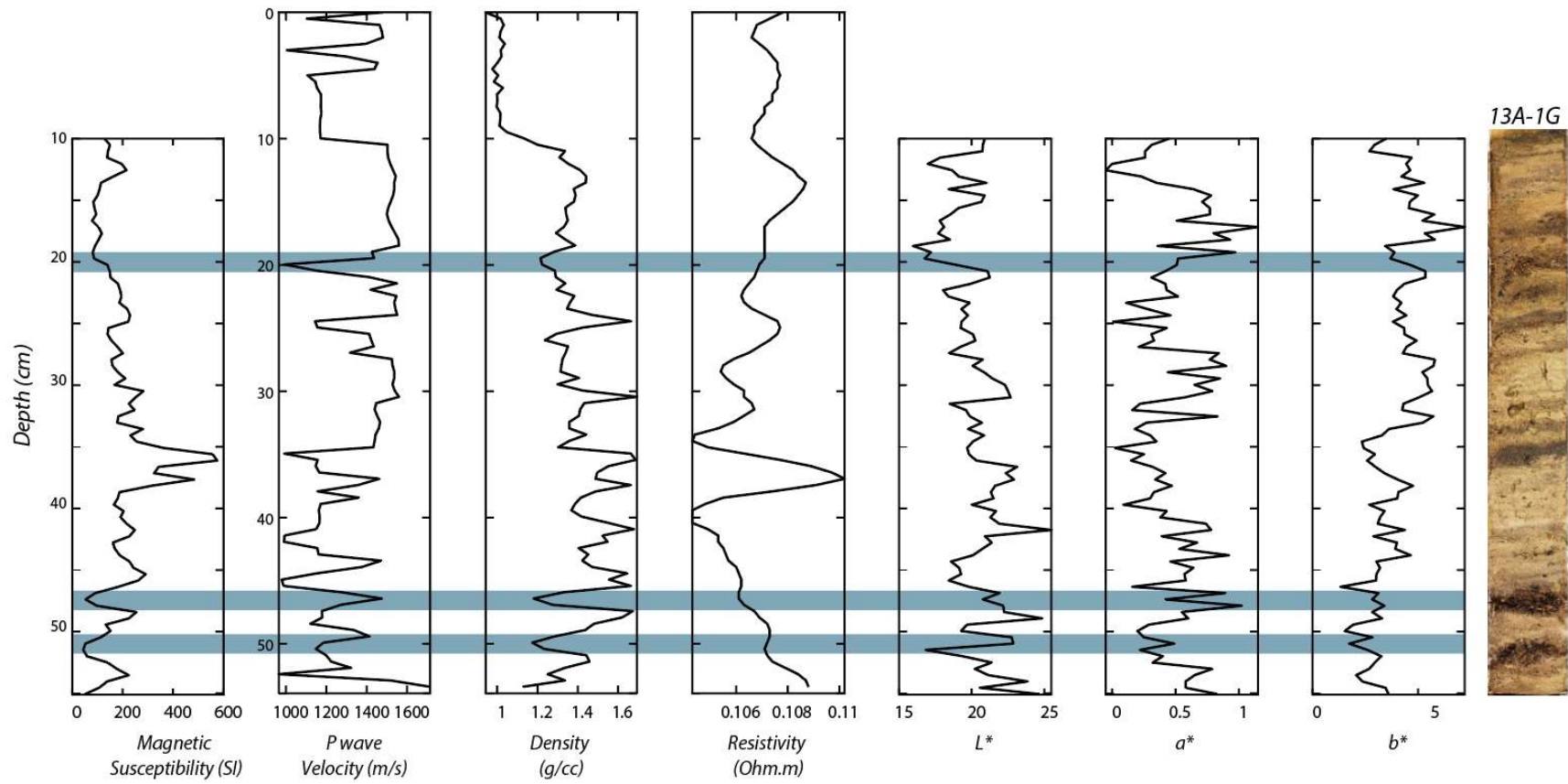




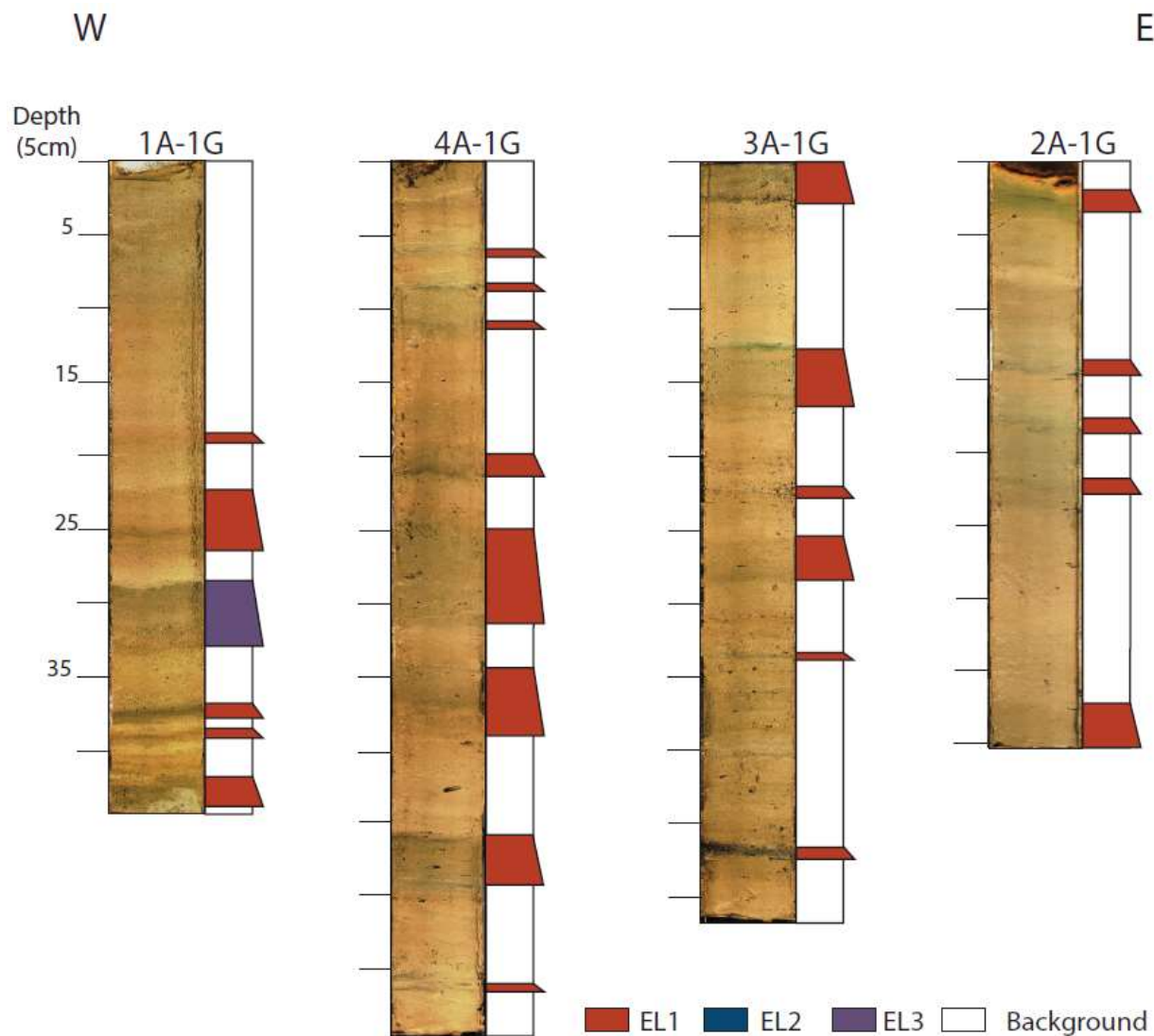


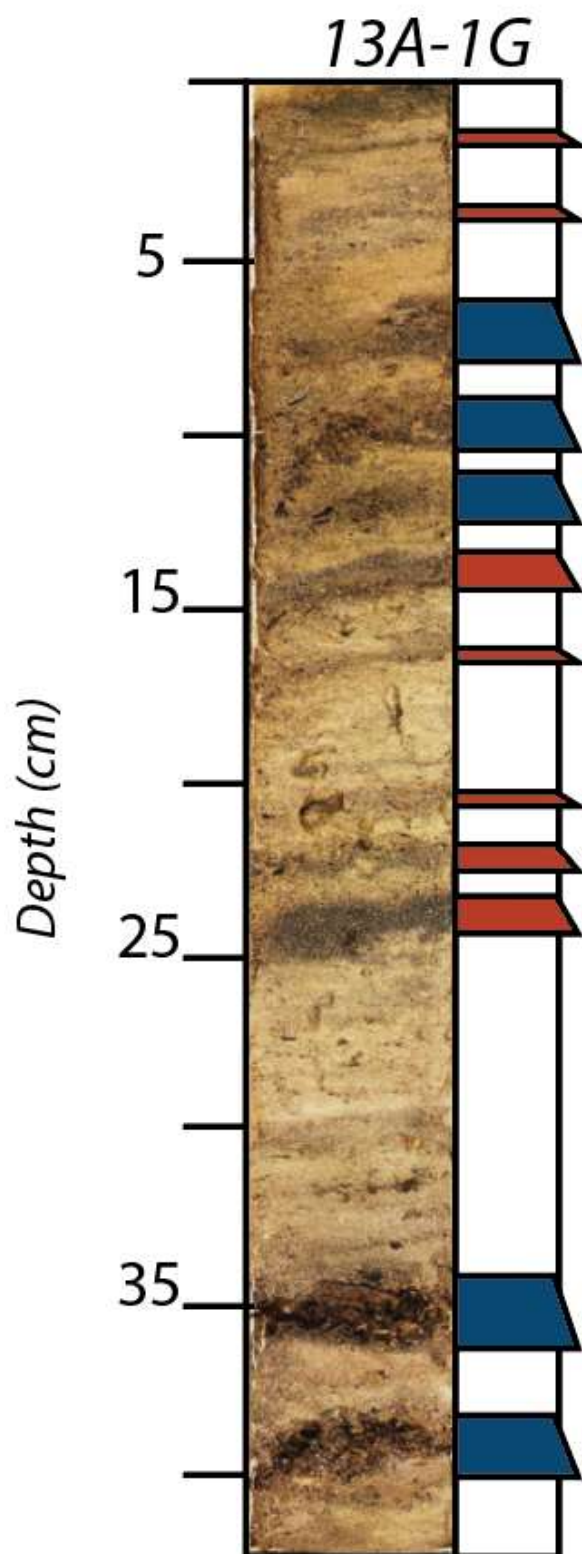
11A-1G





APPENDIX H. Identification of event layers in cores in the northern basin. Core 1A-1G and 4A-1G may contain EL3-A but correlation remains uncertain without radiocarbon ages from northern basin.



APPENDIX I. Core image and event layer classification of core 13A-1G.

Event Layer ID	West-East Transect						North-South Transect		
	12A-1G	11A-1G	10A-1G	7A-1G	6A-1G	5A-1G	9A-1G	7A-1G	8A-1G
EL1-A	0	1	2	1.5	0.5	0.5	0	1.5	0.5
EL1-B	0	1	4	1	3	4.5	1	1.5	3
EL1-C	1	1	1.5	1.5	1.5	3	0.5	1	2.5
EL1-D	2	3	0	0	0	0	0	0	0
EL1-E	4	3	2.5	0.5	2	3	0	0	0
EL1-F	0	0	0	0	0.5	0	0	0	0
EL3-A	1.5	4.5	15	14	10	5	4.5	14	4.5
EL1-G	0	0	0	1	0.5	0.5	0.5	1	0
EL1-H	0	0	0	0.5	0.5	2.5	0	0	0
EL1-I	0	0	0	0.5	1	1.5	0	0	0
EL1-J	0	1	0.5	0.5	1	0.5	1.5	0.5	0
EL1-K	0	2	1.5	1	0	0	1	1	0
EL1-L	0	3	3	2.5	3	1.5	2	2.5	0
EL1-M	0	0.5	0.5	0	0	0	0	0	0
EL1-N	0	0	0	0	0	0	0.5	0.5	0

APPENDIX K. Particle size results.

Core Name	Section Depth (cm)	Mean (µm)	Median	Mode	SD	Variance	<10%	<25%	<50%	<75%	<90%
7A	38.5-39.5	32.98	17.12	31.5	41.16	1694	1.433	6.424	17.12	42.2	35.26
7A	39.5-40.5	40	22.01	34.58	47.85	2290	2.341	8.524	22.01	51.6	105.6
7A	40.5-41.5	59.68	37.84	37.97	61.31	3759	5.647	14.69	37.84	84.04	150.5
7A	41.5-42.5	51.15	31.11	37.97	55.87	3122	4.327	11.99	31.11	69.45	131.8
7A	42.5-43.5	55.8	39.71	66.44	5.47	3418	5.81	15.54	39.71	82.04	143.5
7A	43.5-44.5	109.7	56.24	72.94	161.9	26228	7.927	22.17	56.24	114	219.8
7A	44.5-45.5	101.2	46.79	80.07	142.9	20417	6.029	16.18	46.79	112.8	269.6
7A	45.5-46.5	90.61	41.48	66.44	138.2	19110	5.638	15.35	41.48	95.01	198.8
7A	46.5-47.5	58.87	35.83	34.58	61.26	3753	4.922	13.33	35.83	83.66	156.3
7A	47.5-48.5	87.25	47.25	72.94	117.4	13794	6.813	17.89	47.25	101.1	193.4
7A	48.5-49.5	60.37	39.51	72.94	61.5	3782	5.808	15.29	39.51	83.89	149.3
7A	49.5-50.5	68.32	46.71	72.94	77.6	6021	6.557	17.65	46.71	92.44	151.1
7A	50.5-51.5	64.32	44.12	72.94	64.32	4138	5.852	16.15	44.12	91.01	153.4
7A	51.5-52.5	59.97	34.56	37.97	68.6	4706	4.576	12.73	34.56	79.42	162.1
7A	52.5-53.5	34.95	18.71	13.61	43.3	1875	2.615	8.558	18.71	42.84	87.65
10A	33.5-34.5	46.65	28.48	34.58	50.63	2564	4.028	11.71	28.48	61.58	122.8
10A	34.5-35.5	52.24	35.33	45.75	51.23	2625	5.151	14.24	35.33	73.04	129.6
10A	35.5-36.5	48.61	29.94	37.97	54.24	2942	4.138	12.09	29.94	63.14	121.8
10A	36.5-37.5	47.47	32.41	37.97	47.96	2301	4.814	13.63	32.41	63.86	113.3
10A	37.5-38.5	91.12	32.04	34.58	158.7	25174	4.334	12.75	32.04	74.84	223.9
10A	38.5-39.5	52.35	33.76	41.68	57.37	3291	5.244	14.14	33.76	66.73	127.2
10A	39.5-40.5	41.3	28.14	34.58	42.47	1804	4.173	11.77	28.14	55.4	96.16
10A	40.5-41.5	53.86	36.26	45.75	57.56	3313	5.607	15.32	36.26	70.24	123.9

10A	41.5-42.5	34.98	22.77	34.58	38.68	1496	3.239	9.976	22.77	44.12	81.54
10A	42.5-43.5	50.86	34.56	37.97	50.71	2572	5.573	14.64	34.56	68.92	122.2
10A	43.5-44.5	41.62	27.78	34.58	44.58	1987	4.287	12.06	27.78	53.2	97.37
10A	44.5-45.5	45.9	30.33	37.97	50.43	2543	4.707	12.91	30.33	58.46	105.7
10A	46.5-47	53.78	36.32	80.07	51.18	2619	4.868	13.3	36.32	80.9	132.4
6A	40.5-41	47.18	24.05	31.5	57.65	3324	2.601	8.973	24.35	60.35	138.8
6A	41-42	47.47	28.85	34.58	53	2809	3.946	11.7	28.85	61.02	124.8
6A	42-43	53.51	31.5	37.97	63.28	4004	4.347	12.82	31.5	65.26	140.7
6A	43-44	57.17	32.95	37.97	67.09	4501	4.599	13.21	32.95	70.47	154.3
6A	44-45	47.09	28.23	34.58	52.62	2768	3.806	11.4	28.23	61.05	125.7
6A	45-46	103.3	49.35	66.44	143.9	20708	7.219	19.29	49.35	111.5	288.3
6A	46-47	60.95	36.21	37.97	67.46	4550	5.305	14.29	36.21	78.86	168
6A	47-48	52.33	31.38	34.58	59.9	588	4.096	12.68	31.38	65.13	138.1
6A	48-49	101.7	51.15	72.94	140.2	19664	6.457	18.38	51.15	115.1	231.7
5A	50-51	43.11	28.11	34.58	46.14	2129	2.726	10.31	28.11	58.69	107.1
5A	51-52	87.08	46.39	60.52	117.3	13757	6.577	19.08	46.39	97.65	200.5
5A	52-52.5	61.6	40.08	41.68	62.28	3878	5.255	15.53	40.08	87.63	153
5A	52.5-53	72.63	63.3	105.9	56.7	3215	6.194	23.52	63.3	110.9	155.7
5A	53-54	184.9	119.6	168.9	241.6	58350	9.855	45.86	119.6	202.1	412.4
5A	54-55	237.5	216.6	223.4	141.6	20046	58.13	10.5	216.6	324.5	451.9
8A	41-42	38.66	20.47	34.58	48.6	2362	2.142	7.886	20.47	47.72	101.1
8A	42-43	56.87	39.5	66.44	55.5	3080	5.661	15.4	39.5	79.59	135.3
8A	43-44	52.16	32.84	37.97	56.64	3208	4.499	12.86	32.84	68.9	132
8A	44-45	42.38	24.16	34.58	53.76	2890	2.508	9.353	24.16	51.02	103.3

8A	45-46	55.58	18.99	245.2	80.14	6423	1.48	6.257	18.99	62.19	207.1
9A	34.5-35.5	38.34	22.62	31.5	45.22	2045	3.065	9.573	22.62	47.59	94.24
9A	35.5-36.5	41.56	24.49	34.58	48.97	2398	3.123	9.946	24.49	51.84	105.8
9A	36.5-37.5	47.41	31.35	41.68	49.83	2483	4.026	12.14	31.35	64.64	114
1A	35.5-36	46.24	30.78	34.58	50.85	2585	4.697	13.45	30.78	59.43	106.2
1A	36.5-37	47.48	34.85	37.97	43.75	1914	6.112	15.7	34.85	65.21	108
1A	45-45.5	49.98	35.99	37.97	45.53	2073	6.037	14.82	35.99	71.23	117.5
1A	30-30.5	45.47	31.02	37.97	45.16	2040	4.975	13.38	31.02	62.07	106.1
1A	25.5-26	73.46	36.89	34.58	110.7	12263	5.739	15.58	36.89	82.94	159
1A	20-20.5	44.32	28.88	37.97	46.19	2134	4.463	12.45	28.88	58.62	111.2
1A	15.5-16	38.06	24.27	28.7	42.35	1794	4.07	11.28	24.27	46.55	92
1A	10.5-11	51.81	36.71	60.52	47.83	2288	6.075	16.15	36.71	71.92	122.3
13A	24-25	166.1	61.98	66.44	229	52420	6.37	22.87	61.98	182.9	561.6
13A	25-26	197.9	77.82	72.94	273.6	74856	9.508	29.74	77.82	215.2	601.8
13A	35-36	76.1	61.43	153.8	64.27	4130	4.717	19.01	61.43	121.9	172.5
13A	39-40	120.2	47.76	55.13	173	29944	5.75	18.37	47.76	119.2	444.4

APPENDIX L. Comparison of particle size distribution in cores 10A-1G, 7A-1G, and 5A-1G along the west-east transect of the southern basin, respectively.

Event Layer ID	Event Layer Thickness (cm)	Color	West-East Transect						North-South Transect		
			12A-1G	11A-1G	10A-1G	7A-1G	6A-1G	5A-1G	9A-1G	7A-1G	8A-1G
EL1-A	0.5-3	Red-brown to dark brown; light-colored clay cap	NA	NA	Medium Sand/ Moderate MS	Medium Sand/ Moderate MS	Coarse Sand/ Very High MS	Coarse sand/ Moderate MS	NA	Medium Sand/ Moderate MS	Silt/ Moderate MS
EL1-B	1-4.5	Red-brown to dark brown; light-colored cap clay	NA	Coarse Silt/ Very High MS	Silt/ Very High MS	Silt/ Moderate MS	Coarse Silt/ Very High MS	Coarse Silt/ Very High MS	Silt/ Moderate MS	Silt/ Moderate MS	Silt/ Moderate MS
EL1-C	1-3	Red-brown to light brown	Silt/ Moderate MS	Silt/ Moderate MS	Silt/ Moderate MS	Silt/ Moderate MS	Coarse Silt/ Moderate MS	Sand/ Moderate MS	Silt/ Moderate MS	Silt/ Moderate MS	Silt/ Moderate MS
EL1-D	2-3	Dark to light brown	Silt/ Moderate MS	Silt/ High MS	N/A	N/A	N/A	N/A	N/A	N/A	N/A
EL1-E	0.5-4	Dark-colored	N/A	N/A	N/A	N/A	Silt/ Moderate MS	Silt/ Moderate MS	N/A	N/A	N/A
EL1-F	0.5	Black to dark brown	Silt/ Moderate MS	Silt/ High MS	Silt/ Moderate MS	Silt/ Moderate MS	Silt/ High MS	Silt/ Moderate MS	N/A	Silt/ Moderate MS	N/A

EL3-A	1-15	Black to red brown; light-colored clay cap	Medium Sand/ High MS	Medium Sand/ High MS	Medium Sand/ Very High MS	Medium Sand/ Moderate MS	Coarse Sand/ Very High MS	Coarse sand/ Moderate MS	Medium Sand/ Moderate MS	Coarse Sand/ Moderate MS	Coarse Sand and Gravel/ High MS
EL1-G	0.5-1	Dark red-brown; light colored clay cap	N/A	N/A	N/A	Coarse Silt/ Moderate MS	Silt/ Moderate MS	Coarse Silt/ Moderate MS	Silt/ Moderate MS	Coarse Silt/ Moderate MS	N/A
EL1-H	0.5-2.5	Dark red-brown to black	N/A	N/A	N/A	Coarse Silt/ Moderate MS	Silt/ Moderate MS	Coarse Silt/ Moderate MS	N/A	Coarse Silt/ Moderate MS	N/A
EL1-I	0.5-1.5	Black to dark brown	N/A	N/A	N/A	Coarse Silt/ Moderate MS	Coarse Silt/ High MS	Coarse Silt/ High MS	N/A	Coarse Silt/ Moderate MS	N/A
EL1-J	0.5-1.5	Black to dark brown	Coarse Silt/ Moderate MS	Coarse Silt/ Moderate MS	Coarse Silt/ Moderate MS	Coarse Silt/ Moderate MS	Coarse Silt/ High MS	Coarse Silt/ High MS	Silt/ Moderate MS	Coarse Silt/ Moderate MS	N/A
EL1-K	1-2	Dark red-brown to black	N/A	Silt/ Moderate MS	Coarse Silt/ High MS	Coarse Silt/ Moderate MS	N/A	N/A	Coarse Silt/ High MS	Coarse Silt/ Moderate MS	N/A
EL1-L	1.5-3	Red-brown to light brown; light-colored clay cap	N/A	Silt/ Low MS	Silt/ Low MS	Silt/ Moderate MS	Silt/ Low MS	Silt/ Moderate MS	Silt/ Moderate MS	Silt/ Moderate MS	N/A
EL1-M	0.5	Light brown to red-brown	N/A	Silt/ Moderate MS	Silt/ Moderate MS	N/A	N/A	N/A	N/A	N/A	N/A

EL1-N	0.5	Red-brown	N/A	N/A	N/A	N/A	N/A	N/A	Silt/ Moderate MS	Silt/ Moderate MS	N/A
-------	-----	-----------	-----	-----	-----	-----	-----	-----	-------------------------	-------------------------	-----